Doctoral Dissertation

Nanosized electromechanical devices consisting of carbon nanotubes

Ryosuke Senga

January 2013

Graduate School of Engineering,

Osaka University

Doctoral Dissertation

Nanosized electromechanical devices consisting of carbon nanotubes

Ryosuke Senga

January 2013

Graduate School of Engineering,
Osaka University

Table of contents

Abbreviations

AFM:	Atomic Force Microscopy
CNT:	Carbon nanotube
CVD:	Chemical Vapor Deposition
MEMS:	Microsized Electromechanical Device
NEMS:	Nanosized Electromechanical Device
SEM:	Scanning Electron Microscopy
SPM:	Scanning Probe Microscopy
TEM:	Transmission Electron Microscopy

Chapter 1 Introduction

1.1 Development of technologies

Our lifestyles have been changed and improved with many discoveries in science and technological development. For example, advances in the field of transport, rapid evolution of automobiles, trains, and airplanes, enable us to visit any place around the world. Even if we do not venture out of our homes, the recent whirlwind development of the information technology (IT) field enables us to obtain vast information and connect with people all over the world through the internet. One such new communication style is designated as Social Network Service (SNS), which brings people closer and sometimes becomes a large motivating force for changing the world as a trigger of evolution.

We are also confronting numerous severe problems such as environmental pollution, rapid depletion of resources, economic differentiation, and uncertainty related the economy. These are common issues confronting the governments of many countries. Furthermore, even now, it must not be forgotten that, with our all technologies, we have no power that is capable of protecting human civilization from the awesome power of nature that is manifested during natural disasters. On March 11, 2011, Japan experienced its most destructive earthquake and tsunami in recorded history. That event strongly underscored humanity's powerlessness and helplessness against unprecedented disasters. In this century, we must confront these facts and overcome such tragedies.

The basic study of science has huge potential for solving the issues presented above and gives us ideas for living with nature. Especially, new fields that have yet only insufficiently matured are expected to present unlimited possibilities. A good example is the discovery of Higgs bosons [1], which is one of the most important news stories of recent science. It is said that a Higgs boson will be a key to elucidate the creation of the universe. The discovery does not appear to be immediately applicable to our lives. However it has possibilities as hints or bases for some applications or technologies. Perhaps the day when the Higgs boson will be used as a necessary fixture for our lives such as electrons or X rays will come. Nanotechnology, which is a main topic of this thesis, is also an important field of the twenty-first century, which will support our lives and society.

1.2 History of Nanotechnology

Until a half-century ago, nanoscale science and technology as well as above Higgs boson's story were also a similar "dream vision". Visionary physicist Richard Feynman, in his prescient 1959 Caltech speech "There's Plenty of Room at the Bottom" issued a public challenge and a thousand-dollar prize to the first person to create an electrical motor "smaller than one sixty-fourth of an inch" [2]. This is a first step to open the small scale science and technology. Subsequently, many efforts have been made to develop small machines. Microsized electromechanical systems (MEMS) have been well known from the first appearance of microsized gears or motors in the mid-eighties [3]. The MEMS technology, an integration of top-down semiconductor processing and engineering physics, enables tiny machines to be fabricated from smaller components on the scale of millimeters to micrometers. Now many kinds of MEMS such as printer heads, pressure gauge sensors, and cantilevers for scanning probe microscope and so on are commercially produced [3].

Moreover, miniaturization to a degree greater than MEMS presents the futuristic field of nanosized electromechanical systems (NEMS). Now, the world of the tiniest machines, for example, a transistor in an integrated circuit chip, can be regarded as an achievable goal as Moore's law races towards 40 nm feature sizes [4]. Nanoscale science and technology is not any more a "dream vision", but clearly a growing field, which is expected to solve many problems we confront as described in the first section.

1.3 Specific physical properties in nanoscale

The idea of the limiting size scale of components of devices is important for nanotechnology. As the size of materials approaches the atomic scale, the relevant physical laws change from the classical to the quantum-mechanical laws, nanophysics. This change from classical physics to nanophysics can sometimes provide devices with new performance. It is a most attractive and common challenge for scientists to be involved in nanotechnology to understand such specific phenomena in the nanoscale and to exploit those specific properties for new devices. This thesis also specifically examines the basis of nanophysics, especially mechanical properties, and applications.

One interesting effect obtained by minimization of the materials is increasing of the resonance frequency of fixtures. A frequency that is inversely proportional to a length is typical of mechanical oscillators such as violin or piano string and the frequency

generated using a solid rod of length struck on the end. If one were able to shorten a brass rod to 100 nm length, then the corresponding frequency could be of GHz order, which corresponds to an electromagnetic wave with several centimeters of wavelength. This huge change in frequency will enable completely different applications to be addressed and can be achieved simply by changing the device size.

Another important consideration is dominant force in the nanoscale. When the size becomes small and short, the mass must be small. Then the van der Waals force and electrostatic force become dominant rather than the gravity proportional to the mass. Viscous force is expected to be effective and cannot be ignored if in a liquid.

In contrast, friction force can be nearly zero in nanotechnology envisioned by K. Drexler [4] in which moving elements such as bearings and gears are fashioned from diamond-like "diamondoid" covalently bonded materials, as presented in Fig. 1.1. Drexler's proposed nanocomponents, which are based on the simulations, have not been fabricated experimentally yet. However, there is a natural example of such a highly symmetric nested material. That is a carbon allotrope named the carbon nanotube (CNT) discovered at the end of twentieth century. The CNT surface, which is made by rolling up a graphene sheet, ideally has no roughness. Then, amazing low friction between layers of a CNT is demonstrated [5,6]. The discoveries of nanocarbon materials such as fullerene, graphene, and CNT clearly expand the research fields of nanotechnology.

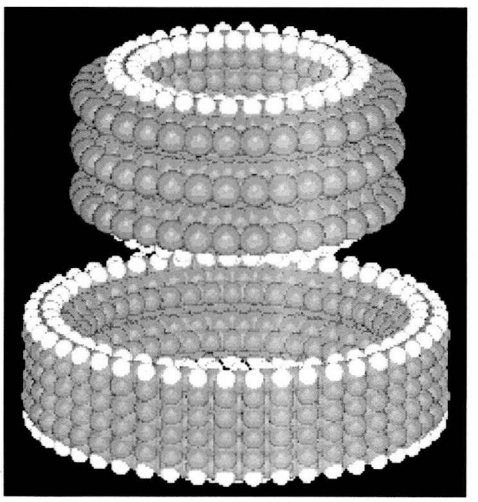

Fig. 1.1 Proposed sleeve bearing of diamondoid atoms [7].

1.4 Nanocarbon materials

Carbon is an important element that is deeply related to our daily life. Coal, charcoal and coke have long been used as fuels. Diamond and graphite, carbon allotropes, have also been widely used after the commercial synthetic methods were established. Therefore, by the 1980s, carbon science was widely regarded as a mature discipline. However, that situation is completely changed today because of the discovery of the first all-carbon molecule, buckminsterfullerene, by H. Kroto and R. Smalley in 1985 [8]. It was that discovery which led to the synthesis of fullerene-related carbon nanotubes and which made carbon science suddenly so fashionable.

The first buckminsterfullerene is C_{60}, consisting of 60 carbon atoms bonded in an icosahedral structure with 20 hexagons and 12 pentagons. This is a soccer-ball-like structure with 0.71 nm diameter. Subsequently other higher order fullerenes such as C_{70}, C_{80}, C_{84}, and metallofullerenes, which contain metal atoms in their cages were reported continuously [9]. The fullerenes are widely studied for application. In medical fields, they are expected to be the smallest cages for drug delivery system because of their size and toughness against physical and chemical stimuli [10]. Some cosmetics, golf clubs, tennis racket and lubricants for automobiles are already used commercially [11].

The history and story of discovery of CNT is somewhat complex. This thesis does not address all works related to the discovery of CNT because of space constraints. However the first work shows clear images and provides detailed structures of CNTs obtained using transmission electron microscopy (TEM). Therefore, one of the most important reasons underlying the current explosion of interest in CNTs is work reported by S. Iijima in 1991 [12], who found highly crystallized multiwall CNTs (Fig. 1.2) in soot, which was usually ignored in the process of fullerene synthesis. CNTs are cylindrical, resembling a rolled-up of a sheet in which carbon atoms are covalently bonded. The diameter of CNTs ranges from less than 1 nm to several tens of nanometers. The length is also varied from nanometer-order to millimeter-order depending on the growth conditions.

Why is the research field of this needle-like material explored so much today? The answer is in the unique properties of CNT which appears only in case of the nanoscale described above. One amazing property of CNT is the electronic property that can be metallic or semiconducting depending on the geometric structures of CNTs so-called chiralities [13]. From this unique electronic property and its nanosized scale, CNTs have been well expected to replace the existing silicon semiconductor devices. They have been actively investigated for applications as some kinds of transistors [14]. Thermal

conductivity is calculated to approach 6600 $Wm^{-1}K^{-1}$ [15], which is higher than a diamond's value. Such high thermal conductivity also becomes beneficial for CNT-based devices in terms of heat efficiency. In addition, CNTs have both a chemically and physically stable structure. The tensile strength reaches 100 GPa [9], the atomic scale stability to temperature in vacuum approaches approximately 2700 K [16] (in the case of highly crystallized multiwall CNTs). No acid can break the covalent bonds of CNT. Therefore, CNTs have the possibility of surviving under any strict conditions.

Some parts of CNT applications are commercially available, as are the applications of fullerenes. For example, the use of the tips for scanning probe microscopy improves resolution and increases the lifecycle dramatically [17]. Transparent electrodes using CNTs for mobile phones and novel flexible electronic papers are now ready for mass production [18]. However, a large part of applications, especially small devices consisting of a few molecules, which are proposed, are still in the stage of research. The situation is not so much different in the field of fullerene described above and graphene, which has recently attracted attention along with CNTs.

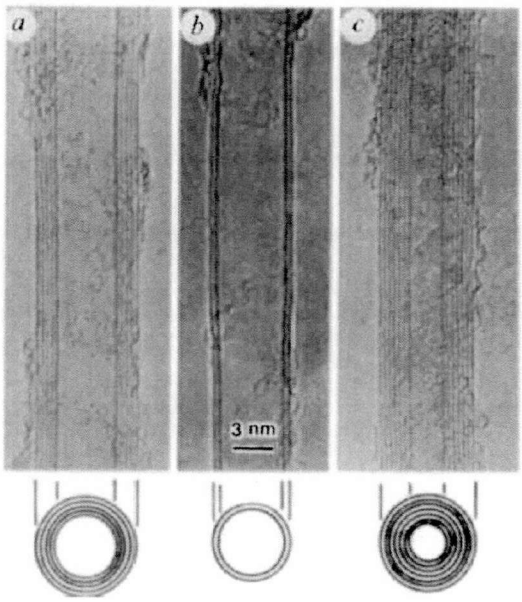

Fig. 1.2 Clear TEM images of CNTs taken for the first time by Sumio Iijima [12].

1.5 Objectives and contributions of this thesis

What are the difficulties for applying large potentials of nanocarbon materials to

devices? The greatest difficulty is in the process of fabricating the devices. Unlike conventional silicon devices, nanocarbon-based devices are thought to be composed using a bottom-up process. Consequently, techniques and bases for operating and fabricating nanosized molecules are necessary. Moreover, we must access the devices with atomic-level analysis. Such nanoengineering for nanodevices has not been established yet. By virtue of the enormous efforts of many researchers, the theory is being fixed. Therefore, development of the field of nanoengineering is necessary for the next phase of nanotechnology.

The objective of this thesis is to design, fabricate and access nanodevices consisting of CNTs and related materials experimentally and to make a basis for nanocarbon devices. This thesis deals with nanodevices of three types. The first device is a high-frequency oscillator using low friction between layers in a CNT. The second is a nanotorsional actuator based on the unique state transition property. The third is a nanosensor for measuring single biomolecules. The concepts of those three devices are described in chapter 3.

Chapter 4 presents discussion of the feasibility of the high-frequency oscillator. The oscillator is based on the linear motion of short CNTs, which are so-called CNT capsules in a hollow space sealed with other capsules inside a single-wall CNT. I have examined the effect of thermal energy on the linear motion of a CNT capsule. TEM observations demonstrate that the back-and-forth motion of the CNT capsule is thermally activated. In the sense of designable device, the fabrication process of the oscillator is also important. The ideal oscillator consists of a CNT capsule in a dumbbell-shaped CNT. The dumbbell-shaped CNTs are fabricated by application of current with tensile stress using TEM manipulation.

Chapter 5 describes an experimental investigation of a torsional actuator consisting of a CNT. TEM results revealed that the CNT, from its flattened state when energetically stable at room temperature, changes states reversibly to a tubular state depending on the amount of current applied to the CNT. Moreover, the flattened CNT can be twisted initially. Then the transition from the flattened state to the tubular state can reverse the twist and generates a torsional torque. The author has also used molecular dynamics simulations to examine the transition behavior and to investigate how the torsion angle is determined and what the driving force is. Results indicate that a specific graphitic stacking order taken for the CNT inside determines the initial twist of a flattened CNT and thereby determines the rotational angle. Results also clarified that the transition results from thermal energy.

Chapter 6 presents development of functional CNT tips, which are so-called CNT

arms as components of nanosensors for single-molecule measurements. Our proposed biosensors measure an interactive force between two protein molecules and a mass of a single protein molecule. For those measurements, a CNT arm that is a part for trapping a single protein molecule in the devices should be designed and fabricated suitably considering measurement situations. In the force measurement, the CNT stiffness is important to avoid undesired bending or vibration of the CNT. However, the use of thicker CNT probes makes it impossible to measure biological reactions as a single-molecule level. We fabricated conical CNTs with a sharpened end by cutting multiwall CNTs with the application of excess current. Regarding the CNT arm for mass measurement, we must meet stricter requirements. Because the mass measurement system is based on a CNT-FET device detecting the resonance frequency of a mechanical vibration of a CNT as an electrical signal in a liquid, the CNT stiffness is also crucial to generate suitable signals in a liquid. In this case, a cone shape is useless because its mechanical vibration mode is too complex to analyze. I demonstrated the fabrication process to join a thin and short CNT, which is a molecule trapping part on the tip of a multiwall CNT using TEM manipulation.

Chapter 2 Carbon nanotube structure, synthesis, properties

2.1 Introduction

Carbon nanotubes (CNTs) present great potential for use as building blocks of nanosized devices because of their unique structure and properties. The fundamental physics of CNTs has been widely researched and has been gradually clarified. This chapter starts from a discussion of the typical structures of carbon materials based on the atomic structure of carbon atoms. Then, several synthesis methods and representative properties, especially emphasizing mechanical properties of CNTs, are introduced.

2.2 Structure

2.2.1 Bonding of carbon atoms

A free carbon atom has atomic orbitals of $1s^2$, $2s^2$, and $2p^2$. To form covalent bonds, one of the 2s electrons should be promoted to 2p. The orbitals are then hybridized in one of three possible ways. In graphene, as presented in Fig. 2.1(a), which is a single sheet of graphite, one of the 2s electrons hybridizes with two of the 2p electrons to give three sp^2 orbitals at 120° mutually in a plane, with the remaining orbital having a p_z configuration, at 90° to this plane. The sp^2 hybrid orbital provides strong σ bonds between carbon atoms in the plane. For graphite, the p_z orbitals, so-called π orbitals, fabricate connections between sheets with van der Waals interaction. The overlap of π orbitals on adjacent atoms in a given plane provides the electron bond network, which gives graphite its high electrical conductivity.

Diamond, consisting of carbon atoms, has been an important material throughout human history. In diamond, each atom is joined to four neighbors in a tetrahedral structure. The bonding here is formed by sp^3 hybridization resulted from the mixing of one 2s and three 2p orbitals. Diamond, which is said to be less stable than graphite, converts to graphite at a temperature of 1973 K at normal pressures [9].

The fullerene, here a C_{60} molecule as presented in Fig. 2.1(b), consists of carbon atoms bonded in an icosahedral (soccer ball) structure with 20 hexagons and 12

pentagons. Each carbon atom in C_{60} is joined to three neighbors. Then the bonding fundamentally behaves as sp^2 but it also has the character of sp^3 because of its curvature.

CNTs, as presented in Fig. 2.1(c), are graphene cylinders. A single-wall CNT (SWCNT) is a rolled-up graphene sheet, of which the sheet edges are mutually joined. The bonds are formed by mainly sp^2 hybrid orbitals. However, the several physical properties of CNTs are affected strongly by how the graphene sheet is rolled up. As described later, a unique characteristic is an electronic property in which separation between metallic or semiconductive behavior appears depending on the geometric structures of CNTs: their so-called chiralities.

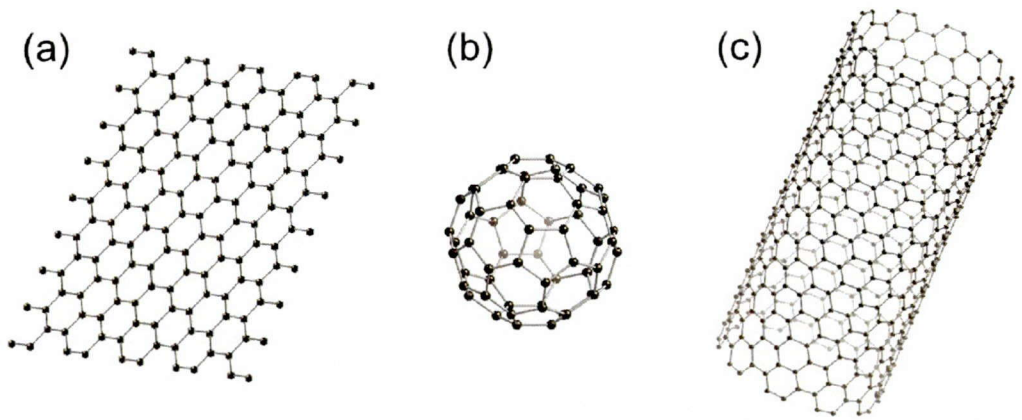

Fig. 2.1 Models for (a) a graphene layer, (b) a C_{60} fullerene molecule, and (c) a single-wall CNT.

2.2.2 Chirality for carbon nanotube

The simplest means to specify the chirality of an individual CNT is in terms of a vector labeled $\mathbf{C}$ joining two equivalent points on the original graphene lattice. The cylinder is produced by rolling up the graphene sheet. Consequently, a coordinate of an atom in the graphene sheet connects to the atom labeled (0, 0), as presented in Fig. 2.2(a) imparts its chirality. The chiral vector is expressed as

$$\mathbf{C} = n\mathbf{a}_1 + n\mathbf{a}_2 \qquad (2.1)$$

where $\mathbf{a}_1$ and $\mathbf{a}_2$ are the unit cell base vectors of the graphene sheet, as presented in Fig. 2.2(a), and $n \geqq m$. It is apparent from Fig. 2.2(a) that m=0 for all zigzag tubes, whereas n=m for all armchair tubes. All other tubes are designated as chiral. Figures 2.2(b)–2.2(d) present models of (10, 10), (10, 5), and (15, 0) CNTs, which respectively show examples for armchair, chiral, and zigzag CNTs. Because $|\mathbf{a}_1| = |\mathbf{a}_2| = 0.246$ nm, the diameter is given as

$$d_t = 0.246\sqrt{n^2 + nm + m^2}\,/\,\pi \,, \tag{2.2}$$

and the chiral angle is given as

$$\Theta = \sin^{-1}\frac{\sqrt{3}m}{2\sqrt{n^2 + nm + m^2}} \,. \tag{2.3}$$

These equations clarify that the chirality is the most important factor to determine the geometric structure and therefore the CNT properties.

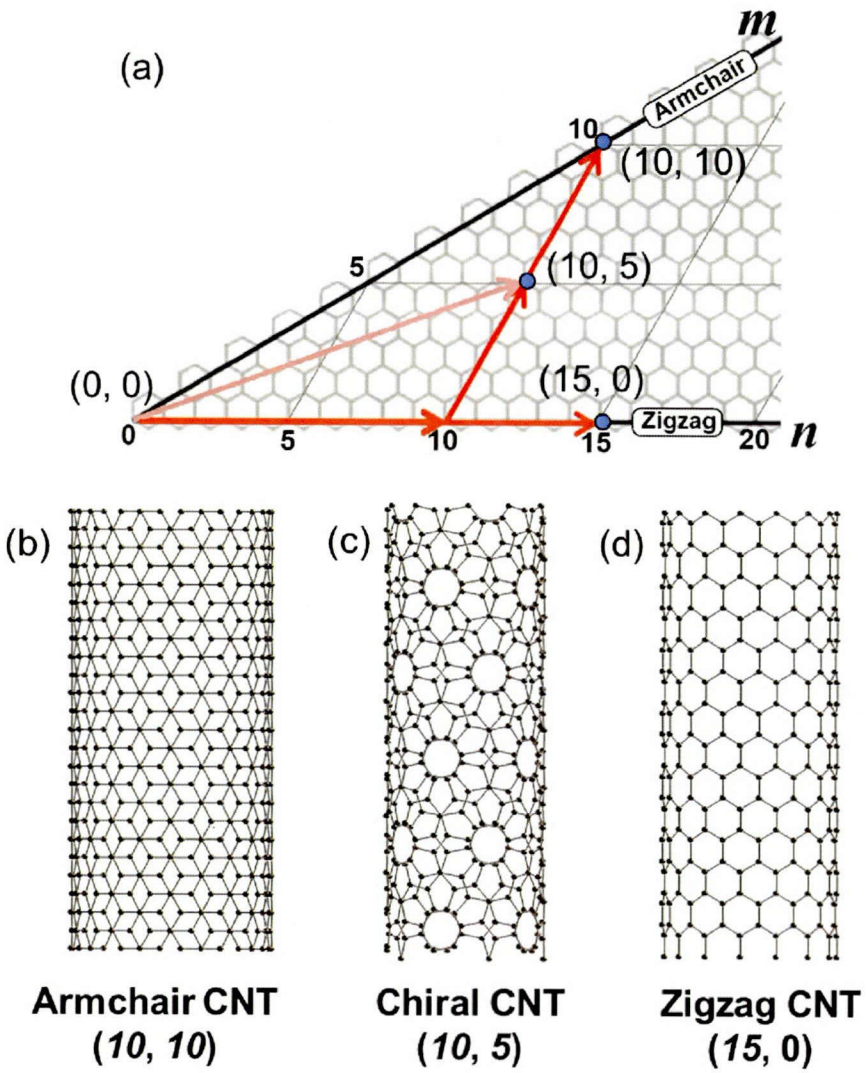

Fig. 2.2 (a) Chiral vector for CNTs and models for (b) armchair CNT (10, 10), (c) chiral CNT (10, 5), and (d) zigzag CNT (15, 0).

2.3 Synthesis

2.3.1 Arc-discharge method

The earliest production of highly perfect multiwall CNTs, reported by S. Iijima in 1991, which becomes an instigator of the after large development of research field of nanocarbon materials, were produced using arc-discharge methods. At that time, S. Iijima used the Kratschmer–Huffman technique for C_{60} production [19], by which the graphite electrodes were held a short distance apart during arc discharge, rather than being kept in contact. Under these conditions, some carbon atoms or dimers that evaporated from the anode recondensed as hard cylindrical deposits on the cathode rod. The yield of this first method was not good. However, in 1992, a breakthrough in multiwall CNT growth by arc-discharge was reported by Ebbesen and Ajayan, who achieved growth and purification of high-quality multiwall CNTs at the gram level [20]. They found that increasing the pressure of He in the arc-evaporation chamber improved the yield of multiwall CNTs formed in the cathode soot dramatically. Another breakthrough is the first success of producing substantial amounts of SWCNTs by arc-discharge demonstrated by Bethune and coworkers in 1993 [21]. An advantage of the arc-discharge method is that highly crystalline CNTs are obtained. Multiwall CNTs produced using the arc-discharge method are used in this thesis.

2.3.2 Chemical vapor deposition

Another important method for producing CNTs is chemical vapor deposition (CVD). CNTs have either single walls or are multiwall and are randomly oriented or oriented, all of which have been uniquely synthesized by CVD. In addition, CVD methods are much easier to scale-up and conduct under milder conditions than those used for arc-discharge (or laser-evaporation) methods. Then, CVD are now widely used for mass production. The growth process in CVD involves heating a catalyst material to high temperatures (973–1273 K) in a furnace and flowing a hydrocarbon gas through the reaction zone for some period of time. The catalytic species are typically transition-metal nanoparticles such as Fe, Co, and Ni. At an earlier stage, those catalysts were supported on the micro-sized particles such as alumina, zeolite, or silica, which usually produces an aggregate powder of single-wall or multiwall CNTs, depending mainly on the catalyst size.

To apply CNTs to the conventional electrical devices, it is important to synthesize CNTs on substrates such as silicon. For synthesizing CNTs on a flat substrate, catalyst particles are deposited on the substrate by sputtering or dip-coating methods. Using this

method, high-density catalyst particles on a substrate are well controlled results. Brush-like CNTs, in which CNTs are vertically aligned, are synthesized.

Several important works support recent advances of mass production technology of CNTs are based on the CVD using substrates. As one mass production study, Y. Nakayama's group developed a large-scale thermal CVD system for synthesizing brush-like multiwall CNTs on a one 6-inch Si wafer every 180 s [22]. In one cycle of the system, a Si substrate covered with a 4-nm-thick Fe film as a catalyst was loaded from a substrate cassette into a CVD chamber. Brush-like CNTs were synthesized on the substrate. Then the substrate was returned to the cassette. Then another Si substrate was processed for the next cycle. Another breakthrough for mass production with CVD growth was made also by a Japanese group in 2004. K. Hata and co-workers developed a new process for a size-selective growth of highly dense vertically aligned CNTs with small amounts of catalyst so-called "Super growth" [23]. The mass production technology of CNTs has come to amount to several tons per year [24].

Applications of vertically aligned CNTs on surfaces produced using CVDs are anticipated in areas such as field emissions [25]. Another important and interesting use of CVD-produced CNTs is the continuous spinning of yarns [22]. Yarns drawn from vertically aligned CNTs are anticipated for use as light and strong ropes or as components of composite materials. CVD methods are also used in the fabrication of nanoscaled devices such as a bridges of single CNTs between alleys [26]. However, CVD-produced CNTs tend to contain high densities of defects such as pentagons and heptagons on their sidewalls. Improvement of CNT quality remains as an important challenge for CVD methods.

2.4 Electrical properties

An amazing CNT characteristic is that they can be metallic, like copper, or semiconducting, like silicon, depending on the chirality. This interesting selection results from whether that of the allowed wave vectors in the Brillouin zone of a CNT passes through a K-point or not. Results show that one-third of CNTs that have $n-m=3q$ (q is an integer) behave as a metal. Then, the other two-thirds of CNTs which have $n-m\neq 3q$ (q is an integer) behave as a semiconductor. The theory has been well discussed by Dresselhaus *et al.* [9,13,27] and then confirmed experimentally using scanning tunneling microscopy by C. Dekker *et al.* [28].

The allowed electronic states for CNTs are much more limited than those for bulk

graphite, which causes the transport behavior of metallic CNTs to be fundamentally similar to that of a quantum wire, which shows ballistic transport. The quantum wire behavior in CNTs has been demonstrated by several groups [29,30]. H. Dai's group demonstrated experimentally that their CNTs exhibited room temperature conductance near the ballistic transport and high current-carrying capability (ca. 25 μA per tube) [31]. Transport in semiconducting single-wall CNTs is more complicated, and appears to be diffusive rather than ballistic. However, experiments have produced evidence showing extremely high mobility in semiconducting CNTs [32].

2.5 Mechanical properties

2.5.1 Young's modulus and tensile strength

Mechanical properties of CNTs are as attractive as their electrical properties for many positive reasons. It is well established that CNTs are the stiffest and strongest fibers ever produced. Predictions by computational studies and experimental measurements of Young's modulus and tensile strength of CNTs have been reported by many groups. A review of computational studies [33] revealed that the predicted values of Young's modulus are 0.5–5.5 TPa. This rather wide range of predicted values is partly caused by the different determination of the wall thickness. Some scientists assume that the wall thickness is equal to the separation between adjacent walls in a multiwall CNT, i.e. 0.34 nm.

Direct measurements of Young's modulus and tensile strength have been conducted using manipulations in atomic force microscopy (AFM), scanning electron microscopy (SEM), and transmission electron microscopy (TEM). M. Treacy *et al.* estimated the Young's modulus of isolated multiwall CNTs by measuring the amplitude of their intrinsic thermal vibrations in TEM. They found that Young's modulus of their multiwall CNTs were in the TPa range [34]. P. Poncharal *et al.* also estimated Young's modulus in TEM by inducing dynamic mechanical deflections to cantilevers of multiwall CNTs by application of alternating electrical fields [35]. The nanotubes were excited resonantly at the fundamental frequency and higher harmonics as presented in Fig. 2.3. The elastic bending modulus, as a function of diameter was found to decrease sharply (from about 1 to 0.1 TPa) with increasing diameter (from 8 to 40 nm), which indicates a crossover from a uniform elastic mode to an elastic mode that involves wavelike distortions in the nanotube. Regarding single-wall CNTs, Ebbesen *et al.* measured Young's modulus of single-wall CNTs by observing their freestanding room temperature vibrations in TEM

and obtained the average value: 1.25 TPa [36].

E. W. Wong *et al.* used AFM to determine Young's modulus of multiwall CNTs by bending isolated multiwall CNTs that were pinned at one end to metal substrates [37]. The bending force was measured versus displacement along the unpinned lengths. Those measurements were conducted in a liquid condition to reduce the effect of friction among CNTs and substrates and provided Young's modulus of 1.28 TPa, which is an average value for CNTs with 26–76 nm diameter.

CNT tips developed for scanning probe scope CNT are also strong tools for elucidation of the mechanical properties. S. Akita *et al.* developed CNT tips for which multiwall CNTs were fixed on Si tips by electron beam deposition of carbon. They used them for measuring the Euler's buckling force in SEM [38]. Figure 2.4 presents the model of the system for the measurement. They pressed a CNT tip to a Si_3N_4 tip for AFM with small spring constant and measured the force by comparing displacements of CNT tip and Si_3N_4 tip. A force curve measurement of CNTs using the CNT tips in the SEM reveals that Young's modulus of a nanotube of 20 nm diameter is 1.1 TPa [38].

Regarding tensile strength of CNTs, M. F. Yu *et al.* measured that of multiwall CNTs using a manipulator in SEM [39]. They observed that the multiwall CNTs broke in the outermost layer ("sword-in-sheath" failure), and the tensile strength of this layer ranged from 11 to 63 GPa. Moreover, B. D. Demczyk *et al.* used manipulation in TEM to carry out a series of pulling and bending tests on individual multiwall CNTs and estimated the tensile strength: ca. 150 GPa [40]. In this case, it should also be recognized that only the outer layers of CNTs were being stressed. When sufficient stress was applied, the outer layers fractured, leaving the inner layers, because of the low interlayer friction (details are described in section 2.5.3).

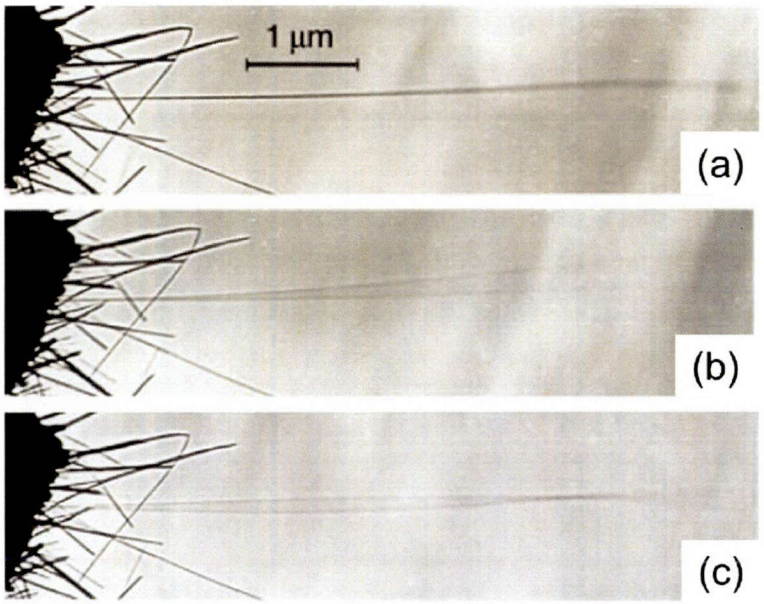

Fig. 2.3 Nanotube response to resonant alternating applied potentials. (a) In the absence of a potential, the nanotube tip (6.25 μm length; 14.5 nm diameter) vibrates slightly because of thermal effects. (b) Resonant excitation of the fundamental mode of vibration (frequency of alternating electrical field is 530 kHz). The shape corresponds closely to that expected for a cantilevered uniform beam. (c) Resonant excitation of the second harmonic (frequency of alternating electrical field is 3.01 MHz) [35].

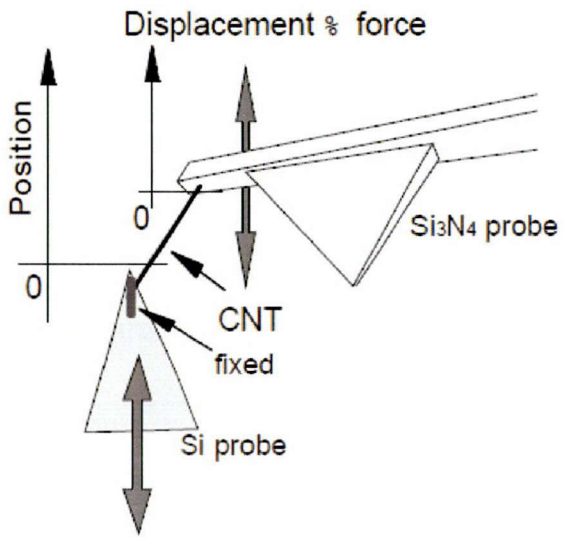

Fig. 2.4 Schematic of the force curve measurement [38].

2.5.2 Deformation of carbon nanotubes

Nanotube behavior under compression has also been studied theoretically and experimentally. B. I. Yakobson *et al.* simulated CNT behavior under compression for several chiralities [41,42]. They observed a kink in the strain energy curve, corresponding to the buckled structure presented in Fig. 2.5. Those buckled single-wall CNTs were observed experimentally using TEM [35]. A buckled CNT can be recovered completely to an initial structure when the stress is removed at room temperature.

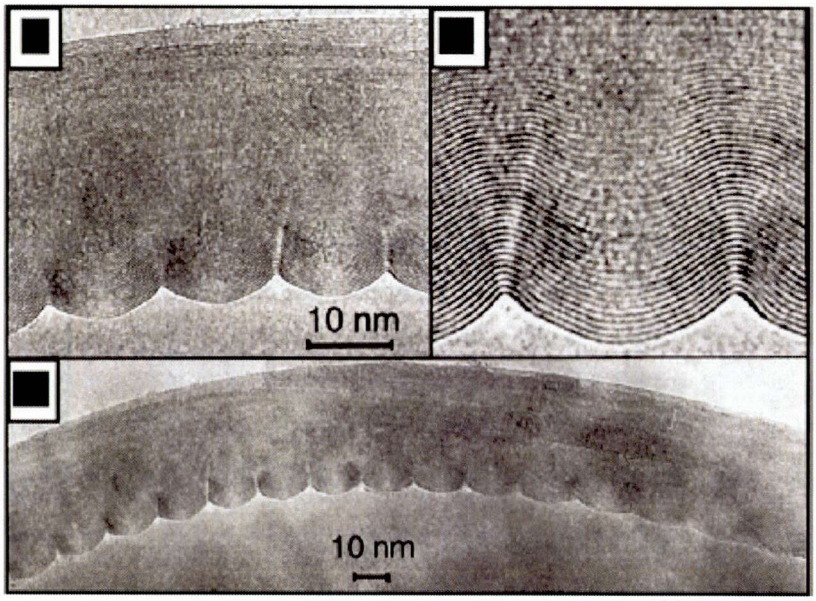

Fig. 2.5 TEM images of a bent CNT (radius of curvature ca. 400 nm), showing wavelike distortion so-called ripples [35].

2.5.3 Tribological properties

Tribology of CNTs has been examined as well as other mechanical properties. The force between two CNTs is usually van der Waals type attractive force. For example, in the case of a nested double-walled CNT as presented in Fig. 2.6, the van der Waals interaction works between inner and outer layers. The van der Waals potential is expressed as shown below.

$$U(x) = -(A/d^2) \cdot S(x)/12\pi \tag{2.4}$$

$$S(x) = 2\pi r \cdot x \tag{2.5}$$

In those equations, A is the Hamaker constant of CNTs, d denotes the distance between layers, $S(x)$ is a surface area of the inner tube for overlapped region with the outer tube, which is defined by the radius of inner tube r and overlapped distance x. Then the force affecting the inner tube is

$$F = -\frac{dU}{dx} = \frac{1}{6}\frac{A}{d^2} \cdot r \tag{2.6}$$

The force is independent of the overlapped distance and works to pull the inner tube back into the outer tube. That has been demonstrated experimentally [5,6]. Furthermore, Suekane *et al.* measured the friction force between two overlapping CNTs inside of a TEM [43]. They concluded that friction force is independent of the overlap length for highly crystalline CNTs but that it is length-dependent for CNTs covered by a certain amount of amorphous layer. These results show that the amorphous layer increases the friction force. In contrast, the amount of friction for highly crystalline CNTs with no impurities is governed solely by the van der Waals force. It is quite low.

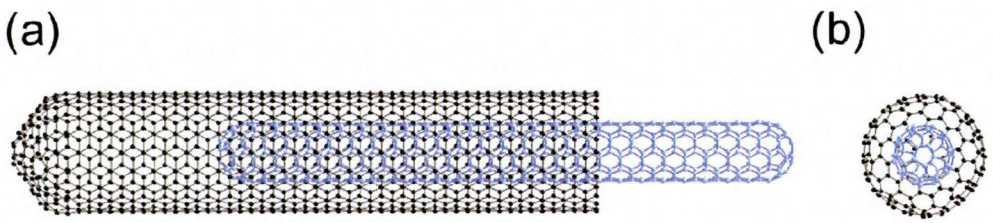

Fig. 2.6 Models of nested double-walled CNT for (10, 10)@(5, 5) from (a) side and (b) axis direction views.

2.6 Thermal properties

2.6.1 Heat capacity

For semiconducting single-wall CNTs, only the contribution of phonons to the heat capacity and the specific heat need to be considered because no degree of freedom exists for electrons in those CNTs. Therefore the contribution of electrons is negligible at room temperature. However, for metallic single-wall CNTs, both phonons and electrons can affect the heat capacity and the specific heat. However, because the electronic density of states near the Fermi level in metallic CNTs is low, the effect of electrons on the heat capacity and specific heat in those CNTs is negligible. Therefore the contribution of phonons is dominant [44]. At low temperatures, the contributions of four acoustic phonon modes in CNTs, including two flexural acoustic (FL) modes, a longitudinal acoustic (LA) mode, and a twisting acoustic (TW) mode, are dominant. As the temperature increases, the contribution of optical phonon modes, which can be negligible at low temperature, begins to contribute to the heat capacity and the specific heat. Regarding experimental measurement, J. C. Lasjaunias *et al.* investigated the heat capacity of bundles of single-wall CNTs at temperatures T of 0.1–7 K [45]. Their results

show contributions from all acoustic phonon modes. Specific heat $C(T)$ for bundles of single CNTs given from their results can be fitted by $C(T)\sim 0.038T^{1/2}+0.006T+0.035T^3$. The term proportional to $T^{1/2}$ and T shows the respective contributions from two FL modes ($\propto T^{1/2}$) and LA and TW modes ($\propto T^3$). Moreover, a vibrational T^3 contribution shows the three-dimensional character of the bundles for low-frequency phonons.

2.6.2 Thermal conductivity

Crystalline CNTs display the highest measured thermal conductivities of all known materials. For pure diamond, the thermal conductivity is 2000–2500 $Wm^{-1}K^{-1}$, whereas for graphite, the in-plane conductivity at room temperature can reach 2000 $Wm^{-1}K^{-1}$. For CNTs, ever higher values are predicted. The highest value reaches 6600 $Wm^{-1}K^{-1}$ for an isolated single-wall CNT at room temperature, as calculated by D. Tomanek *et al.* [15]. Experimental measurements also showed high conductivities. P. McEuen's group obtained a value of higher than 3000 $Wm^{-1}K^{-1}$ for well crystalline arc-grown CNTs at room temperature using a microsized device [46]. Thermal conductivities for CVD growth CNTs were found to be lower, with values of approximately 200 $Wm^{-1}K^{-1}$ [47].

J. Hone *et al.* reported that the electronic contribution to the thermal conductivity is negligible at all temperatures from simultaneous measurements of the electrical and thermal conductivity of bulk samples of single-wall CNTs that had been aligned by filtration in a high magnetic field [48]. In addition, the phonon means free path of single-wall CNTs reaches several micrometers at room temperature. Consequently, ballistic phonon transport is apparent in CNTs with lengths that are sufficiently shorter than the phonon mean free path at low temperatures. Regarding ballistic thermal transport, thermal conductance is quantized and is independent of the CNT length [49].

2.7 Characterization – Transmission electron microscopy

Characterization of CNTs for applications in electronic, mechanical, or sensing devices can be performed using various methods including optical spectroscopy, scanning probe techniques and electron diffraction. Suitable methods are chosen depending on the necessary level of characterization, for instance whether it is sufficient to distinguish metallic from semiconducting nanotubes or whether the chiral index must be determined. Furthermore, it depends on the sample conditions such as its environment, and whether the sample is an individual nanotube or a nanotube bundle.

In this thesis, TEM, a powerful method for observing materials directly, is mainly

used for characterization. It is possible to observe the morphology and atomic arrangements of a specimen directly using TEM. Furthermore, an electron wave is diffracted by materials with a periodic structure and can be converged to a small area. Therefore, electron diffraction enables us to determine the local crystal structure of a specimen. In the case of CNT studies, one important characteristic, chirality, can be determined from electron diffraction patterns [50]. Additionally, we can observe the dynamics of structural changing of materials by equipping a manipulation to a TEM. Our group has demonstrated several important mechanical properties, including plastic bending [51], shape memory effects [52], and a chirality changing of a single-wall CNT in an elongation process [53] using a TEM equipped with a special manipulation holder, a so-called "super nanofactory".

2.8 Summary

This chapter specifically examined unique structures and properties of CNTs. Structures of CNTs can be regarded as rolled-up graphene sheets of which the edges of the sheets are mutually joined. Several physical properties such as electrical behaviors of CNTs are affected strongly by chirality, which shows how to roll up a graphene sheet. The ideal mechanical properties of a CNT reach values of 1 TPa for the Young's modulus and 100 GPa for tensile strength. In addition, the amount of interlayers friction in a CNT or between the outer walls of two CNTs is governed solely by van der Waals force and becomes quite low. Those unique properties show great potential for the creation of next-generation nanodevices.

Chapter 3 Nanodevices

3.1 Introduction

Development of functional nanodevices is a daunting challenge confronting nanotechnology. Several important subjects are related to the creation of nanodevices: preparing suitable materials for device components, developing device fabrication processes, constructing systems for device operations, and assessing device performance. Related to those subjects, several approaches have been attempted. For instance, in the field of bioscience, organic molecules have been studied widely as biomolecular device components. Various polymers, gels, and ceramics have been investigated as components for nanosized actuating devices. Furthermore, not many, but several synthetic devices consisting of CNTs have been reported.

This chapter embarks from a brief review of those previously reported nanodevices. Then the frameworks of nanodevices addressed in this thesis are described. Especially, the originality of devices compared with previously reported devices and important elements for the realization of the devices are discussed.

3.2 Bionanodevices

Excellent examples of nanoscaled devices such as linear and rotary motors are apparent from examination of biological phenomena. Muscle contraction of occurs through the concerted action of vastly numerous muscle myosin and kinesin molecules, which function as unique biological linear motors. In both cases, the molecular motor moves along a strong filament that is part of the internal structure of the cell and acts as tracks for the motors. The energetic impulse of these linear motors is given by the hydrolysis of adenosine triphosphate (ATP) to adenosine diphosphate (ADP). They move in quantized steps, using up a fixed number of ATP molecules per step. As an example, Figure 3.1 presents the model for the movement of a conventional kinesin molecule [54]. The kinesin molecule walks methodically along a microtubule protofilament, stepping from one tubulin subunit to the next (80 Å distance). Unidirectional motion is produced by a pronounced conformational change in kinesin's "neck linker," a 15-amino acid region shown as orange and red parts in Fig. 3.1(a) that is COOH-terminal to the catalytic core. The neck linker can change its configuration

when kinesin is bound to microtubules in its nucleotide-free and ADP-bound states. However, when the microtubule-bound kinesin binds an ATP, the neck linker becomes docked on the catalytic core with its COOH-terminus pointing toward the microtubule plus end. Consequently, the energy associated with ATP binding drives forward motion of the neck linker and any object attached to its COOH-terminus. Recently, that walking model of kinesin molecules and also that of muscle myosin molecules have been confirmed through observations made using high-speed atomic force microscopy (AFM) [55].

Other sorts of motors rotate flagella, providing motion of bacteria through liquid media. The flagella rotary motors are mounted in the wall of a cell, from which they transmit rotational torque and power across the cell wall. ATP synthase (F_0F_1) and F_1-adenosine triphosphate synthase (F_1-ATPase) are typical biomolecular rotary motors found in mitochondria and bacterial membranes. Y. Sambongi *et al.* observed the rotational motion of F_0F_1 motors directly by binding fluorescently labeled actin filaments to the tip of F_0F_1 motors (*c* unit), as depicted in Fig. 3.2 [56]. F_0F_1 motors were attached to a grass coverslip using His tag linked to the lower end of the α subunit. In this motor, the The γ, ε, and *c* units rotated together after adding 5 mM Mg-ATP. This rotary motor is driven by an electrochemical proton gradient and a reverse gradient produced by hydrolyzing the ATP. The rotational rates were measured as 0.5–10 Hz, with torque of the motor of 40 pNnm.

One approach to creating artificial nanodevices is to emulate natural molecular motors such as that explained above. R.K. Soong *et al.* demonstrated a hybrid artificial biomolecular motor as depicted in Fig. 3.3(b), which was assembled from F_1-ATPase and a nickel propeller [57]. Every time an ATP molecule is synthesized, the head of F_1-ATPase as depicted in Fig. 3.3(a) rotates by 120°. The mechanism of rotation of F_1-ATPase is almost identical to that of the F_0F_1 motor described above. In the artificial biomolecular motor, F_1-ATPase was anchored chemically via a histidine linkage on its underside to a lithographically defined nickel pillar on a substrate, and via a biotin–streptavidin linkage on its topside to a nickel propeller, also produced using lithography. In the reported experiment, about 400 propellers led to observation of five that rotated continuously in a counterclockwise direction when 2 mM Na_2-ATP was added. Moreover they stopped their motion when immersed in a buffer solution containing 10 mM NaN_3. Based on those results, the rotary torque of F_1-ATPase motors was estimated as being within a range of 20–100 pNnm.

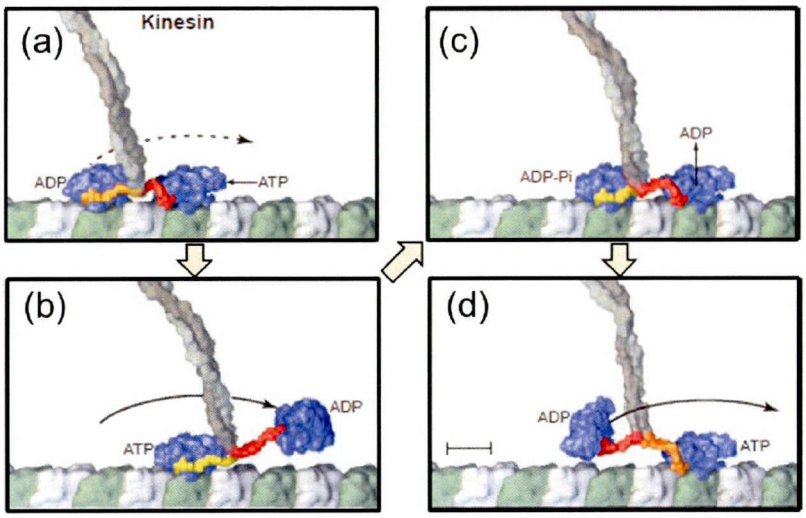

Fig. 3.1 Models of the conventional kinesin motion. The two heads of kinesin dimer move along a tubulin filament in a motion resembling that of bipedal walking. The coiled coil (gray) extends to the top and leads up to the kinesin cargo. (a) Each catalytic core (blue) is bound to a tubulin heterodimer (green, β subunit; white, α subunit) along a microtubule filament. ATP binding to the leading head will initiate neck linker docking. (b) Neck linker docking is completed by the leading head (yellow), which throws the partner head forward toward the next tubulin binding site. (c) New leading head docks tightly onto the binding site. Polymer binding also accelerates ADP release. During this time, the trailing head hydrolyzes ATP to ADP-Pi. (d) After ADP dissociates, an ATP binds to the leading head and the neck linker begins to zipper onto the core (partially docked neck shown as orange). The trailing head, which has released its Pi and which has detached its neck linker (red) from the core, is in the process of being thrown forward (scale bar is 4 nm) [54].

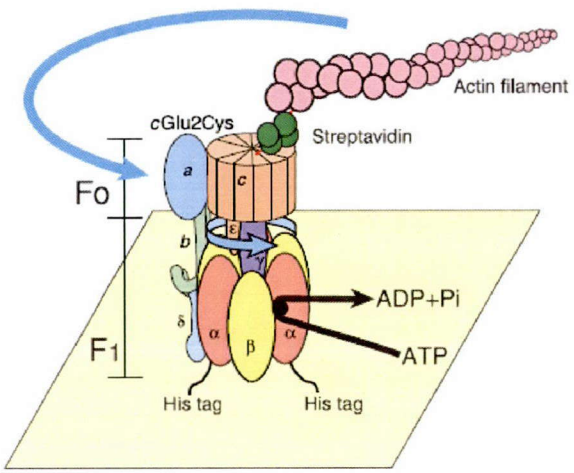

Fig. 3.2 Observation system for the c subunit rotation in F_0F_1. One c subunit of Glu2 was replaced by cysteine and then biotinylated to bind streptavidin and the actin filament. The γ, ε, and *c* units are thus shown to be a rotor, whereas the α, β, δ, *a*, and *b* complex is the stator. The rotation rate of the actin filament in the viscous medium was found to depend upon its length. Rotational rates were 0.5–10 Hz, which is consistent with torque of 40 pN nm [56].

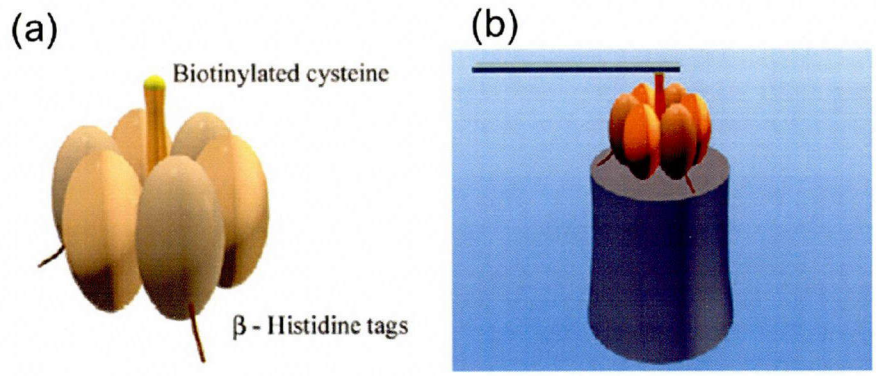

Fig. 3.3 Biomolecular rotary motor powered propellers. (a) Schematic view of F_1-ATPase molecular motor. (b) Schematic view of one assembled device. Ni pillar under the F_1-ATPase molecule and Ni propeller connected to the tip of the molecule are fabricated lithographically [57].

3.3 Nanochemomechanical systems

Although biomolecular motors can drive nanomechanical systems, they are complex and are constrained to functioning under physiological conditions. In contrast, a chemically powered motor can, in principle, be constructed from nanoscale building blocks having several compositions, sizes, and shape, and which can be powered using diverse environmentally friendly on-board fuels. The first challenge for the chemomechanical system is to create an "artificial muscle".

R. H. Baughman's group has demonstrated that conducting polymers can provide attractive actuator materials that function more analogously to natural muscle, and developed practical conducting polymer actuator devices based on the electrochemical doping and dedoping of a conducting polymer [58]. Another group also experimentally demonstrated artificial muscle by a synthetic polymer gel [59]. The gel network is anionic. Positively charged surfactant molecules can therefore bind to its surface, including local shrinkage by decreasing the difference in osmotic pressure between the gel interior and the solution outside.

Those electrochemically actuated conducting polymers and gels excel in some measures of performance such as energy density or strain, but they are unsatisfactory in others such as efficiency and their rapidity of response. Those persist as common challenges for polymer based devices. To improve those points, an electrical actuator made from films of dielectric elastomers such as silicone elastomers coated onto both sides with a compliant electrode material was reported [60]. The maximum strain and

response time (actuating frequency) of the actuator reached 215% and 170 Hz, respectively, which exceeded those of natural muscle.

3.4 Nanodevices consisting of nanocarbon materials

However, existing biomolecular devices are designed to operate in a specific environment where organic molecules can live and where hydrogels or polymers are mechanically fragile or have even slow response rates. It is necessary for future nanosized devices to function in a range of environmental conditions with fast response time and long cycling lifetime and to have a range of functionalities. Such nanodevices have been proposed in nanometer-scale electromechanical systems (NEMS) consisting of CNTs using their unusual mechanical and electrical properties. Although widely diverse devices exist consisting of CNTs, including tips for AFM, emitters, transistors, electrical circuits, sensors, motors, actuators, and oscillators as described in chapter 1 and 2, this chapter specifically examines mechanical systems.

Carbon nanotubes can be excellent shafts for nanomechanical systems because of their low friction between layers. In this concept, an actuator with a metal propeller structure deposited on the multiwall CNTs has been reported as depicted in Fig. 3.4 [61]. The actuator was constructed using lithographic methods. The multiwall CNTs were located with respect to pre-patterned alignment marks on the SiO_2 surface using AFM or SEM. The remaining actuator components (in-plane rotor plate, in-plane stators, anchors, and electrical leads) were then patterned using electron beam lithography, which revealed that applying voltages up to 50 V direct current between the rotor plate and the gate stator generated a net torque sufficient to rotate the rotor plate (up to 20° deflection) visibly by a static electric force. When the applied voltage was removed, the rotor plate would return rapidly to its original horizontal position.

Another group developed a device consisting of a cargo made on the outermost layer of a multiwall CNT suspended between electrodes. They demonstrated that the cargo traveled back and forth along the inner coaxial CNT by thermophoretic force, as depicted in Fig. 3.5 [62]. As the first step for fabrication of the device, multiwall CNTs were deposited onto an oxidized silicon substrate. Electron beam lithography and Cr/Au evaporation were used to attach electrodes to an isolated CNT and to pattern a plate in the middle of the CNT that plays the role of the cargo. A few outer walls of the CNT were removed selectively by application of a large current to the CNT. The device was completed by suspending the nanotube and the cargo using a wet etching step. The

cargo moved linearly along the CNT shaft when the current applied to the CNT shaft. The report concluded that the driving force of the cargo was thermophoretic force induced by Joule heating because the direction of the cargo's motion was independent of the current direction.

Another concept for creation of nanocarbon devices is explained below. As the size of a component of a device becomes smaller, the resonance frequency of the system usually increases, as described in chapter 1. For this reason, nanocarbon materials have been anticipated to realize oscillators that can generate high-frequency waves. Related to this concept, several devices such as a mass sensor [63] and a radio [64] using mechanical vibrations of CNTs have been reported.

The field of nanoscale biosensing using CNTs has also been of interest in biology and has been evolved gradually using single-wall CNTs in a field effect transistor (FET). H. Dai's group developed protein sensors by coating single-wall CNTs with a surfactant [65]. Those CNTs are bridged between source and drain electrodes. The coated CNT attracts specific receptors. Consequently, sensing in solution was conducted by monitoring electrical current through the device during protein addition. As another example, C. Dekker's group developed glucose sensors with a FET made by an individual CNT as depicted in Fig. 3.6 [66]. In the device, controlled attachment of the redox enzyme glucose oxidase to the CNT sidewall was achieved through a linking molecule. It was found to induce a clear change of the conductance. By detecting the conductance change by FET, the enzyme-coated CNT worked as a pH sensor with large and reversible changes in conductance upon changes in pH.

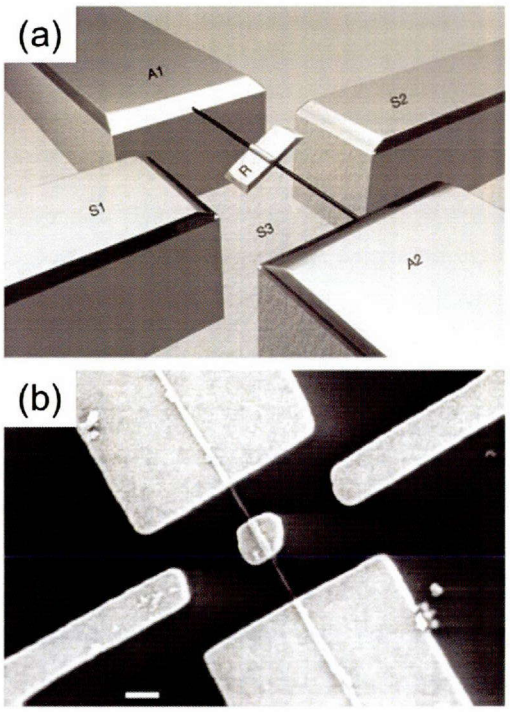

Fig. 3.4 Synthetic rotational actuator consisting of a multiwall CNT. (a) Schematic and (b) SEM image for the device. A metal plate rotor (R) is attached to a multiwall CNT, which acts as a support shaft and which is the source of rotational freedom. Electrical contact to the rotor plate is made via the CNT and its anchor pads (A1, A2). Three stator electrodes, two on the SiO2 surface (S1, S2), and one buried beneath the surface (S3), provide additional voltage control elements. The scale bar in (b) is 300 nm [62].

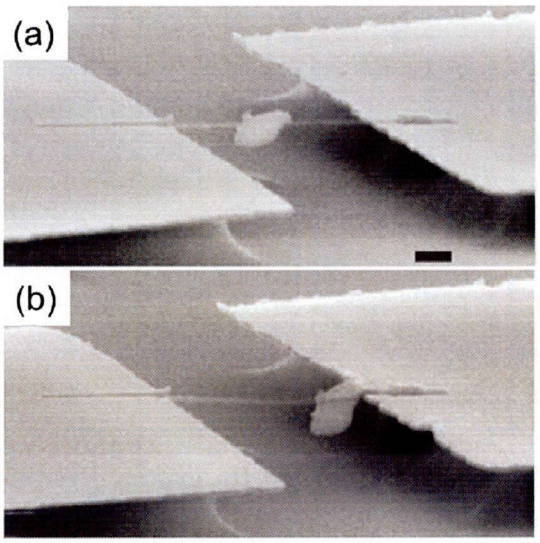

Fig. 3.5 Thermophoretically driven linear motor. (a) SEM images of the device where the Au cargo is attached to the center of the CNT. (b) The cargo moved right via current induction. Scale bar is 300 nm [61].

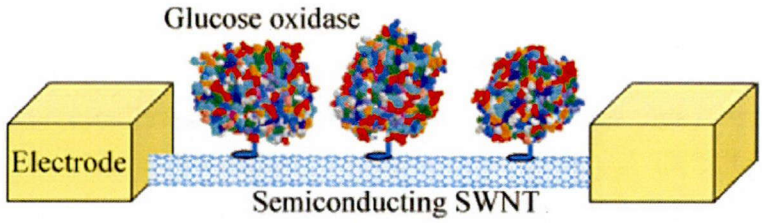

Fig. 3.6 Schematic representation of two electrodes connecting a semiconducting SWNT with glucose oxidase enzymes immobilized on its surface [66].

3.5 Framework of devices studied

3.5.1 Nano-oscillator

As described in section 3.4, an attractive property for future devices is the remarkably low friction that exists between CNT layers. Some devices using a CNT as a shaft have already been reported [61,62] . Those devices utilize the outer walls of CNTs. However, utilization of the inner space of CNTs for devices is still under investigation. The inner spaces of CNTs are attractive for creating nanodevices because no other materials can produce such thin, long, and straight spaces surrounded by smooth walls.

Regarding the physics of the inner space of CNT, our group previously reported a unique phenomenon: a capsule-like short CNT (CNT capsule) traveled back and forth in the hollow space sealed with other capsules inside a single-walled CNT at room temperature (289 K) [67] . However, the effective utilization of inner space of CNTs remains a challenging subject because of the absence of sufficient perception and techniques. Therefore, this study addresses the nano-oscillator, which expands the CNT capsule linear motion and which maximizes the features of the inner spaces of CNTs.

A nano-oscillator consists of a CNT capsule encapsulated in an outer CNT with opened ends. The operating principle of the nano-oscillator is the following. Once the CNT capsule starts to move with a certain initial velocity, the CNT capsule repeats back-and-forth motions supported by the extracting force worked at both opened ends of the outer CNT. The origin of the extracting force is the potential barrier at both opened ends. Additional details related to the principle are presented in section 4.2. However, the opened ends can attract impurities. In terms of working devices, this fact poses severe difficulties, such as obstruction of the CNT capsule motion. For this subject, the model proposed by Legoas *et al.* [68] depicted in Fig. 3.7 can present one solution. Because the external tube cannot have its ends closed, they proposed "to fuse" tubes of different diameters to produce dumbbell-shaped CNTs and thereby "seal" the

device. That system has been expected to enable raised frequencies by several gigahertz, based on the calculations of some researchers [68].

The most remarkable and unique feature of the nano-oscillator is the high-speed linear motion of CNT capsules, which enables gigahertz-order oscillation. Such a high-frequency mechanical oscillation of the capsule structure presents great potential for application to numerous other functional devices such as memory, microwave generators, and gyro-sensors by doping the charge to the CNT capsules. Moreover, the nano-oscillator is robust because of CNTs' resilience, remaining active in a wide range of environmental conditions. That toughness is an important benefit that distinguishes it from other devices made of biomolecules, which need specific conditions.

For realizing the nano-oscillator, first, detailed perception for CNT capsule motion is necessary. According to an earlier report [68], to move CNT capsules, the initial velocity must be given by an external force. However, in our experiment, CNT capsules encapsulated in an outer CNT moved frequently without external forces at room temperature. This result suggests that the motion of CNT capsules results from thermal energy at room temperature. To design the nano-oscillator, clarification of the mechanism supplying linear motion of the CNT capsules and assessment of the mechanical stability of the system including the measurement of the resonance frequency of the system are necessary. In addition, fabrication of dumbbell-shaped CNTs persists as a challenge to creating nano-oscillators. Chapter 4 specifically examines those subjects.

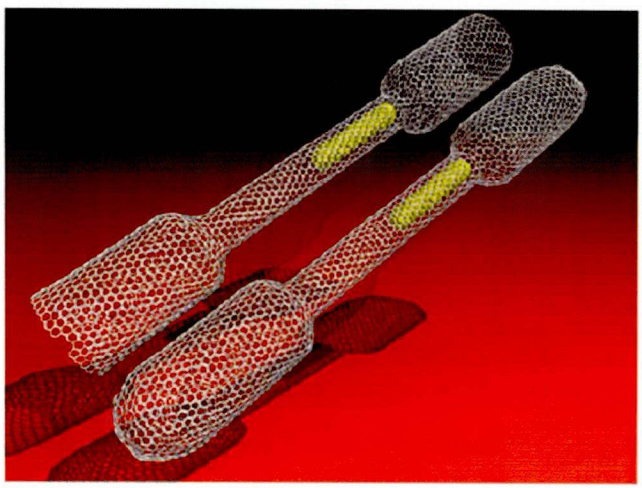

Fig. 3.7 Schematic of nano-oscillator. The inner CNTs oscillate inside a binanotube junction [68].

3.5.2 Nanotorsional actuator

The study described in this section and in chapter 5 originated from the significant finding of a unique state transition behavior of CNTs. Some experiments revealed that multiwall CNTs from which several inner layers had been extracted could take a flattened state by maintaining the CNTs in vacuum or air in a few days at room temperature. Moreover, TEM observations revealed that those flattened CNTs changed their state reversibly to a tubular state depending on the amount of current applied to the CNT [69]. This work is highly original not only because this is the first study in which the transition between tubular and flattened states in a CNT has been experimentally demonstrated and electrically controlled but also for the point on particularly addressing the device using the unique transition behavior described below.

Figure 3.8 depicts the proposed nanosized torsional actuator using the transition behavior. Two electrodes support a flattened and twisted CNT at both ends. One end is fixed to the electrode by an attachment process [70]. The other end, which is connected to the electrode with a CNT bearing [5] structure, is free to rotate. When the CNTs change their states according to the current control, the free end rotates clockwise or counterclockwise.

An extremely attractive feature of the nanotorsional actuator is that it enables generation of reversible rotational motion with high speed and large torque. As described in section 3.2, the biomotors can also provide rotational motion. However, that motion is limited to one direction. Another benefit is that the rotational angle of the torsional actuator is controllable by the CNT structure and the amount of current to apply. This functionality is entirely different from those of rotational motors with CNT shafts described in section 3.4.

Creation of the devices demands detailed understanding of the state transition between tubular and flattened states. In this study, TEM observations and molecular dynamics simulations were used to examine the phenomenon and to investigate the feasibility of the nanotorsional actuator. Details are presented in chapter 5.

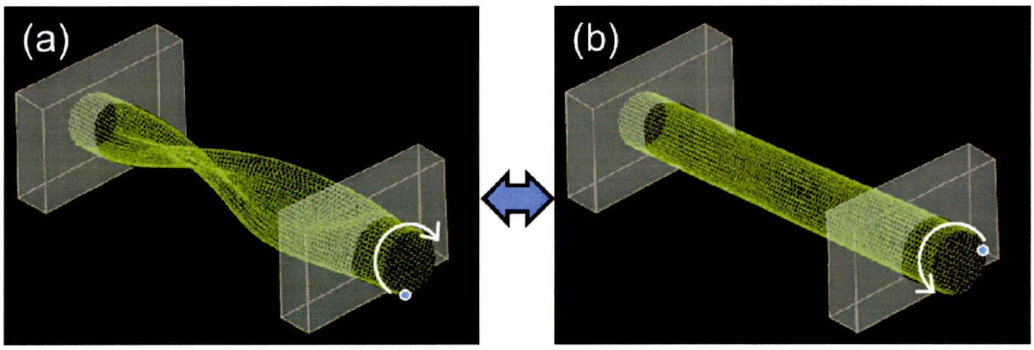

Fig. 3.8 Schematic portrayals of the proposed nanotorsional actuator. The device has two states: (a) flattened and (b) tubular. An atom of the free rotatable end is shown as a blue dot.

3.5.3 Biosensor for a single protein molecule

Carbon nanotubes have been used as biosensors in various ways, as described in section 3.4. Especially, a single CNT is ultimately a suitable material for biosensors for single-molecule measurements. Herein, we propose biosensors using CNTs for measurement of the interaction force between two protein molecules and measurement of the mass of a single protein molecule.

The force measurement system is embedded in AFM, as depicted in Fig. 3.9(a). One protein is attached to the tip of a CNT on the AFM tip, a so-called CNT arm. Proteins of another type are supported on CNTs protruded from resin: so-called CNT sheets. The force is measured using the force curve mode of the AFM.

The mass measurement system is based on the CNT-FET device depicted in Fig. 3.9(b). The system consists of a CNT arm and a CNT transistor. The resonance frequency of the CNT arm can be changed when a protein is trapped at the tip of the CNT arm. The protein mass is calculated by detecting a slight change of the frequency of the CNT arm by the CNT transistor.

The most important advantage of utilization of CNTs for single-biomolecule measurements is their size. Conventional measurements for single biomolecules have been conducted using AFM tips or optical tweezers, but those tools are much larger than a single protein. For that reason, the chemically decorated tip has many reaction groups to biomolecules, which renders a single biomolecule trap at the apex at the tip difficult to produce. Our proposed biosensors overcome this difficulty using a single CNT as an arm for trapping a single biomolecule at its tip. This point also distinguishes our sensors from other biosensors using CNTs, as described in section 3.4. Reported biomolecular sensors using CNTs have used the outer walls of CNTs; they are intended for several molecules. Moreover, biomolecules are bonded site-specifically to the CNT tip by

introduction of special chemical reactions [71,72]. For this reason, biomolecules can maintain their natural condition during measurements.

To realize precise measurements, sophisticated fabrications of the CNT arm such as sharpening and opening of CNT tips and attachment of a CNT with the AFM tip are necessary. This study specifically examines the CNT arm fabrication process, which is addressed in chapter 6

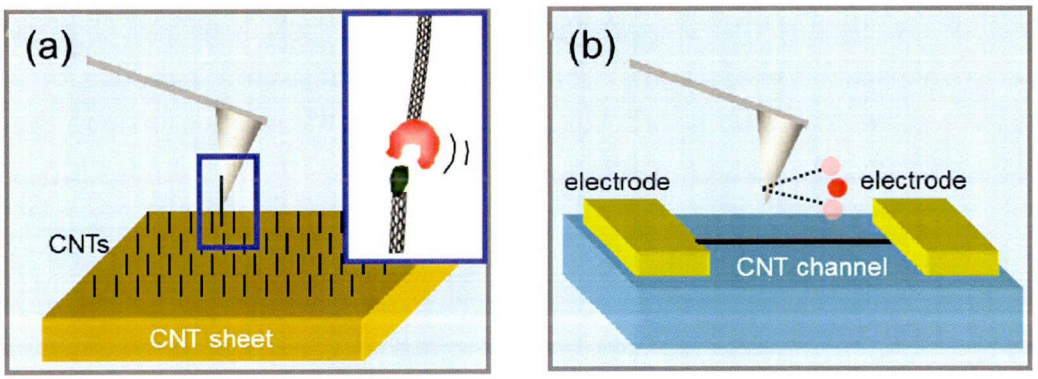

Fig. 3.9 Schematics of the proposed biosensors using CNT arms for (a) the interaction force measurement and (b) the mass measurement intended for a single protein molecule using a CNT-FET with a floating gate of a CNT arm.

3.6 Summary

Numerous nanodevices using different approaches have been demonstrated. This section presents brief summaries for several reported devices including biomolecular motors, chemomechanically driven polymers or gels, and CNT devices. Then, frameworks of three nanodevices studied in this thesis: (1) nano-oscillator, (2) nanotorsional actuator, and (3) biosensor for a single protein molecule, which are addressed in later chapters, are described. These three devices maximize the unique and specific properties of CNTs and offer great potential for use as future nanodevices.

Chapter 4 Nano-oscillator

4.1 Introduction

Carbon nanostructures are of great interest for their potential in the design of nanosized electromechanical devices because of their unique mechanical and electrical properties, as described in chapter 2. An attractive property for future devices is the remarkably low friction that exists between CNT layers [5,6]. Consequently, several functional devices such as memory [73], motors [62], actuators [61], and oscillators [68] have been reported based on the low friction of carbon nanotubes. Our group previously investigated a synthetic linear motor consisting of a capsule-like short CNT (CNT capsule) [67]. The TEM observation revealed that the CNT capsule traveled back and forth between both ends of the hollow space along the axial direction at room temperature (289 K). The ideal frequency of the thermally induced back-and-forth linear motion was estimated as 10^4 Hz at room temperature based on TEM experiments and molecular dynamics simulations [74]. This unique phenomenon offers great potential for application to nanodevices using linear motions of nanomaterials in CNTs. An extremely effective application of this high-speed linear motion is a nano-oscillator working at GHz order proposed by Legoas *et al.* [68], as described in section 3.5.1. However, the mechanism of the linear motion of the CNT capsules remains under investigation. In addition, nanoengineering for fabricating the nano-oscillator is an important subject. Therefore, detailed elucidation of this phenomenon and development of fundamental techniques to manufacture CNTs present important value for realization of the oscillator.

In this chapter, thermal energy effects on the linear motion of CNT capsules are discussed from TEM observations. In addition, in the sense of a designable device, the oscillator fabrication process is described. The ideal oscillator consists of a CNT capsule in a dumbbell-shaped CNT. The dumbbell-shaped CNTs are fabricated by application of current with tensile stress using TEM manipulation. Finally, the possibility of the oscillator from perspective of its response-speed based on the operation mechanism of the linear motion of CNT capsules and the oscillator fabrication process are discussed.

4.2 Principle of the nano-oscillator

The oscillator devices can work with a CNT capsule encapsulated in an external nanotube having both ends open, as depicted in Fig. 4.1. In this system, the van der Waals potential energy between the CNT capsule and the outer CNT is expressed as

$$U(x) = -\frac{A}{12\pi d^2} \cdot 2\pi r X = -\frac{Ar}{6d^2} \cdot X \tag{4.1}$$

from eqs. (2.1 and 2.2), where A is the Hamaker constant of CNTs, d denotes the distance between the layers, and r is the average radius of the inner and outer tube. The potential energy is proportional to the overlapped distance X. When the CNT capsule is encapsulated completely in the outer CNT as depicted in Fig. 4.1(a), the van der Waals potential energy is given as shown below.

$$U(x) = -\frac{Ar}{6d^2} \cdot 2L \tag{4.2}$$

Therein, the CNT capsule length is $2L$. Because the potential energy is constant irrespective of the CNT capsule position, the force applied to the CNT capsule from the axis direction becomes zero by the following equation.

$$F = -\frac{dU}{dx} = 0 \tag{4.3}$$

In contrast, when the part of the CNT capsule is protruded from the outer CNT as depicted in Fig. 4.1(b), the van der Waals energy is given as

$$U(x) = -\frac{Ar}{6d^2} \cdot (L + L' - x) \tag{4.4}$$

Differentiating the potential energy above by x gives the constant force.

$$F = -\frac{dU}{dx} = -\frac{Ar}{6d^2} \tag{4.5}$$

This force works to pull the CNT capsule back into the outer CNT. The distribution of total potential energy for the system is displayed as a mortar shape, as depicted in Fig. 4.1(c). In this system, once the CNT capsule starts to move with a certain initial velocity, the CNT capsule ideally repeats back-and-forth motions supported by the extracting force at both opened ends of outer CNT. The frequency of the back-and-forth motion is calculable with the length of the outer CNT and the initial velocity of the CNT capsule. For example, using a CNT capsule (diameter: 0.7 nm, length: 4.4 nm) encapsulated in an outer CNT (diameter: 1.4 nm, length: 8 nm), the maximum initial velocity is approximately 1200 m/s (the CNT capsule would go out from the outer CNT if the initial velocity exceeded the value), and the frequency reaches 33 GHz.

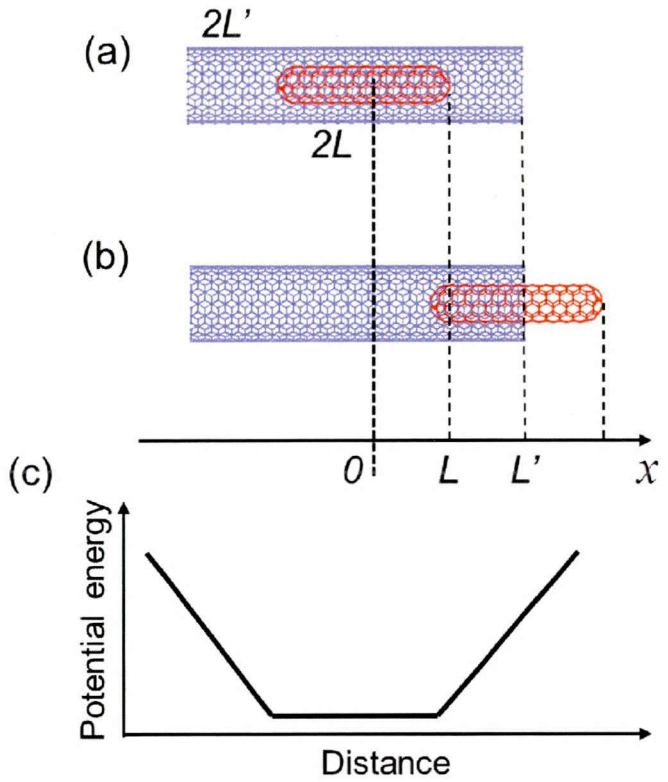

Fig. 4.1 Schematics for a CNT capsule encapsulated in an outer CNT. (a) The whole CNT capsule is in the outer CNT. (b) The part of the CNT capsule protrudes from the edge of the outer CNT. (c) Distribution of potential energy for the system determined by the van der Waals interaction between the CNT capsule and the outer CNT.

4.3 Experimental methods

4.3.1 Preparing carbon nanotube capsules

We started from encapsulating C_{60} molecules in single-wall CNTs. In this experiment, we used single-wall CNTs produced using CVD methods, as shown in Fig. 4.2(a). Because CVD grown CNTs are normally closed with caps, we heated the CNTs at 723 K in air to remove the caps and thereby create entrance holes for C_{60} molecules. Those CNTs with open ends and C_{60} molecules were put in a glass tube, which was then evacuated and closed in vacuum, as shown in Fig. 4.2(d). Those glass tube samples were heated at 673 K for 24 hr. During heating, C_{60} molecules were sublimated and were automatically encapsulated in CNTs from their opened ends. Figure 4.2(b)

displays those CNTs having C_{60} molecules inside: so-called peapods.

The CNT capsules were formed by coalescence of C_{60} molecules encapsulated in CNTs assisted by heat treatment in vacuum. The CNT capsule length is determined by the number of coalesced C_{60} molecules. In this study, we obtained CNT capsules with 3–10 nm lengths encapsulated in the interior of host CNTs by heating at 1273 K for 8 hr, as portrayed in Fig. 4.2(c).

The CNT capsules were observed using a transmission electron microscope (TEM, JEM-2500SE; JEOL). The equipment was tuned with a 90 kV acceleration voltage to reduce additional structural changes in the carbon materials caused by electron irradiation. The sample temperature was controlled from room temperature to 1073 K in the TEM with a heating holder.

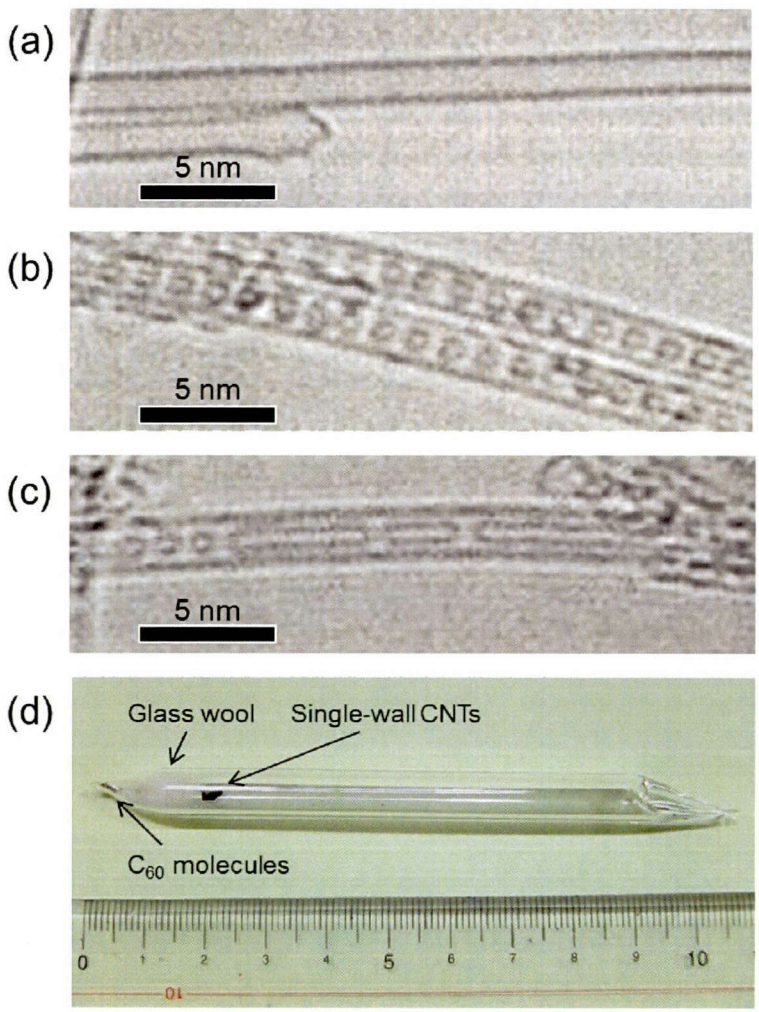

Fig. 4.1 TEM images of (a) single-wall CNTs, (b) C_{60} peapods, and (c) CNT capsules. (d) Single-wall CNTs and C_{60} molecules encapsulated in a glass tube in vacuum.

4.3.2 TEM manipulations

Experiments described in section 4.5 were conducted using TEM with a specially designed manipulation holder as presented below. Figure 4.3(a) presents a schematic for the manipulation system. CNTs were aligned and protruded from a sharpened edge of a Pt-coated Si substrate to produce a CNT cartridge as shown in Fig. 4.3(b). For the experiment, multiwall CNTs with high crystallinity were prepared using an arc-discharge method as shown in Fig. 4.3(d). The diameters of those CNTs were 10–20 nm. The CNT cartridge was set on a piezoelectric-driven manipulator stage installed in the TEM. A cantilever for a scanning probe microscope with a Pt-coated Si tip was set on the other stage, as shown in Fig. 4.3(b).

The manipulator is designed to provide applied voltage between the two stages. The force on the CNT bridged between the two stages above can be estimated from the cantilever deflection.

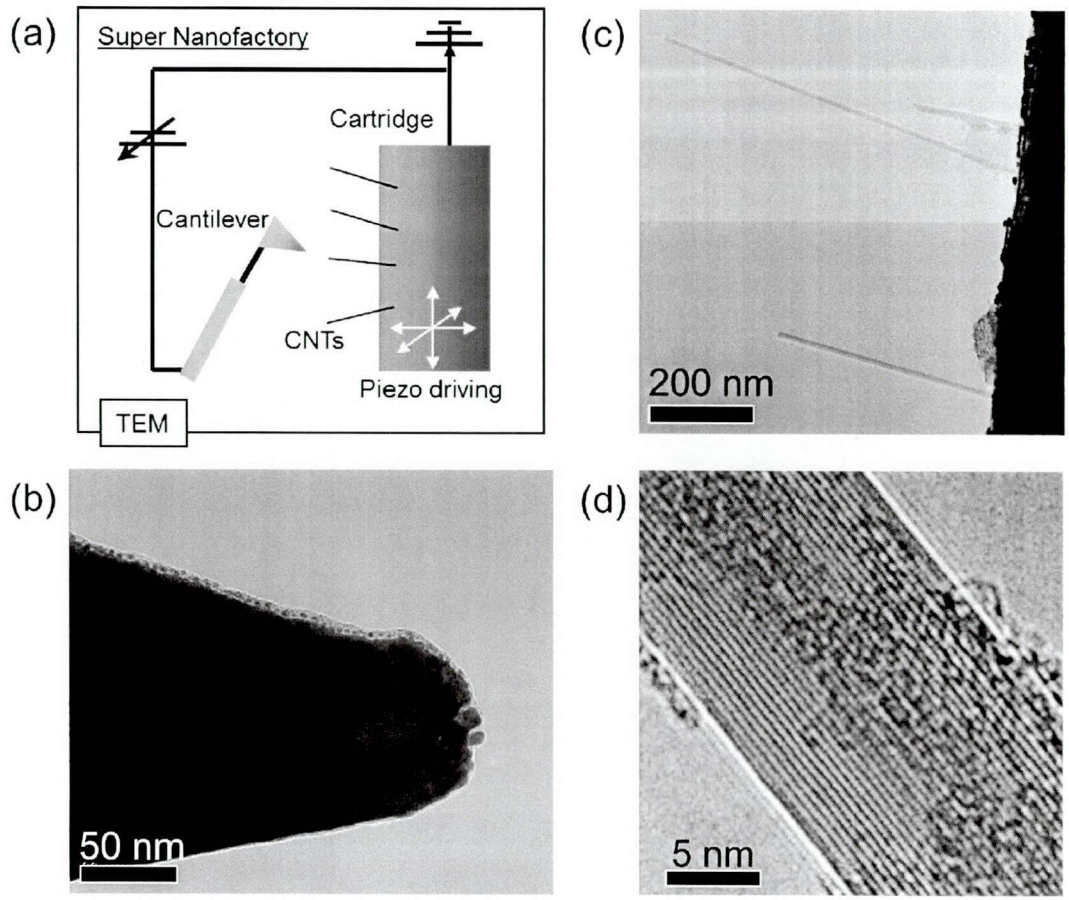

Fig. 4.3 (a) Schematic showing a TEM manipulation system: a "Super Nanofactory". TEM images showing (b) the tip of a Pt-coated Si probe for a scanning probe microscope, (c) a part of a CNT cartridge and (d) a multiwall CNT prepared using the arc-discharge method used in the experiments.

4.4 Thermally induced linear motion

Figure 4.4 presents linear motions of a CNT capsule at 673 K. At this temperature, CNT capsule A (see Fig. 4.4(a)) travels back and forth in a hollow space formed by the other two capsules. The respective CNT capsule A length and diameter are approximately 3.8 nm and 1.1 nm. The capsule normally stays at either end of the hollow space, as at room temperature, as described in a previous report [67]. For example, Figs. 4.4(b) and 4.4(c) respectively portray the capsule at the left and right side end in the hollow space. It is difficult to capture a moment when the capsule is traversing the space in the present experiments. However, an image exhibiting the presence of the capsule at both ends, as portrayed in Fig. 4.4(d) is captured, which scarcely occurs at room temperature, but which indicates that the capsule travels back and forth more than once within a capture time of the image (one frame of the movie: 0.5 s). The probability of such an image being captured was about 9% for images taken at 673 K.

Figure 4.4(f) presents the normalized density measured along the dotted line presented in Fig. 4.4(e). High density indicates that the probability of carbon atom presence is high. The density curve has four high peaks corresponding to the edges of the capsule at both ends in the space. When the capsule goes to either end in the hollow space, van der Waals (vdW) interaction functions between a cap of the capsule and a cap of the fixed capsules. Then the system has potential valleys, as presented in Fig. 4.4(j). The estimated vdW energy is given as E =500 meV from

$$E = -\frac{A}{12d}\frac{D_1 D_2}{(D_1 + D_2)}, \tag{4.6}$$

where A=6×10^{-19} J is the Hamaker constant of CNTs [75], D_1=D_2=1.1 nm is the diameter of the cap of the capsules, and d=0.34 nm represents the distance between the caps.

In our system, unfortunately, it is difficult to measure the frequency, which shows how many times the capsule escapes the above potential valley in one frame of the movie. However, if the operation results from thermal energy, then the Arrhenius equation

$$f = f_0 \cdot \exp\left(-\frac{E}{k_B T}\right) \tag{4.7}$$

gives the frequency f = 10^6 Hz at 627 K, where K_B stands for Boltzmann's constant (1.38×10^{-23} J/K), T denotes the system temperature (627 K), and f_0 10^8 Hz represents the

prefactor to which a resonance frequency of a simple oscillator model was applied. Consequently, f_0 is given as

$$f_0 = \frac{1}{2\pi}\sqrt{\frac{k}{m}}, \tag{4.8}$$

for a capsule of weight m and spring constant k estimated from the vdW energy (see details in an earlier report [74]). The estimated high-frequency motion provides an image exhibiting the presence of the CNT capsule at both ends of the hollow space, as presented in Fig. 4.4(c).

When the temperature increases to 1073 K, the CNT capsule B (see Fig. 4.4(a)), which did not move at 673 K, starts to move. Capsule B is approximately 6.5 nm long, which is almost two times longer than that of capsule A, with 1.1 nm diameter at the thickest part. The capsule is trapped at either end in the hollow space, just as at the lower temperature of 673 K, as shown in Figs. 4.5(a) and 4.5(b). At this temperature of 1073 K, however, the capsule image is also captured at the middle in the hollow space, as presented in Fig. 4.5(c). The probability of trapping somewhere in the hollow space other than at either end is almost equal to that of trapping at either end.

A possible reason for these trappings in the hollow space is that the thermally fluctuated wall of the outer CNT prevents the capsule from transport. The repulsion force, the so-called undulation force, which is affected strongly by the thermal energy of the system, is known to function between two waving layers when they are thermally fluctuated. The below equation expressing the repulsive undulation force per unit area was derived by R. Servuss and W. Helfrich from their study on mutual adhesion of lecithin bilayers [76].

$$P = \frac{(k_B T)^2}{2k_b t^3} \tag{4.9}$$

By assuming a CNT capsule and an outer CNT as a bilayer, the undulation force can be adapted to our system. For example, at 1073 K, undulation force P between the capsule and the outer CNT per unit area is calculated as 1.2×10^7 Pa from eq. (4.9), where k_b is the bending modulus of CNT (1.4 eV)[77], t denotes the distance between the capsule and the outer CNT, which is probably 0.34 nm on average. Then, multiplying the surface area of capsule B by the P value, the braking force for the capsule motion is estimated as 0.23 nN. With this value, energy of 7.2 eV is required to travel from the end to the other end of the space with no breaks. In contrast, for capsule A at 673 K as presented in Fig. 4.4, the energy of 1.5 eV is sufficient for one-way travel with no

breaks. In fact, because the undulation force works locally, the energies described above are overestimated. However, the braking effect of thermally fluctuated walls well explains why the capsule stopped at the middle in the hollow space only in the case of 1073 K. Moreover, an obstruction attributable to the thermal fluctuated walls is apparent in a previous study with MD simulations [74].

Figure 4.5(d) also exhibits the capsule at several positions in the hollow space. The normalized density along the dotted line indicated in Fig. 4.5(e) is presented in Fig. 4.5(g). It has several clear peaks aside from those at both ends, which reflect the positions of the edges of the capsule trapped at corresponding places for a certain period (see insets presented in Fig. 4.5(f)). Moreover, small peaks indicated by arrows in Fig. 4.5(g) show trapping of the capsule for a rather short period. These results strongly suggest that the capsule moves actively at the high temperature even while the motion is prevented by thermal fluctuation of the outer CNT wall. The fact that the capsule is trapped at some positions with high probability suggests that the outer CNT wall has some defects (vacancy or topological defect) [78], which reduce the potential energy for the capsule because stopping of the capsule by competition between the thermal activation of the motion and thermal obstruction occurs at random positions.

In our system, the sample was heated uniformly and was observed after reaching a sufficiently steady state. Therefore, thermophoresis, which has been inferred as a driving force of the capsules [79–82], is actually not the driving force. The breakdown of vdW interactions between the caps of the capsules by an electron beam [83] is also not the driving force because the effect of the electron irradiation does not explain the temperature dependence of the capsule motion described above.

Because spring constant k estimated from the vdW interaction between caps is a function of the mass, i.e. the capsule length, the resonance frequency f_0 of the capsule decreases as the length of the capsule increases from eq. (4.8). Consequently, capsule B requires a higher temperature than capsule A for movement based on the Arrhenius equation (eq. (4.7)). Capsule B requires approximately 700 K to obtain the same frequency of capsule A at 673 K. In addition, the longer capsule at higher temperature suffers from a greater obstruction force from the outer CNT by the thermal fluctuation of its wall, as described above. The net temperature for the motion of the capsule is balanced between the activating energy and the obstruction effect from the thermally fluctuated wall provided at that temperature. Therefore, the temperature that is necessary for moving capsule B was much higher than 700 K. Nevertheless, we do not yet understand why capsule A did not move at 1073 K.

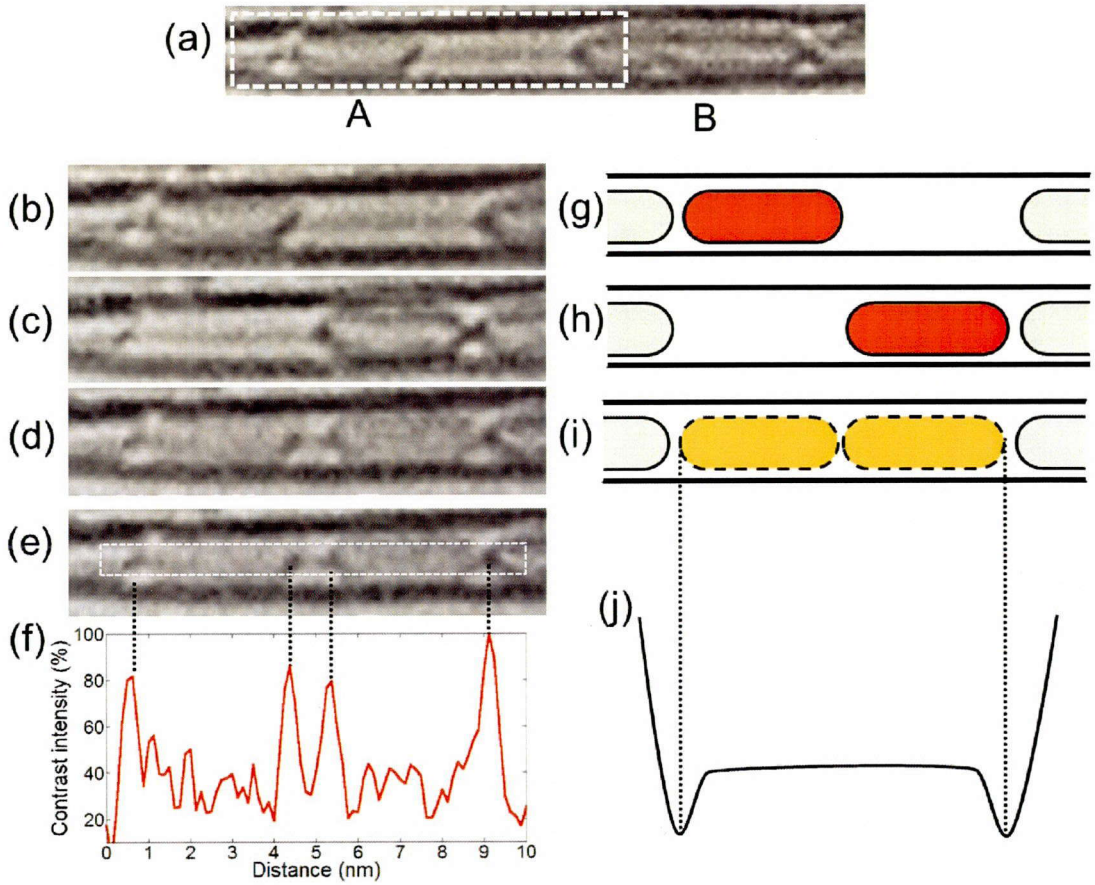

Fig. 4.4 Linear motion of a CNT capsule at 673 K in a hollow space constructed by other fixed CNT capsules in an outer CNT: (a) TEM image of the initial state of two CNT capsules A and B. (b), (c) TEM images of CNT capsule A at the left and right end, respectively. (d) TEM image showing capsule A at both ends. (e) The TEM image shown in (c) has a dotted line on which the image density was measured. (f) Normalized density curve on the dotted line in (e). (g)–(i) Schematics of TEM images of (b)–(d), respectively. (j) Schematic of the potential energy in the tube.

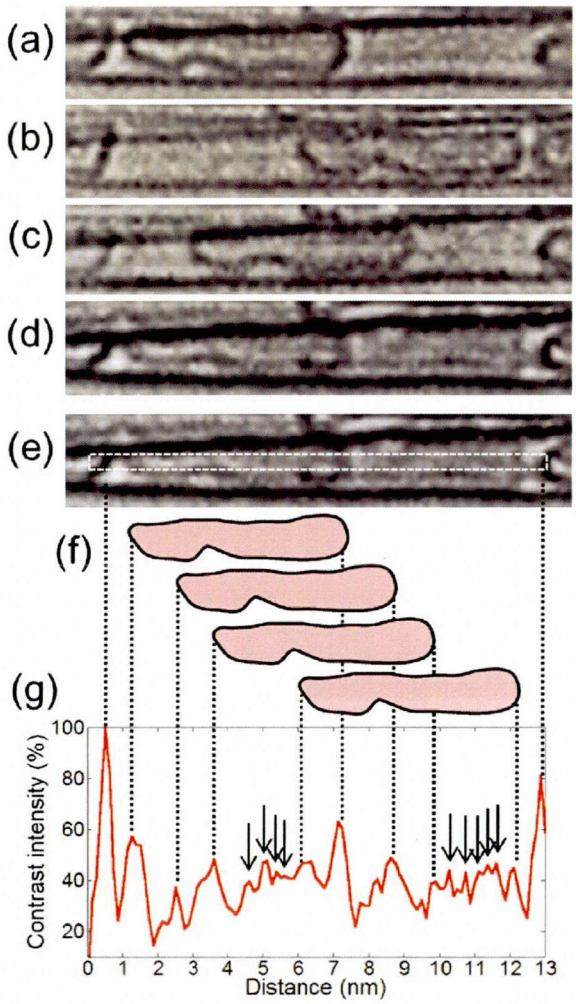

Fig. 4.5 Linear motion of a CNT capsule at 1073 K: (a), (b) TEM images of CNT capsule B, presented in Fig. 4.4(a), at the left and right end of the hollow space, respectively. (c) TEM image of capsule B trapped at the middle in the hollow space. (d) TEM image showing weak contrasts of capsule B at several points in the hollow space. (e) TEM image shown in (d) with a dotted line with which the density of the image was measured. (f) Schematics of the capsule trapped at several points in the hollow space. (g) Normalized density curve on the dotted line in (e).

4.5 Fabrication of dumbbell-shaped carbon nanotubes

In terms of working devices, a single CNT capsule should be put in a dumbbell-shaped CNT in which two thicker CNTs are fused at both ends of a thinner CNT as described in section 3.5.1. To fabricate such a complicated configuration, development of nanoengineering in TEM including a cutting, a joining, and plastic deformations of several kinds intended for a single CNT are necessary. Especially,

joining two CNTs with different diameters is a difficult challenge. If one could change a part of diameter, or chirality, in a single CNT like a dumbbell-shaped CNT, then the range of application could be explored. For example, a semiconductive CNT in which both ends are fused by metallic CNTs with a different chirality will function as a metal–insulator–metal made solely from CNTs.

Several means can be used to alter an individual CNT's diameter, including plumbing [84], sublimation induced by Joule heating [85,86], and elongation with application of current [53,87]. The joining process has a broad utility, but it requires catalyst particles to connect a pair of CNTs having a large diameter difference. Moreover, it is difficult to control the process.

Sharpening CNTs induced by sublimation is a rather simple means to control the diameter. One report described a method to sharpen an individual CNT controllably using resistive heating. In this case, the center of a suspended CNT was shrunk. Eventually, hypodermic syringe-like tips were formed [85]. Our group has also demonstrated a process for forming cone shape CNT tips induced by rapid current increasing [86]. In these sublimation processes, the value of the current determines the sublimation rate of carbon atoms and therefore the resultant configuration of sharpened CNT tip. For example, the rate stated in our group's previous report [86] is ca. 10^4 atoms/s, forming a cone shape tip, but the rate calculated from the work reported by T. Yuzvinsky *et al.* [85] was ca. 10 atoms/s, resulting in syringe-like CNT tips. That structural difference results from the difference of sublimation energies of carbon atoms from the hexagon and from 5–7 defects. According to our previous report [86], at the lower temperature, sublimation starts from 5–7 unstable defects and only slightly from a stable hexagon. Syringe-like structures result from sublimation from 5–7 defects and propagation of 5–7 defects along the axis. In contrast, under higher temperatures, sublimation starts from hexagons as well as from 5–7 defects simultaneously from the center region. Conical structures are the results of the sublimation amounts depending on the temperature, which is distributed parabolically along the CNT axis. Then the lower sublimation rate is apparently suitable for fabrication of dumbbell-shaped CNTs. However, because the electrical resistance is changed as the diameter changes, it is difficult to control the current. It is also difficult to control the CNT diameter.

Plastically elongated CNTs also have different diameters in an individual CNT. One report described superplastic elongation of a single-wall CNT by the combination of resistive heating and mechanical pulling [87]. Our group has demonstrated structural changes in an isolated carbon nanotube during plastic elongation using TEM equipped with a nanomanipulation system [53]. A salient benefit of the elongation process is that

the diameter can be controlled to a fine degree. In our previous report [53], nanobeam electron diffraction reveals the chiral indices of the nanotube decrease by (1, 1), when tensile stress and electroresistive heating are applied simultaneously. The circumferential current density is maintained at 1.0 μA/nm, which is smaller than the value for the sublimation of CNTs (2.2 μA/nm) [88]. The elongation process is more controllable than the sublimation process, but it is unsuitable for the fabrication necessary for large diameter change in a short length.

As described herein, dumbbell-shaped CNTs were fabricated by application of current under tensile stress, taking advantage of both sublimation and elongation processes.

We first prepared a hollow CNT, as portrayed in Fig. 4.6(a), by extracting inner layers from multiwall CNT produced using the arc-discharge method. Details of that extraction process are described later in section 5.3. A hollow CNT was bridged between electrodes and excess current was applied to the CNT to reduce layers. The outer layers were sublimated from the middle area by Joule heating. The number of layers was decreased across the tube, as portrayed in Fig. 4.6(b) with gradual decrease of the current, as indicated by the red line in Fig. 4.6(e). Moreover, several layers of the middle area of the CNT were sublimated as portrayed in Fig. 4.6(c) with a rapid decrease of the current, as portrayed in Fig. 4.6(e). The thinnest part of the CNT had four layers. It was approximately 70 nm long, as portrayed in Fig. 4.6(d).

Figures 4.7(a)–4.7(e) portray sequential TEM images of a shrinking process of the CNT. In this process, a certain tensile stress was applied to the CNT, and the voltage was fixed at 3.0–3.2 V. Figure 4.7(g) stands for the diameter changing of the middle area of the CNT. The diameter decreases gradually and the current decreases correspondingly, as indicated by the red line in Fig. 4.7(f). In contrast, the circumferential current density given by $J=I/\pi d$, where I represents current and d is the diameter of the thinnest part, increases through the process as portrayed in Fig. 4.7(h). In addition, results show that the resultant CNT is stretched by approximately 10 nm from the initial state by comparing an edge of outer most layer between Figs. 4.7(a) and 4.7(e) (the broken line is a visual guide). The resultant CNT has a dumbbell shape with 1.6 nm diameter in inner space at the middle region and 4.1 nm diameter at both ends, which is suitable for the outer frame of the nano-oscillator that we have proposed. The suitable shape of this dumbbell CNT is discussed later in section 4.5.2.

Dumbbell-shaped CNTs are fabricated using the thermal energy and the elastic energy induced respectively by Joule heating and tensile stress. To control the process, the balance between both energies is important. In this experiment, the structural change

starts when the circumferential current density reaches 1.65 μA/nm, which is larger than the value 1.0 μA/nm required for the elongation process described in our previous report [53] but less than the value 2.2 μA/nm for sublimation [88]. However, this structural change includes not only the migration of 5–7 defects for stretching but also the sublimation of atoms from 5–7 defects by considering the decreasing rate of the diameter. The sublimation rate is ca. 300 atoms/s, which is between the values reported in one earlier study (10 atoms/s) [85] and another (10^4 atoms/s) [86]. That value provides large diameter changes in a short distance at both sides. In addition, by application of tensile stress, fine control of diameter at the center region is possible. However the circumferential current density increases gradually in the process, as portrayed in Fig. 4.7(h) because the diameter decreases at a high rate under tensile stress. When the circumferential current density increases to greater than 2.2 μA/nm, the sublimation can be dominant, which is a reason for a cut down. Therefore, the current and diameter should be monitored carefully and controlled in the process.

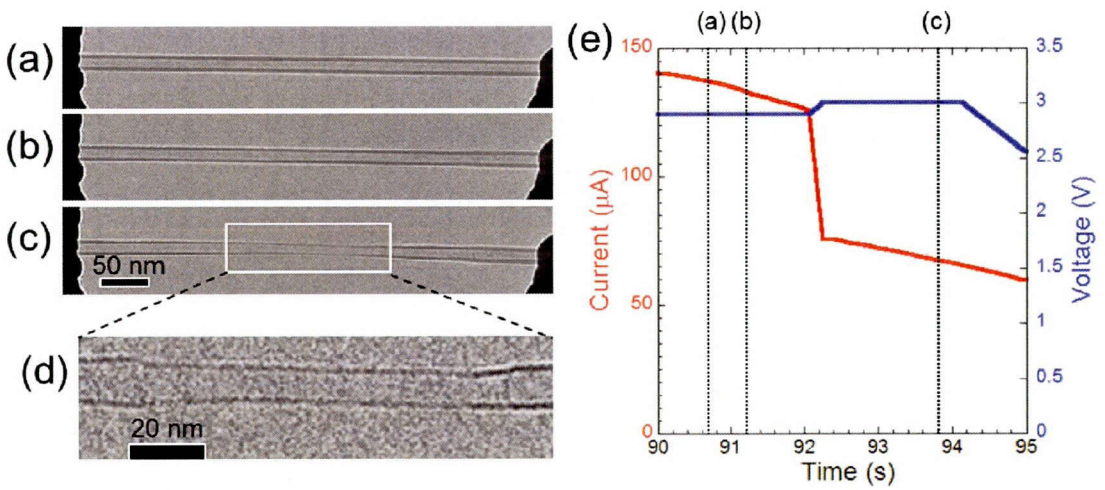

Fig. 4.6 Sublimation process of multiwall CNT. (a) Multiwall CNT in which several inner layers are extracted as bridges between the electrodes. (b) Several outer layers are sublimated along the tube. (c) More layers are sublimated at the center of the CNT. The number of layers decreases as a step toward the center of the CNT. (d) Enlarged TEM image in the white square in (c). (e) Temporal variation of the current corresponding to that of the voltage applied to the CNT. Points designated as a–c correspond to TEM images (a)–(c).

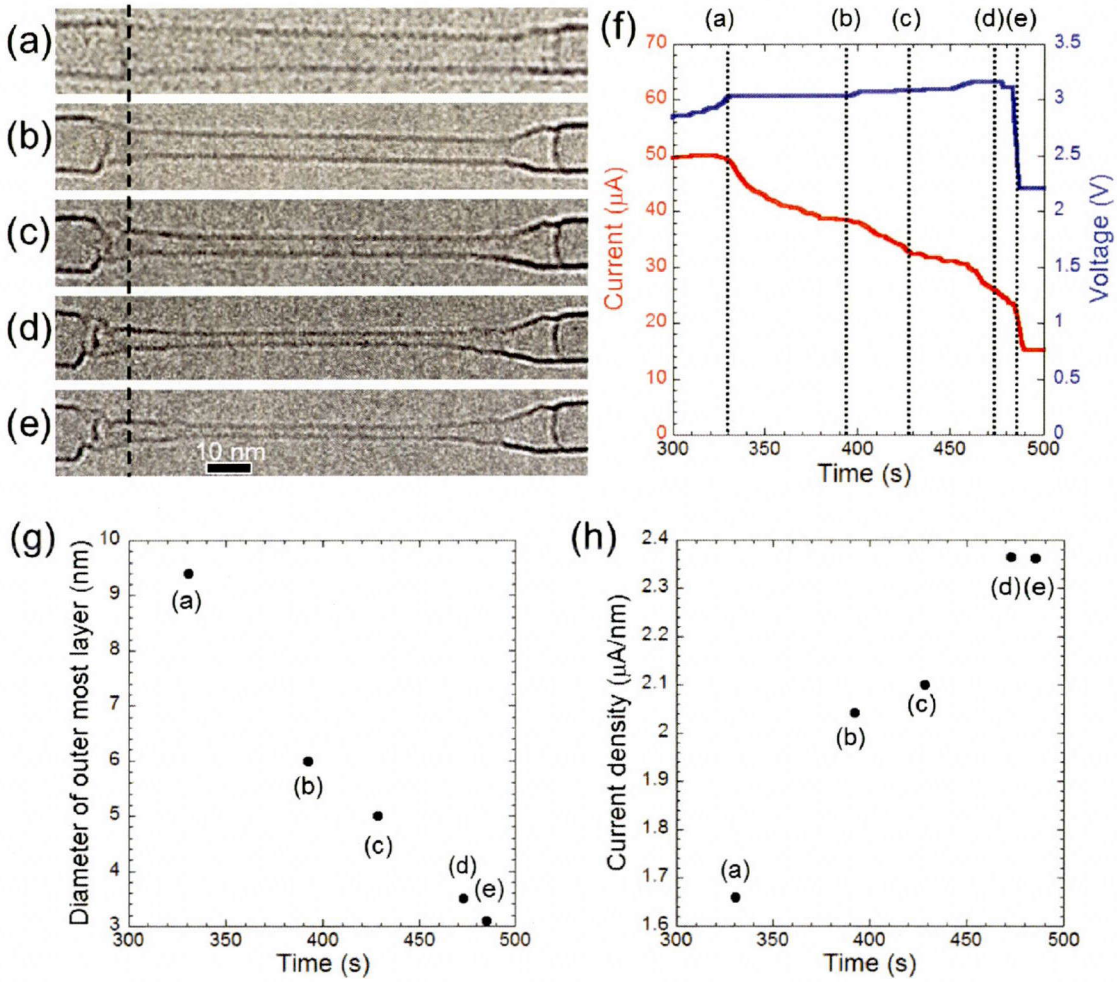

Fig. 4.7 Dumbbell-shaped CNT fabrication process. (a)–(e) Sequential TEM images of the multiwall CNT, which is displayed in Fig. 4.6 during processing. In the process, the diameter of center area of the CNT decreases and the CNT stretches by ca. 9 nm. The broken line on TEM images shows the initial position of the left side edge of the outermost layer. Temporal variation of (f) the current corresponding to that of the voltage applied to the CNT, (g) the diameter at the center region and (h) the circumferential current density during the process. All points designated as a–e in (f)–(h) correspond to TEM images (a)–(e).

4.6 Discussion

4.6.1 Frequency of the oscillator

In the system described in section 4.4, CNT capsules travel back and forth in a space formed by two other CNT capsules. Therefore, the system has a potential valley at both ends, as portrayed in Fig. 4.8(a). Although it is difficult to observe the high-speed

back-and-forth motion of in the TEM directly, images exhibiting the presence of the capsule at both ends such as those in Fig. 4.4(d) present the strong possibility of high-speed motion. According to the Arrhenius equation, the estimated frequency of back-and-forth motion can be 10^4 Hz at room temperature. Moreover, introducing dumbbell-shaped CNTs as described in section 4.5, the potential valleys can be removed as portrayed in Fig. 4.8(b). In this system, the frequency can be much larger than the system as portrayed in Fig. 4.8(a). Ideally, once the CNT capsule starts to move with a certain initial velocity, the CNT capsule repeats back-and-forth motions supported by the extracting force at both opened ends of outer CNT. The frequency of the back-and-forth motion is calculable with the length of the outer CNT and the initial velocity of the CNT capsule (see section 3.5.1 for details). For example, using a CNT capsule (0.7 nm diameter; 4.4 nm length) encapsulated in an outer CNT (1.4 nm diameter; 8 nm length), the maximum initial velocity is approximately 1200 m/s (the CNT capsule would go out from the outer CNT if the initial velocity exceeds the value), and the frequency reaches 33 GHz. However this calculation does not concern the effect of thermal fluctuation of the wall. In our experiment, thermal fluctuation at 1073 K worked as obstruction and stopped the motion of the CNT capsules. To design the device, we must assess the effect of thermal energy to the linear motion more deeply, and for this subject, it is important to observe its frequency as a function of temperature, which remains as a subject for additional study.

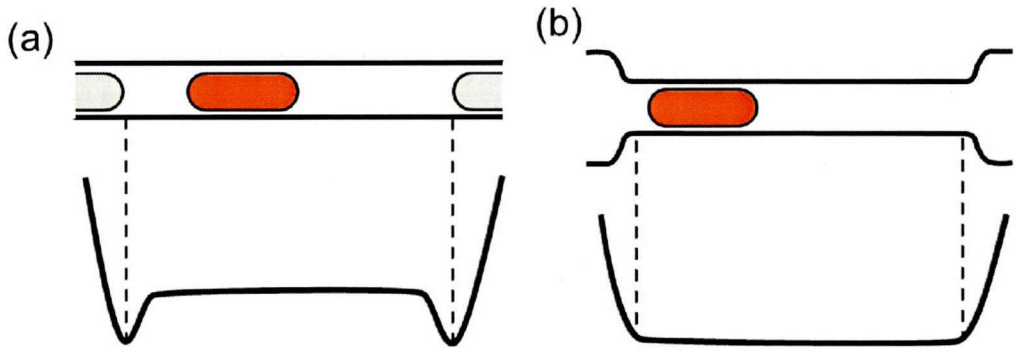

Fig. 4.8 Schematics of two types oscillating system and potential energy. (a) A CNT capsule oscillates in a space formed by two other capsules. (b) A CNT capsule oscillates in a dumbbell-shaped CNT.

4.6.2 Assessment of dumbbell-shaped carbon nanotubes

The configuration of tapers between thinner and thicker parts in a dumbbell-shaped CNT is also important for designing the nano-oscillator. Figure 4.9(a) portrays a resultant dumbbell-shaped CNT as described in section 4.5. Figures 4.9(b) and 4.9(c)

present an enlarged image and its schematic in the white square in Fig. 4.9(a) where two steps of tapers exist between thinner part and thicker part. In taper I presented in Fig. 4.9(c), the diameter is 1.6–2.2 nm with 6.1 nm length. The angle of this taper is approximately 3°. In contrast, taper II is more precipitous; its angle is 20–30°. In this case, by assuming that the taper is expanded uniformly, as shown in the schematics of Fig. 4.9(d) as a simple model, the van der Waals energy is given as

$$U(x) = -\frac{Ar}{6d} \cdot \left\{ \frac{(2L-x)}{d} + \frac{x}{px+d} \right\}, \tag{4.10}$$

where A is the Hamaker constant of CNTs, d denotes the distance between layers, r is the radius of inner tube, x is the length protruded from thinnest part, and p is a gradient of tapers (0.05 and 0.45 for tapers I and II, respectively). By differentiating the potential energy above, the force shown in the following equation is obtained.

$$F(x) = -\frac{Ar}{6} \cdot \left\{ \frac{1}{d^2} - \frac{1}{(px+d)^2} \right\} \tag{4.11}$$

Figure 4.9(e) presents the distribution of the force corresponding to the distance from the end of the thinnest part of the dumbbell-shaped CNT. This force works to pull the CNT capsule back into the thinnest part of the CNT. In that graph, the integral value of the area under the line represents the work done by the CNT capsule. To obtain oscillating motions, the capsule length should be designed to make the amount of the work higher than the kinetic energy of the CNT capsule. In this case, more than 1000 m/s of initial velocity is necessary to generate gigahertz-order oscillation. Corresponding to that initial velocity, the CNT capsule length should be longer than 7 nm to prevent the CNT capsule from projecting out from the thinner part of the dumbbell-shaped CNT.

Moreover, as working devices, the CNT capsule motion must be controlled. One approach that is useful for control of the motion is the application of an electric field. By doping metal atoms in CNT capsules, CNT capsules will have a positive charge by charge transfer from the capsules to the outer CNT [89]. The CNT capsule can oscillate by application of an alternating electric field to the dumbbell-shaped CNT if such a charged CNT capsule is inserted in a dumbbell-shaped CNT consisting of a semiconductive CNT of which both ends are fused by thicker metallic CNTs. This system is not only attractive for future devices such as generators; it is also helpful to ascertain the phenomenon more deeply.

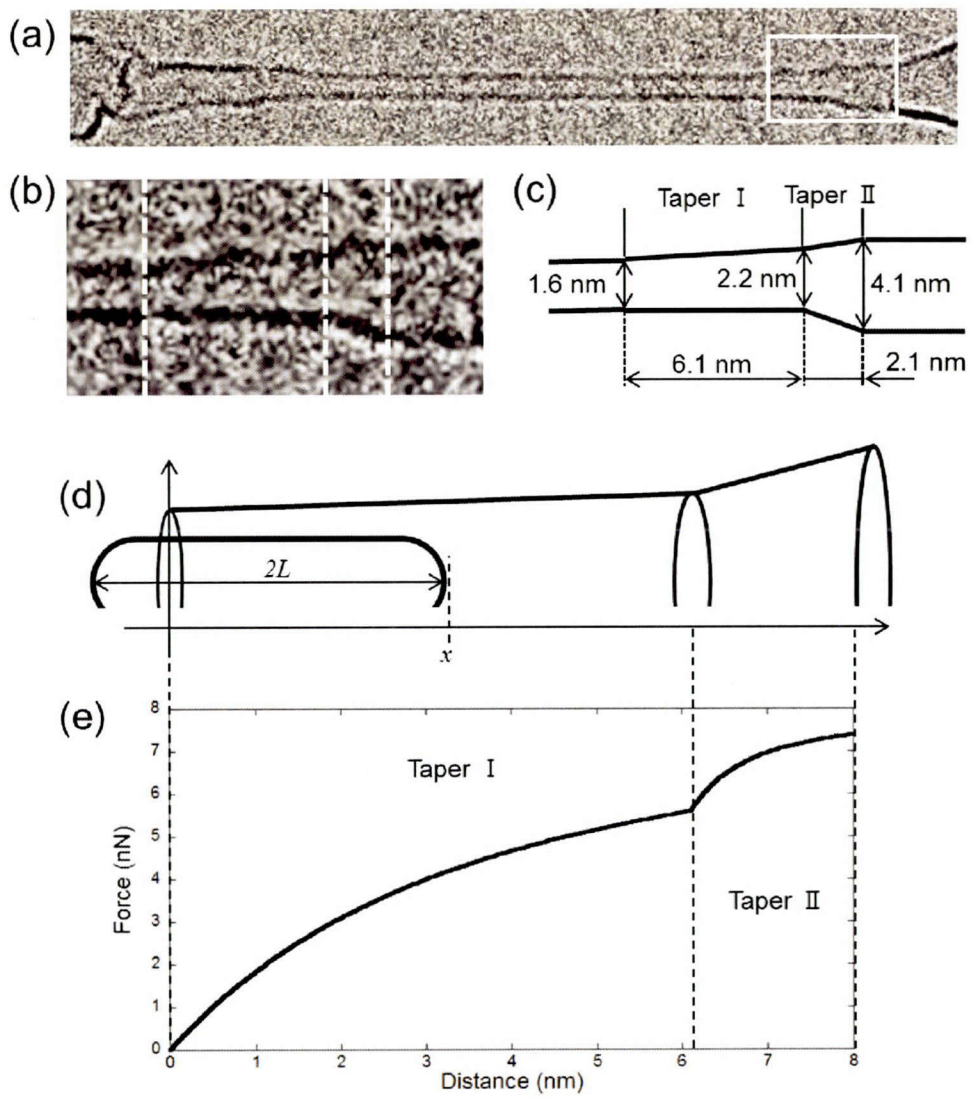

Fig. 4.9 TEM images and schematics of a resultant dumbbell-shaped CNT. (a) A TEM image of a dumbbell-shaped CNT displayed in Fig. 4.7(e). (b) Enlarged TEM image and (c) schematics in the white square in (a). (d) Model of uniformly expanded dumbbell-shaped CNT and a CNT capsule designed from (c). (e) The van der Waals force acting to the capsule shown against distance x appeared in (d).

4.6 Summary

At the high temperature of 673 K, the linear motion of the CNT capsules in the hollow space in the outer CNT is more active than at room temperature. The frequency of back-and-forth movement for the CNT capsules is at least higher than the video rate

of the observation. A temperature as high as 1073 K obstructs the travel of the CNT capsules and activation of the linear motion. The most probable origin of the obstruction is the thermal fluctuation of the sidewall of the outer CNT. The driving force of the linear motion of the CNT capsules is inferred to be thermal energy.

The dumbbell-shaped CNT was fabricated with Joule heating and application of tensile stress. In the process, the sublimation of atoms from 5–7 defects starts from the center of the bridged CNT with tensile stress as well as migration of 5–7 defects at 1.6 μA/nm of circumferential current density. The sublimation rate is ca. 300 atoms/s, which is the median value between values reported previously as 10 atoms/s [85] and 10^4 atoms/s [86]. That value provides large diameter changes in a short distance at both sides and a suitable dumbbell-shaped for the nano-oscillator.

To realize the nano-oscillator, it is important to elucidate the mechanism of the linear motion more deeply, especially in a system with a single CNT capsule in a dumbbell-shaped CNT. For this subject, we must develop techniques to combine a CNT capsule and a dumbbell-shaped CNT and observe its frequency in accuracy as a function of temperature. Those remain as subjects for additional study.

Chapter 5 Nanotorsional actuator

5.1 Introduction

Development of actuators that convert external energy such as electrical, thermal, and chemical energy to kinetic energy in a nanoworld is a great challenge in the field of nanotechnology. Especially, nanoactuators, which provide well controlled movement in a range of environmental conditions with rapid response and long cycling lifetime are promising for use in more functional devices such as nanorobots. This chapter presents a nanoactuator with a new function consisting of a carbon nanotube (CNT). It can serve as a component actuator for future nanosized devices.

Transmission electron microscopic (TEM) observations have revealed that a thick CNT can operate as a torsional actuator: a CNT in a flattened state that is energetically stable at room temperature changes reversibly to a tubular state depending on the amount of current applied to the CNT. In fact, the flattened configuration of CNTs has attracted scientific interest since the very first report of fully flattened CNTs [77], but it not been highlighted in applications. This work is highly original not only because this is the first study in which the transition between tubular and flattened states in a CNT has been experimentally demonstrated and electrically controlled, but also because it particularly addresses a device which has shown unique transition behavior.

For this study, TEM observations and molecular dynamics (MD) simulations were used to examine transition behavior and to investigate the feasibility of a nanotorsional actuator. First, the preparation of flattened CNTs and properties of those CNTs are introduced. Then, details related to state transitions are discussed based on TEM observations and MD simulations. Finally, the expected performance and the feasibility of the actuator are described.

5.2 Experimental methods

5.2.1 TEM manipulations

Experiments described in this chapter were conducted using a TEM special manipulation holder as presented below. Multiwall CNTs prepared using an arc-discharge method were aligned and protruded from a sharpened edge of a Pt-coated Si substrate to produce a so-called CNT cartridge. The CNT cartridge was set on a

piezoelectric-driven manipulator stage installed in TEM (2500SE; JEOL Ltd.) with 90 kV accelerating voltage. A Pt-coated Si probe used for a scanning probe microscope was set on the other stage. The Si probe tip was attached to the free end of a CNT in the CNT cartridge using the manipulator. Excess dc current was applied between the Si probe and the cartridge to cut the CNT. The cut ends were sharpened to give them a bamboo-shoot-like structure. The two sharpened tips were then overlapped and current was passed through the overlapped region. At this time, a sufficiently strong interaction was produced between the two sharpened tips. Then several inner layers of the CNT at the Si-probe-tip side were extracted by controlling the manipulator stage position. Details of these important techniques are described in section 5.3. The resultant hollow CNT was kept in air at room temperature. Then the CNT was collapsed to be energetically stable. Finally, we obtained a flattened and twisted CNT.

5.2.2 Molecular dynamics simulations

Computational studies have been useful and reliable tools for the investigation of several physical properties of nanosized materials. In fact, several studies of mechanical properties of CNTs have been undertaken using MD simulations. The work described in this chapter also used MD simulations for elucidation of the mechanism of the CNT state transition. In this simulation, the total energy of the system was composed of the combination of the short distance potential E_b for interaction among carbon bonds in CNTs and the long distance potential E_{LJ} for van der Waals interaction for the inside face of flattened CNTs as shown below.

$$E = E_b + E_{LJ} \tag{5.1}$$

Interaction among carbon atoms was described by the reactive empirical bond order (REBO) potential proposed by Brenner [90], which was based on Tersoff's [91] bond-order expression and which was optimized for small hydrocarbons, graphite, and diamond crystal. That energy E_b was expressed as the sum of the bonding energies between all atoms i and j as

$$E_b = \sum_i \sum_{j(i>j)} \left[V_R(r_{ij}) - B_{ij}^* V_A(r_{ij}) \right], \tag{5.2}$$

where $V_R(r_{ij})$ and $V_A(r_{ij})$ are repulsive and attractive force terms, respectively, as a function of the distance r_{ij} between bond i - j. Morse-type exponential functions with a cut-off function $f(r)$ were used for these terms.

$$V_R(r) = f(r) \frac{D_e}{S-1} \exp\left\{ -\beta\sqrt{2S}(r - R_e) \right\} \tag{5.3}$$

$$V_A(r) = f(r)\frac{D_e S}{S-1}\exp\left\{-\beta\sqrt{2/S}(r-R_e)\right\} \tag{5.4}$$

$$f(r) = \begin{cases} 1 & (r < R_1) \\ \frac{1}{2}\left(1+\cos\frac{r-R_1}{R_2-R_1}\pi\right) & (R_1 < r < R_2) \\ 0 & (r > R_2) \end{cases} \tag{5.5}$$

The bonding state was described through the bond order term B^* as the function of the angle θ_{ijk} between bond i - j and each neighboring bond i - k. However, Brenner's original equation had the conjugate compensation term in term B^* for simulating hydrogen terminated edges and did not take into account non-terminated small carbon clusters. To simulate those non-terminated carbon clusters, Y. Yamaguchi *et al.* removed the conjugate compensation term from Brenner's original equation and simulated the growth process of small carbon clusters [92,93]. For this thesis, the same method as that used in Y. Yamaguchi's report above was adopted. That improved bond order term B^* is described as presented below.

$$B_{ij}^* = \frac{B_{ij} + B_{ji}}{2} \tag{5.6}$$

$$B_{ij} = \left(1 + \sum_{k(\neq i,j)}\left[G_c(\theta_{ijk})f(r_{ik})\right]\right)^{-\delta} \tag{5.7}$$

$$G_c(\theta) = a_0\left(1 + \frac{c_0^2}{d_0^2} - \left(\frac{c_0^2}{d_0^2 + (1+\cos\theta)^2}\right)\right) \tag{5.8}$$

Constants used herein are presented in Table 5.1.

Table 5.1 C-C potential parameters

D_e(eV)	S	β(Å^{-1})	R_e(Å^{-1})	R_1(Å^{-1})	R_2(Å^{-1})	δ	a_0	c_0	d_0
6.325	1.29	1.5	1.315	1.7	2.0	0.80469	0.011304	19	2.5

In addition, van der Waals interaction between non-bonded carbon atoms was expressed by the Lenard–Jones potential for interaction of the CNT inside face. The total van der Waals energy E_{LJ} was expressed as the function of the distance r_{ij} between bond i - j.

$$E_{LJ} = \sum_i \sum_{j(i>j)} f_{LJ}(r_{ij})\phi_{LJ}(r_{ij}) \tag{5.9}$$

$$\phi_{LJ}(r_{ij}) = 4\varepsilon\left\{\left(\left(\frac{\sigma}{r_{ij}}\right)^{12} - \left(\frac{\sigma}{r_{ij}}\right)^{6}\right) + a\left(\frac{r_{ij}}{R_5}\right)^2 + b\right\} \tag{5.10}$$

$$f_{LJ}(r) = \begin{cases} 0 & (r < R_3) \\ \frac{1}{2}\left(1 + \cos\frac{R_3 - r}{R_4 - R_3}\pi\right) & (R_3 < r < R_4) \\ 1 & (R_4 < r < R_5) \\ 0 & (r > R_5) \end{cases} \tag{5.11}$$

The parameters ε = 2.4 meV and σ = 3.37 Å were used to describe the van der Waals potential between graphite layers per carbon atom [94]. The cut-off function f_{LJ} was divided into four ranges. To remove the effect of the repulsion force derived from Lenard–Jones potential to the covalent bonds in CNTs simulated using Brenner's potential, the calculation should be cut to less than R_3 ($>R_2$). In addition, to keep the inner faces of CNTs from approaching closer than the gap distance for graphene sheets when the CNTs become the flattened state, a sufficient potential barrier is needed; also, R_4 should be less than σ. R_5 is introduced to reduce the calculation time. Moreover, in eq. (5.10), a quadratic function was added to the normal Lenard–Jones potential to connect the function continuously at $r=R_5(=3\sigma)$. Therefore values a and b are given from the differential equations shown below.

$$\phi_{LJ}(r)\big|_{r=R_5} = 0, \quad \left.\frac{d\phi_{LJ}(r)}{dt}\right|_{r=R_5} = 0 \tag{5.12}$$

Then,

$$a = 3\left\{2\left(\frac{\sigma}{R_5}\right)^{12} - \left(\frac{\sigma}{R_5}\right)^{6}\right\}, \quad b = -7\left(\frac{\sigma}{R_5}\right)^{12} + 4\left(\frac{\sigma}{R_5}\right)^{6}. \tag{5.13}$$

Other constants that are used are shown in Table 5.2.

The velocity Verlet method was adopted to integrate the equation of motion with the time step of 0.5 fs (details in Appendix 1). Model CNTs are single-wall CNTs of about 5.4 nm diameter with several chiralities. They are flattened as an energetically stable state at room temperature. The system temperature was controlled using Berendsen scaling [95] (details in Appendix 2). The initial flattened states were prepared by application of pressure to the CNT from a direction normal to the tube axis.

Table 5.2 Lenard-Jones potential parameters

σ(meV)	ε(Å^{-1})	R_3(Å^{-1})	R_4(Å^{-1})	R_5(Å^{-1})
2.4	3.37	2.491	2.590	10.11

5.3 Extraction process

Multiwall CNTs (including double-wall and triple-wall CNTs) have nested structures, as explained in chapters 1 and 2. The range of the application will be spread if one can take out inner shells freely and control the number of layers. Recently, H. Shinohara's group developed a method to separate only inner layers from double-wall CNTs using sonication for bulk samples [96]. In the work reported by A. Zettl's group described in chapter 4, an inner shell of an isolated multiwall CNT was operated using a manipulation in TEM [5]. However, the process of operating or extracting inner shells in TEM has not been characterized well because of daunting technical challenges. Here, several important points and knowledge for operating the inner shells of multiwall CNTs are presented.

As the first step of the extraction process, a multiwall CNT was cut using excess dc current. Then, the two cut ends with sharpened tips were overlapped as presented in Fig. 5.1(a) and current was passed through the overlapped region. To extract inner layers from a multiwall CNT successfully after cutting, a sufficiently strong interaction between the faced sharpened tips must be made by this application of current. To investigate the sufficient amount of current for bonding, a certain amount of current corresponding to the applied voltage was applied for a few seconds. Then the right side CNT was pulled without current application. The amount of voltage applied to the faced CNTs was increased if those two CNTs were detached without extracting inner layers. The process described above was repeated until the inner layers of the left side CNT were extracted successfully.

Figure 5.2(a) portrays the temporal variation of the current (red line) and the voltage (blue line) for that repeated trials. For example, Fig. 5.2(b) shows the variation of the current and the voltage for the second trial, signified by the left yellow square in Fig. 5.2(a). First, the two sharpened tips are not touching. After setting the voltage to the target value (1.2 V here), the two sharpened tips are in contact, where the current increases at t=130 s. The contacted region between two CNTs is almost confined to the tips (point contact) as presented in Fig. 5.2(d). Then, the voltage is returned to zero and the right side CNT is moved right. In this trial, the two CNTs are detached.

In contrast, Fig. 5.2(c) depicts the temporal variation of the current and the voltage during the extraction process presented in Fig. 5.1(b)–5.1(d). At this time, two sharpened tips are overlapped by 5 nm (wall contact) as presented in Fig. 5.2(e). The current in Fig. 5.2(c) increases gradually after the two sharpened tips make contact (t=771 s), although the voltage does not change, which strongly suggests that the conductivity is improved by forming atomic bonds at the attached region. Then the inner shells of the left side CNT were pulled out along with the right side CNT as presented in Fig. 5.1(b)–5.1(d).

The bonding force is expected to be stronger than the van der Waals force between the walls of the inner shells and the outer shells. The value of the van der Waals force is

$$F = \frac{Ar}{6d^2}, \tag{5.14}$$

where $A = 6\times10^{-19}$ J is the Hamaker constant of CNTs [97], r signifies the radius of the inner shells, and d = 0.34 nm denotes the distance between layers. The van der Waals force is approximately 3.2 nN by application of r = 3.7 nm. Therefore, the bonding force generated by application of current is at least stronger than 3.2 nN. Our group has demonstrated that the formation of two sp^3-like bonds is a favorable atomic configuration at a very early stage of the head-to-head coalescence of two capped CNTs [98]. This report has also presented calculations of the bonding force of the several atomic configurations. According to that calculation, one sp^3-like bond and two sp^3-like bonds between two C_{60} molecules respectively cause bonding forces of ca. 15 nN and 24 nN. Although, the situation differs between the tip contact and the wall contact, the boundary between the two sharpened tips at the successful extraction process described above is thought to have more than one sp^3-like bond.

Fig. 5.1 Series of TEM images for an extraction process. (a) Two CNTs with sharpened tips are in contact. (b), (c) Left side inner shell is extracted following the right side CNT. White arrows indicate the ends of the inner shell. (d) Left side inner shell is extracted completely and the outer several layers remain at the left-side electrode.

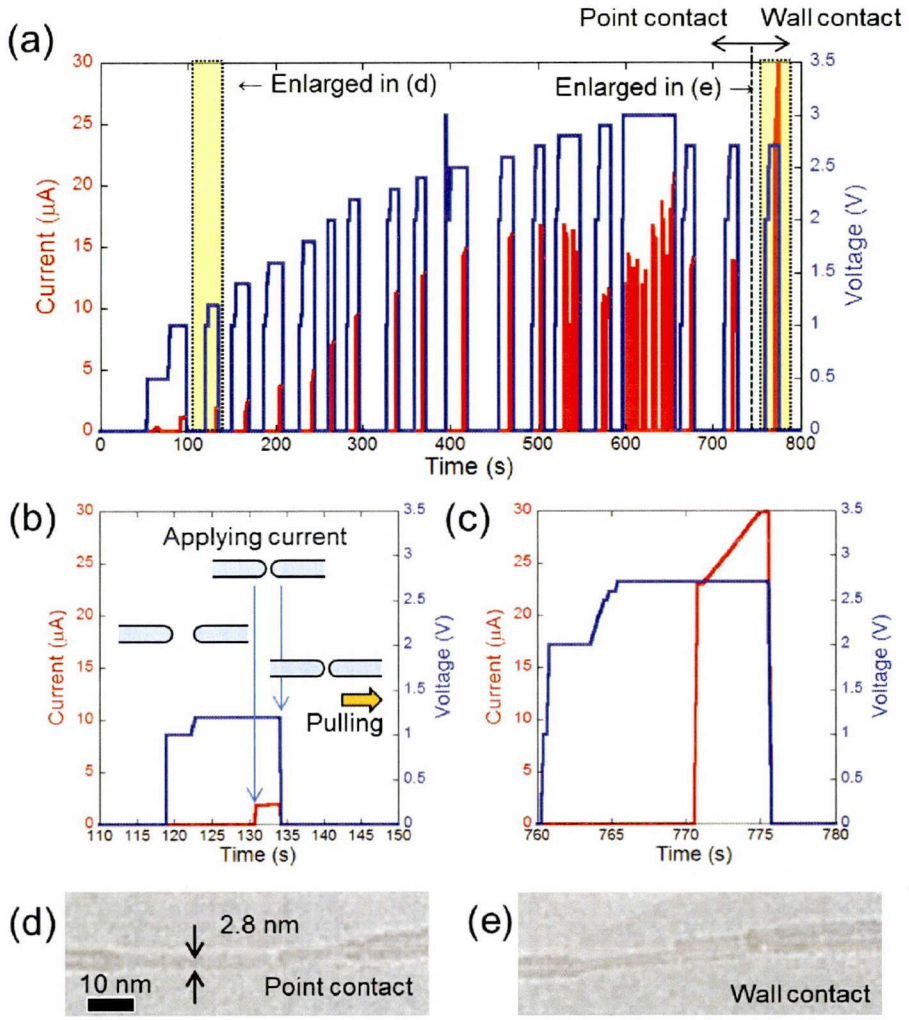

Fig. 5.2 (a) Temporal variation of the current and voltage for all trials to produce a junction between the two sharpened tips as presented in Fig. 5.1. (b), (c) Enlarged graphs of the left and right yellow squares shown in (a), respectively. Images taken using TEM for two sharpened tips in contact by (d) head-to-head and (e) wall-to-wall.

5.4 Flattened carbon nanotubes

Figure 5.3(a) presents an example of a hollow CNT soon after extracting inner layers using the processes described above. It has five layers. The CNT has 12.5 nm diameter at the innermost layer. Maintaining the CNT at room temperature for several hours changed its tubular state to a flattened state, as presented in Fig. 5.3(b). Figures 5.3(c) and 5.3(d) portray illustrations of the cross section of the innermost layer for each state. For the tubular state presented in Fig. 5.3(c), a simple energetic analysis [77] reveals the

energy per unit length of the CNT as

$$E_{tube} = \pi k_c / r, \tag{5.15}$$

where r denotes the radius of CNT and k_c = 1.4 eV signifies the curvature modulus. [77] Applying r=6.25 nm to eq. (5.15) provides E_{tube} = 0.70 eV/nm. In contrast, the flattened state presented in Fig. 5.3(d) has a two-sheeted strip and high curvature at the strip edges: so-called bulbs. The curvature energy per unit length of this structure is

$$E_{bulb} = k_c a / r_b^2, \tag{5.16}$$

where a stands for the arc length of the curved region and r_b represents the bulb radius. Applying $a = 1.65$ nm and r_b=0.53 nm to eq. (5.16) yields E_{tube} = 11.2 eV/nm. The attractive van der Waals energy between the two sheets is E_v = -14.4 eV/nm from

$$E_v = -A / d^2 \cdot S / 12\pi, \tag{5.17}$$

where A = 6×10^{-19} J is the Hamaker constant of CNTs [97], S stands for the area of the two sheets faced, and d = 0.34 nm denotes the graphite inter-sheet spacing. These estimations give $E_{bulb} + E_v < E_{tube}$, which indicates that the flattened state is more stable than the tubular state. For this reason, the large diameter CNT is in the flattened state.

Most flattened CNTs are twisted even if one end is free or unsupported, as presented in Fig. 5.3(e). Therefore, the twist is known not to result from some applied external force. The twist is expected to result from a specific graphitic stacking order on the CNT inside face. The most probable mode of stacking is the AB stacking from the viewpoint of energetic stability. For chiral CNTs, the torsional strain appears and then generates the twist by taking the AB stacking when they are in the flattened state.

This work confirmed the respective stacking orders for armchair, zigzag, and chiral CNTs through MD simulations. Figures 5.4(a)–5.4(d) portray stable states of 3-nm-long CNTs with (40, 40), (45, 35), (68, 2), and (69, 0) at 5 K after flattening. The armchair CNT (40, 40) adopts the AB stacking presented in Figs. 5.4(a) and 5.4(e) and shows a straight flattened shape without twisting, as presented in the left image of Fig. 5.4(a). The chiral CNT (45, 35), being near the armchair line, also adopts the AB stacking. In this case, however, the twist was caused to take AB stacking, as shown in the left image of Fig. 5.4(b). In contrast, the zigzag CNT (69, 0) were not able to adopt the AB stacking, but instead adopted AB-like stacking with a straight flattened shape, as portrayed in Figs. 5.4(d) and 5.4(f). The chiral CNT (68, 2), being near the zigzag line, also responds better to AB-like stacking with a small twist, as shown in the left image of Fig. 5.4(c). It is noteworthy that the mean potential energy of the -7.21 eV/atom for the

(69, 0) zigzag CNT is comparable to the value of -7.19 eV/atom for the (40, 40) armchair CNT. This result demonstrates that the stability of the AB-like stacking is comparable to that of the AB stacking. Therefore, considering that the initial twist angle depends on the chirality and length of a CNT, one can design the maximum torsional angle of the devices (as described in section 5.8).

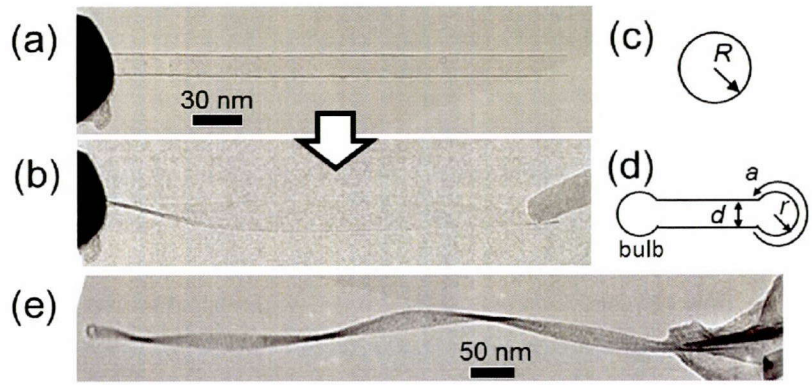

Fig. 5.3 TEM images and illustrations of a tubular state CNT and flattened state CNTs. (a) Multiwall CNT that maintains a tubular state soon after extraction of several inner layers. (b) Same CNT in a flattened state after being kept for several hours in vacuum at room temperature. (c),(d) Cross sections of (a) and (b). (e) Another flattened CNT that is twisted (one end is free).

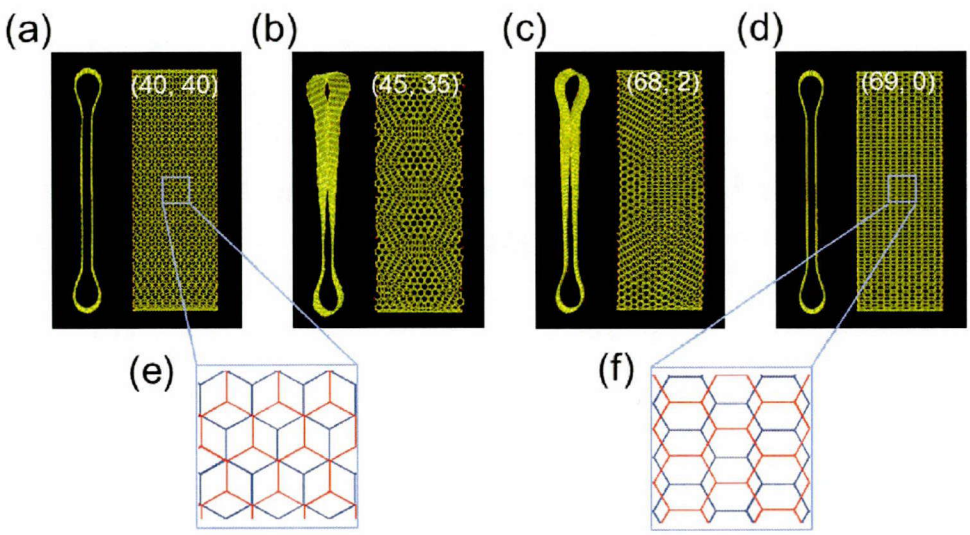

Fig. 5.4 Simulation results of flattened state CNTs. (a)–(d) Simulation results of flattened CNTs with 3 nm length and chiral indices (m, n) = (40, 40), (45, 35), (68, 2), and (69, 0). The left images are views from their tube axis. The right images are views normal to the flattened face. (e) AB stacking, which is preferred in armchair CNTs. (f) AB-like stacking, which is preferred in zigzag CNTs.

5.5 Transition between a flattened and tubular state

Figure 5.5 presents results demonstrating repeated transitions between the flattened state and the tubular state. A flattened and twisted CNT prepared using the process described above is bridged between the two manipulation stages in the TEM. Figure 5.5(a) exhibits the initial state, fully flattened and twisted, for a CNT. When the current was applied to the CNT and increased to 50 μA, part of the flattened CNT changed its state to the tubular state, as presented in Fig. 5.5(b). Yellow arrows in that figure indicate a boundary between the flattened state region and the tubular state region. After the transition from Fig. 5.5(a)–5.5(b), the boundary moved left or right depending on the current amount. When the current decreased, the boundary moved left to expand the flattened region, as shown from Fig. 5.5(b)–5.5(c). In contrast, when the current increased again, the boundary moved right to expand the tubular region, as shown in Figs. 5.5(c)–5.5(d). When the current was reduced to less than 20 μA, it reverted to the initial state (fully flattened and twisted), as presented in Fig. 5.5(e). This result demonstrates that the process is both reversible and current-controllable.

The initial twist in the flattened state causes a torque when the state becomes tubular one. Shifting of the yellow arrow to the right in Fig. 5.5 reflects the generation of torque, which is balanced with the torsional stress because both ends of the CNT are fixed.

Application of the current causes a transition from the flattened state to the tubular one, which suggests that the driving force for the transition is the thermal energy from Joule heating. When the current increases, the local temperature of the CNT becomes greater than a critical value. Then the attractive van der Waals energy at the CNT inside is compensated by the total energy of the curvature energy stored at the bulbs and the thermal energy. The thermal energy affects the attractive van der Waals energy and the curvature energy. We examine the deviation in the total energy of the flattened state caused by the thermal energy ΔEt. For CNTs with the initial flattened state, as presented in Fig. 5.5, the curvature energy per unit length is estimated as $E_{bulb} = 11.2$ eV/nm from eq. (5.16). The attractive van der Waals energy between the two sheets is $E_v = -8.0$ eV/nm, as calculated from eq. (5.17). After the first transition to the tubular state, the surface energy at the tubular state per unit length is $E_{tube} = 1.1$ eV/nm from eq. (5.15). The inequality $E_{tube} < E_{bulb} + E_v + \Delta E_t$ is a precondition for taking the tubular state. It provides deviation for the first transition of $\Delta E_t = 2.1$ eV/nm.

In addition, the circumferential current density $J = I / \pi d$ when the first transition was 1.2–2.0 μA/nm. These values are less than 2.2 μA/nm, at which the CNT begins to sublimate [88]. This result shows that the transition occurred at a temperature that is

lower than the sublimation temperature of 2500 K for CNTs [88].

To investigate the effect of the thermal energy to the transition, MD simulations were performed with 30-nm-long (40, 40) CNT. Figures 5.6(a)–5.6(d) show movement of the boundary between the tubular state and the flattened state depending on the temperature obtained using the MD simulation. In the calculation, atoms at the left end were fixed to maintain the tubular state, whereas 640 atoms from the right end were fixed to maintain the flattened state. Figure 5.6(a) exhibits the stable state of the CNT at room temperature under the conditions described above. Figures 5.6(b)–5.6(d) show the state after being kept for 1 ns at each temperature. The boundary position indicated by the yellow arrow moves right depending on the temperature. This temperature dependence of the boundary movement shows good agreement with the experimentally obtained results.

It is reasonable to consider that the thermal energy plays a role in producing a space between the two faced sheets to open the flattened CNT. At the lower temperature, for example 300 K, atoms at the boundary between tubular and flattened states are almost static, as presented in Fig. 5.6(e). However, when the temperature increases, for example 1200 K, those atoms fluctuate actively as presented in Fig. 5.6(f). Under this condition, the distance between two sheets lengthens at the boundary between tubular and flattened. Then the opened area is spread with the assistance of the curvature energy stored in the bulbs. Consequently, the flattened state changes to the tubular state.

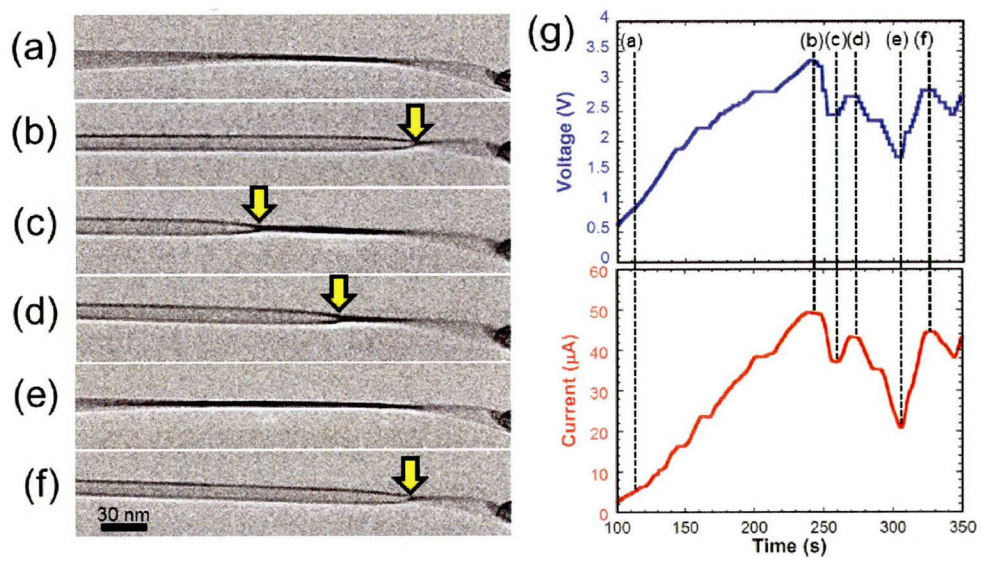

Fig. 5.5 TEM images of reversible transitions between the tubular state and the flattened state in a CNT by application of current and temporal variations of applied voltage and corresponding current. Left (a–f) Sequential TEM images of an multiwall CNT during processing. (g) Temporal variation of the current corresponding to that of the voltage applied to the CNT. Right, points designated a–f

correspond to TEM images (a)–(f). (a) Fully flattened CNT was bridged between the electrodes and current of 5 μA was applied. (b) The CNT changed its state to a partially tubular state at 50 μA. The yellow arrow in the left panel indicates the boundary between the left tubular state region and the right flattened state region. (c) Boundary shifted left at 36 μA. (d) Boundary shifted right again at 42 μA. (e) The CNT state returned to the initial one at less than 20 μA. (f) Fully flattened CNT changed its state to the partially tubular state again at 42 μA.

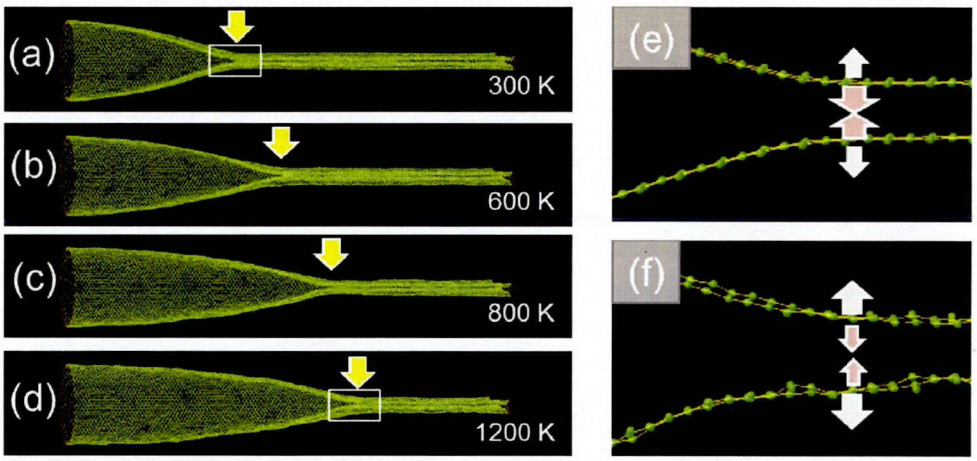

Fig. 5.6 Simulation results of the transitions between the tubular state and the flattened state in a 30-nm-long (40, 40) CNT. (a)–(d) After being kept at a target temperature (300 K, 600 K, 800 K, 1200 K) for 1 ns. The yellow arrow indicates the boundary between the left tubular state region and the right flattened state region. The boundary position shifts depending on the temperature. (e), (f) Enlarged cross section images for white squares in (a) and (d), respectively.

5.6 State transition showing the change of conductance

The state transition in a CNT causes a conductivity change of the CNT. Figure 5.7 portrays another example of the transition behavior from the flattened state to the tubular state by application of current to a CNT. A current of ca. 110 μA is applied to it. Constriction in the middle of the CNT that is visible in Fig. 5.7(b) shows that this CNT is flattened and twisted. Figure 5.7(c) shows that increasing the current to 111 μA and maintaining it for several tens of seconds suddenly changed a part of the CNT from the flattened state to the tubular state. This transition time is less than the frame rate (0.2 s) of a CCD camera installed in TEM. After the transition, the CNT to the left of the yellow arrow indicates the tubular state; the right side shows the flattened state.

The CNT conductance changes dramatically when the transition occurs. Figure 5.7(a)

depicts temporal variations of the applied voltage and the resultant current during the process. At $t < 234$ s, the CNT exhibits the flattened state presented in Fig. 5.7(a). The current does not change even though the voltage increases slightly. However, the current decreases abruptly at around $t = 237$s, where the voltage does not change, when part of the CNT changed to show a tubular state. The result shows that the flattened state region has higher conductivity because of its two-dimensional dispersion relation of bilayer graphene [99].

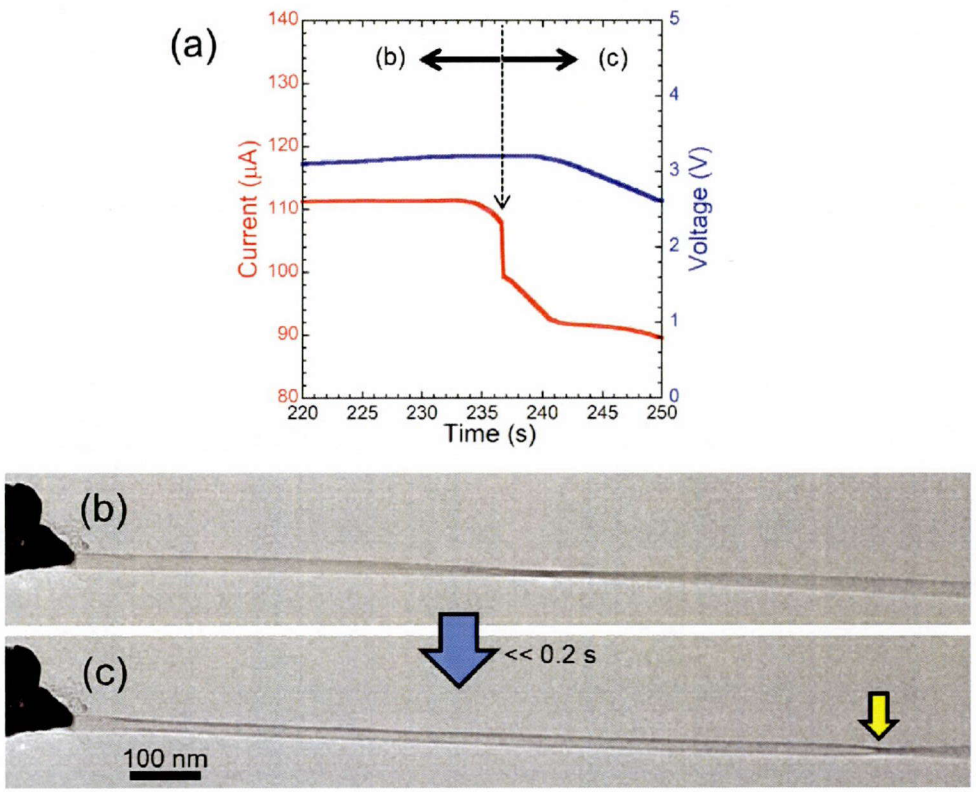

Fig. 5.7 Transition from the flattened state to the tubular state in a CNT by application of current. (a) Temporal variations of the voltage and corresponding current applied to the CNT; notations (b) and (c) respectively correspond to TEM images of (b) and (c). (b) TEM image of a flattened and twisted CNT bridging the Si probe tip and CNT cartridge. (c) CNT after transition to a tubular state. A yellow arrow indicates the boundary between a tubular state and a flattened state. The transition occurs within 0.2 s.

5.7 Hysteresis in transition

The response of the transition is also an important factor for the realization of the device using the phenomenon. In the experimental condition, the transition is dominated

by the amount of thermal energy, which is controlled by the current flow. However, a relation between the given energy and the length of transition area presents a certain difference between the opening process induced by increasing the current and the closing process induced by decreasing the current.

Figure 5.8(a) presents a series of snapshots for a state transition of a CNT. The diameters of the outermost and innermost nanotube are, respectively, 14.5 nm and 8.3 nm. This nanotube has nine layers. The flattened region up to 200 nm length changed to a tubular state with around 40 μA and 2 V, as shown in the bottom TEM image of Fig. 5.8(a). The current increasing process corresponds to the opening process, as indicated by the red arrow in Fig. 5.8(a). In contrast, the current decreasing process corresponds to the closing process as indicated by the blue arrow in Fig. 5.8(a). In this experiment, the current increasing and decreasing process was repeated continuously three times. Figure 5.8(b) presents the temporal variation of the current corresponding to that of the voltage applied to the CNT for those three trials. The first two trials take 200–300 s per trial and the last trial takes 600 s.

Figures 5.8(c)–5.8(e) show the relations between the current density and the flattened state area corresponding to each trial. It is clear that hysteresis exists in all trials by comparing the boundary positions in the current increasing and decreasing process at the same current density in Figs. 5.8(c)–5.8(e).

The hysteresis is explained by the asymmetric potential energy in the state transition, as presented in Fig. 5.9. The potential energy of the flattened state is smaller than that of the tubular state in a thick CNT in which the flattened state is energetically stable at room temperature. For example, the potential energy of a 30 nm-long (40, 40) CNT at the tubular and the flattened states calculated from MD simulation are, respectively, -7.18 eV/atom and -7.19 eV/atom. When the state transition occurs, the system must exceed a certain potential barrier. In the transition from the tubular to the flattened state in the CNT, the potential energy increases gradually as the CNT deforms, as shown in Figs. 5.9(b)–5.9(c). However, once the CNT has negative curvatures in its configuration, as presented in Fig. 5.9(d), the CNT becomes a flattened state easily supported by van der Waals energy. In the process, the potential energy decreases sharply and shows an asymmetric distribution as presented in Fig. 5.9(a). Therefore, in the transition from the flattened to the tubular state, the CNT needs higher energy to overcome the higher slope. Consequently, sufficient energy for the transition from the tubular to the flattened state *i.e.* the circumferential current density indicated by red line in Figs. 5.8(c)–5.8(e) took a higher value than that for the transition from a tubular to a flattened state indicated by blue line in Figs. 5.8(c)–5.8(e). This is the most probable origin of the hysteresis.

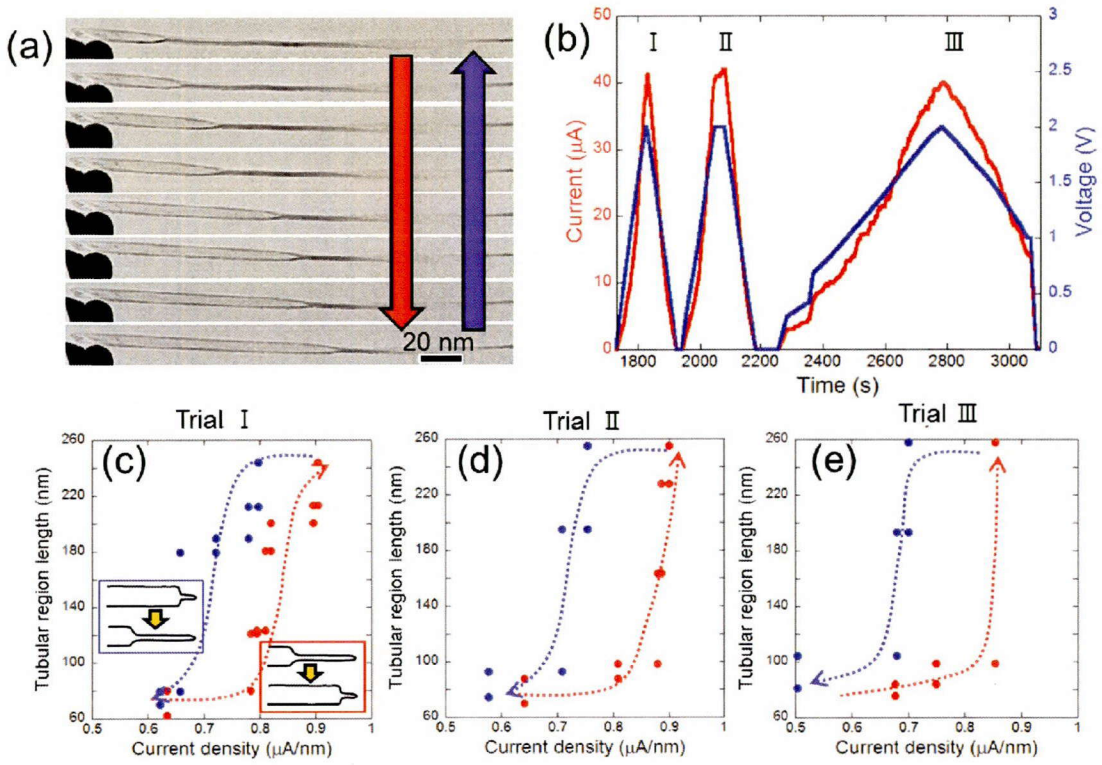

Fig. 5.8 Hysteresis in the state transition. (a) Series of TEM images for the state transition. (b) Temporal variation of the current corresponding to the voltage applied to the CNT portrayed in (a). The current increasing and decreasing process was repeated three times. The respective processes trials are denoted as I, II, and III. (c)–(e) Relations between current density and tubular length corresponding to those in respective trials.

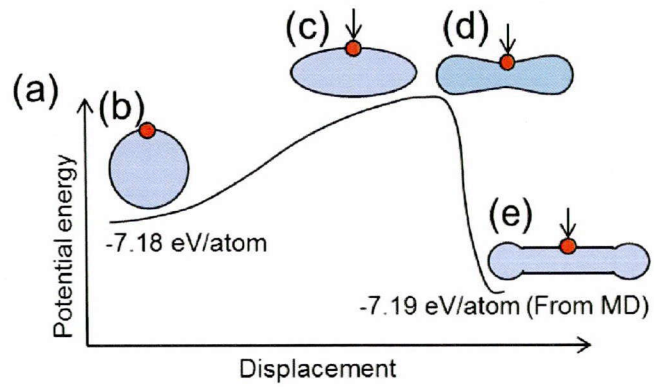

Fig. 5.9 Model of potential energy in the state transition. (a) Potential energy of a CNT corresponding to the displacement of an atom of the CNT indicated by red points in schematics (b)–(e), which show the cross section of the CNT in the transition between (b) the tubular state and (e) the flattened state.

5.8 Torsional actuator

5.8.1 Torsional angle and torque of the actuator

The reversible transition with torsion is a unique behavior that is applicable to nanosized actuators as described in chapter 3. Our proposed actuator is portrayed in Fig. 3.8. In the actuator, two electrodes support a flattened and twisted CNT at both ends. One end is fixed to the electrode by an attachment process [70]. The other end, which is connected to the electrode with a CNT bearing [5] structure, is free to rotate. When the CNTs change their states according to the current control, the free end rotates clockwise or counterclockwise.

It is possible to design the maximum torsional angle of the devices because the initial twist angle depends on the chirality and the CNT length as described in section 5.4. We examine the initial twist angle per unit length. The twist of the flattened CNT results from taking specific graphitic stacking orders for the CNT inside. Regarding armchair CNTs, they show the AB stacking presented in Fig. 5.10(d). They assume a straight flattened shape without twisting. Chiral CNTs near the armchair line also mainly show the AB stacking. For the AB stacking, the axis of the flattened CNTs is along the zigzag line, as portrayed in Fig. 5.10(c), which causes the twist because the zigzag line is not parallel to the tubular axis. In this case, a simple geometrical analysis shows that the torsional angle per unit length is given as $\beta = 2 \cdot \tan(\pi/6 - \alpha)/D$, where D and α respectively represent the diameter and the chiral angle of the CNTs. In contrast, zigzag and near zigzag CNTs cannot assume the AB stacking conformation, instead showing AB-like stacking, as portrayed in Fig. 5.10(b). The axis of the flattened CNTs is along the armchair line, as portrayed in Fig. 5.10(a). In this case, the torsional angle per unit length is given as $\beta = 2 \cdot \tan\alpha/D$. Figure 5.10(e) presents the relation between the chiral angle and the torsional angle at unit length for three diameters. For example, it is possible to design a torsional actuator with maximum rotation of 180° by choosing a 38-nm-long (49, 23) CNT, which is shown as a closed circle in Fig. 5.10(e).

We confirmed the torsional motion with MD simulations. Figure 5.11(a) presents a series of snapshots for the reversible transition of (42, 38) CNT in which the top end is fixed as the flattened state and the bottom end is free to rotate with the tubular state. Figure 5.11(b) shows temporal variation of the rotational angle of the bottom end of the model (red line) and the target temperature in the simulation (blue broken line). The maximum rotational angle reaches 4° with ca. 10 nm of transition length at 1200 K. When the temperature returns to the initial temperature (300 K), the rotational angle also reverts to zero. This obtained torsional angle is reasonable from the twisting angle

of 0.5°/nm for (42, 38) referred from Fig. 5.10.

The torque generated when the transition occurs is estimated using simple continuum models. The shape of a cross section of a flattened CNT is approximated as a rectangle: $a \times b$ $(a < b)$. The torque is given as $\tau = GI_p\theta$, where G (=1 GPa) [100] is the shear modulus of the CNT, $I_p = 1/3ab^3$ denotes the polar moment of inertia of the area, and θ is the specific angle of the twist. For the (49, 23) CNT marked in Fig. 5.10(e), the torque is estimated as $\tau = 5$ nNnm, which is 50 times stronger than that of rotational biomolecular motors (ca. 100 pNnm) [57].

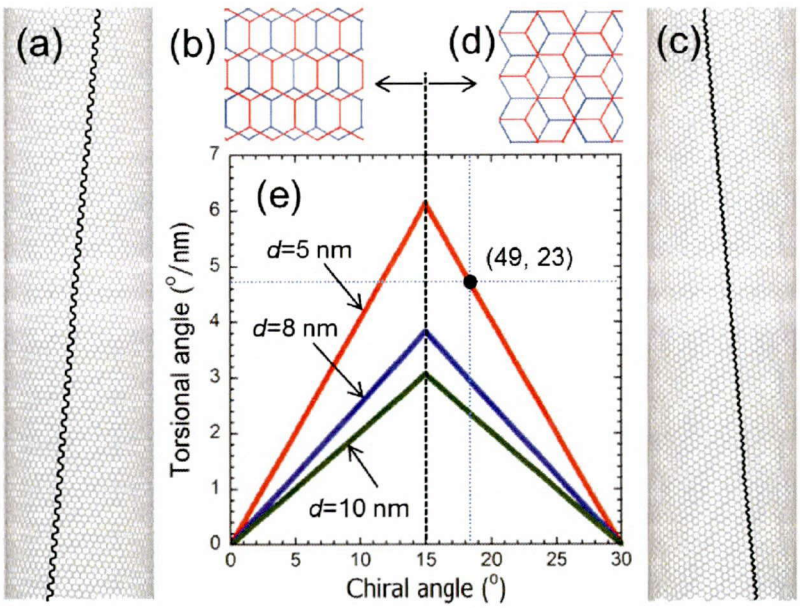

Fig. 5.10. Specific graphitic stacking orders and the relation between the chiral angle of CNTs and the torsional angle per unit length. (a) (60, 6) CNT which takes AB-like stacking. The bold line shows the armchair line along which the CNT is flattened to accommodate AB-like stacking. (b) AB-like stacking is preferred in CNTs with a chiral angle of less than 15°. (c) (42, 31) CNT showing AB stacking. The bold line represents the zigzag line along which the CNT is flattened to accommodate the AB stacking. (d) AB stacking is preferred in CNTs with a chiral angle of 15°–30°. (e) Torsional angle calculated from the geometrical analysis, shown as a function of the chiral angle.

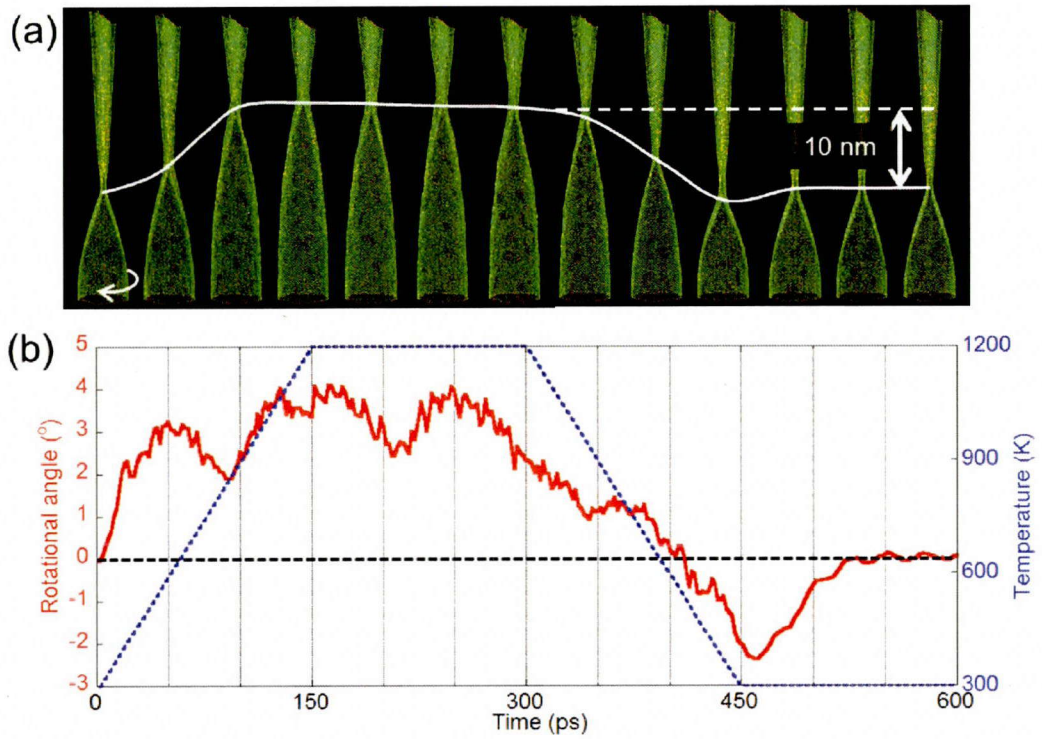

Fig. 5.11 (a) Sequential snapshots for rotational motion of a 30-nm-length (42, 38) CNT corresponding to the state transition obtained using the MD simulation. The top end is fixed to maintain the flattened state. The bottom end is free to rotate, maintaining the tubular state. (b) Temporal variation of the rotational angle of the CNT model and the target temperature in the calculation.

5.8.2 Response speed of the actuator

The actuator response speed depends on the transition speed. The MD simulation shows that the velocity for the shift of the boundary between the flattened and the tubular state reaches 500 m/s. The speed provides 10 GHz of repeatable clockwise and counterclockwise rotations in the device consisting of 50 nm transition length.

However, because the transition results from the thermal energy, we must address the heat transfer efficiency of the device. Analysis of the heat transfer of a CNT is a tough and challenging problem. Computational studies are necessary to analyze the heat transfer behavior of CNTs. Using MD simulation, non-Fourier heat conduction has been investigated in single-wall CNTs subjected to a local heat pulse with time duration of subpicoseconds [101]. In this report, the temperature distribution of a locally heated CNT (25 nm length) by the heat pulse goes back to the static state within a few picoseconds. This heat transfer efficiency in a CNT is capable of designing the torsional actuator working with terahertz order. Therefore can be ignored considering the

maximum reaction speed. Parts where the thermal resistance can be highest are the boundaries between the electrodes and the CNT. The heat transfer between a CNT and a metal is another challenging subject. For the interface between bulk copper and a single-wall CNT, the value of 4 $GWm^{-2}K^{-1}$ as the interfacial thermal conductivity has been reported based on MD simulations [102]. Using this value, the time constant of heat dissipation from a CNT to the metal is calculated as 10 ps. This value also supports a designable nanotorsional actuator working with 10 GHz.

5.9 Summary

Using TEM manipulation and MD simulations, we demonstrated the transition between the flattened and the tubular states in CNT. The MD simulations clarified that the twist of the flattened CNT results from taking specific graphitic stacking orders for the CNT inside. It was also clarified that the driving force for the transition is the thermal energy. The boundary between the tubular state region and the flattened state region changes its position depending on the temperature. These results present the possibility of design and control of the output torsional angle and torque of the actuator by selecting the chiralities and lengths of CNTs and by controlling the current.

The actuator that we have proposed has broad potential for application to the driving of miniaturized devices. For example, it is available for use as a switch and an oscillator using alternating current. Moreover, it might be useful as a screwdriver or gear. A thinner CNT that is joined at the end of the actuator by joining [98] or elongation [53] processing can function as a gripper for nanosized robot arms. We believe that this nanoactuator will open a new field of functional nanomachines.

Chapter 6

Biosensor for single-molecule measurements

6.1 Introduction

Nanobiotechnology is an important field in nanotechnology emerging at the intersection of materials research, nanosciences, and molecular biotechnology. The discussion in this chapter is focused particularly on single-molecule measurement, which currently attracts much attention and which is expected to provide a powerful means for the fundamental investigation of life sciences.

The design and structures of biological molecules have been well established through numerous studies of biomolecules and deoxyribonucleic acid (DNA) including our genetic information. However, the information is insufficient to elucidate the mysteries of life. It is important to consider that living systems comprise their dynamic motions of such systems in addition to their static structures. Therefore, some understanding of these behaviors at a molecular level will lead us to the elucidation of biological phenomena.

For this challenge, biological molecular dynamics measurement at the single-molecule level using CNTs has been proposed and studied for project research (JST CREST). This project is intended for development of a device to measure the interactive force and mass of biomolecules in real time to elucidate the dynamics of protein molecules at the single-molecule level using CNTs. The concepts of those devices are described in section 3.5.3.

To realize those measurements with accuracy, a CNT tip, which is a portion for trapping a single-protein molecule in the devices, should be designed suitably and fabricated considering measurement situations. In this project, I specifically examined the development of CNT arms as components of nanosensors for single-molecule measurements. This chapter describes a fundamental technique for creation of CNT arms including the attachment process of a CNT to the substrate (section 6.3) and fabrication processes of the CNT arms for force measurement (section 6.4.1) and mass measurement (section 6.4.2). In addition, results of the actual force measurement using the CNT arms are introduced in section 6.5.

6.2 Experimental method

The idea for the attachment of CNTs used in this work is that C_{60} molecules inserted between the CNTs and substrate serve as glue. The C_{60} molecules were deposited on commercially available probes for use with scanning probe microscope (SPM) or Si substrates covered by Pt thin film by heating at 673 K in vacuum, which is an almost identical method to that used for the encapsulation of C_{60} molecules in a CNT described in section 4.3.1. The deposition thickness was controlled to a few molecular layers by adjusting the sublimation time of C_{60} molecules. The C_{60}-deposited probe and the CNT cartridge in which CNTs were aligned at the sharpened edge of the Si substrate were set respectively on piezoelectric-driven manipulator stages installed in the TEM. A free end of a CNT protruding from the cartridge was manipulated to touch the probe tip. An electron beam was irradiated to the C_{60} molecular layer that was contacted with the CNT to attach it.

The CNT arms were fabricated using a TEM equipped with a manipulator as described for the experiments in chapters 4 and 5. CNTs used in this work were multiwall CNTs produced using the arc-discharge method. The CNT diameter is in a range of 10–20 nm. For the measurement of biological intermolecular interaction force, commercially available Cr/Au coated Si probes with a spring constant of 0.03 N/m (CSC38/Cr-Au; MicroMasch) were used as the base of the CNT probes. In addition, Importin α and importin β [103] were used as a model for examining protein–protein interaction. Detail conditions and setups for the force measurements are described in section 6.5 and Appendix 3.

6.3 Attachment of carbon nanotubes

Components of CNTs in the devices must be attached to substrates sufficiently. Conventional methods to attach CNTs use thin film deposition. Electron-beam-induced deposition of thin films is applied for construction of CNT devices in an SEM equipped with a manipulator [17,104]. The sources of film deposition are contamination in SEM for carbon films [17,104] and metalorganic gases for metal films [105]. It is nevertheless difficult in TEM to adopt that method for film deposition used in SEM because of a higher vacuum condition. We developed an alternative method to attach CNTs to the substrate in TEM. As described herein, it is a new approach by which the graphitic structure created by an electron-beam-induced structural change of C_{60}

molecules is used to attach CNTs on the substrate [70].

Figure 6.1(a) shows that a CNT was placed at the edge of the silicon substrate which was coated with the C_{60}-molecular layers. Then, the converged electron beam was irradiated near the CNT. The C_{60} molecules gathered continuously to a central part of the irradiation area and covered a part of the CNT when the electron dose was as high as 3×10^8 electrons/nm^2. The phenomenon of migration of C_{60} molecules toward the irradiated area plays an important role in attaching the CNT mechanically on a substrate. The most possible driving force of the migration of C_{60} molecules is the Coulomb repulsion working in C_{60} molecules, which results from the negative charges induced to C_{60} molecules from the electron beam.

The electron beam irradiation also changed the structure of the gathered C_{60} molecules to form a graphitic structure. Figure 6.2 presents a multiwall CNT on the Pt/Si substrate covered with C_{60} molecules before and after electron-beam irradiation. The almost three-molecule layer of C_{60} molecules was deposited on the Pt/Si substrate, as depicted in Fig. 6.2(a). An electron beam with a dose of 3×10^8 electrons/nm^2 was irradiated to the CNT and the C_{60}-molecular layer near the CNT. Graphitic layers were constructed to cover not only the substrate, but also the CNT. This structural change functioned effectively to attach the CNT to the substrate both mechanically and electrically.

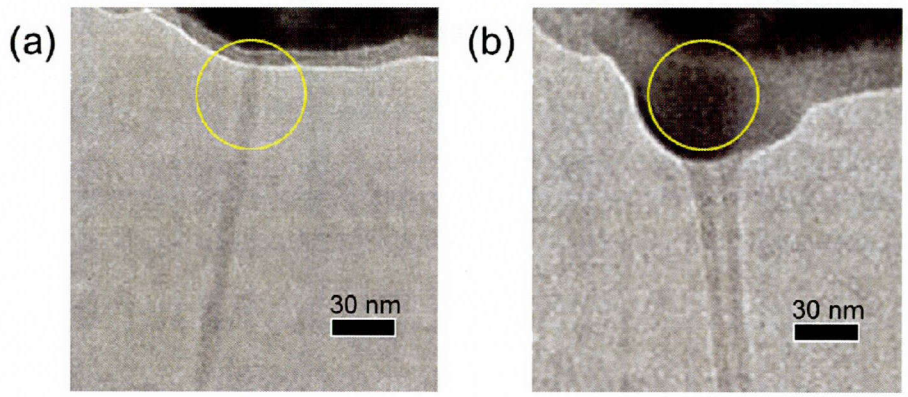

Fig. 6.1 TEM images of a CNT putted on the tip of a probe for SPM covered with C_{60} molecules (a) before and (b) after electron beam irradiation with 3×10^8 electrons/nm^2.

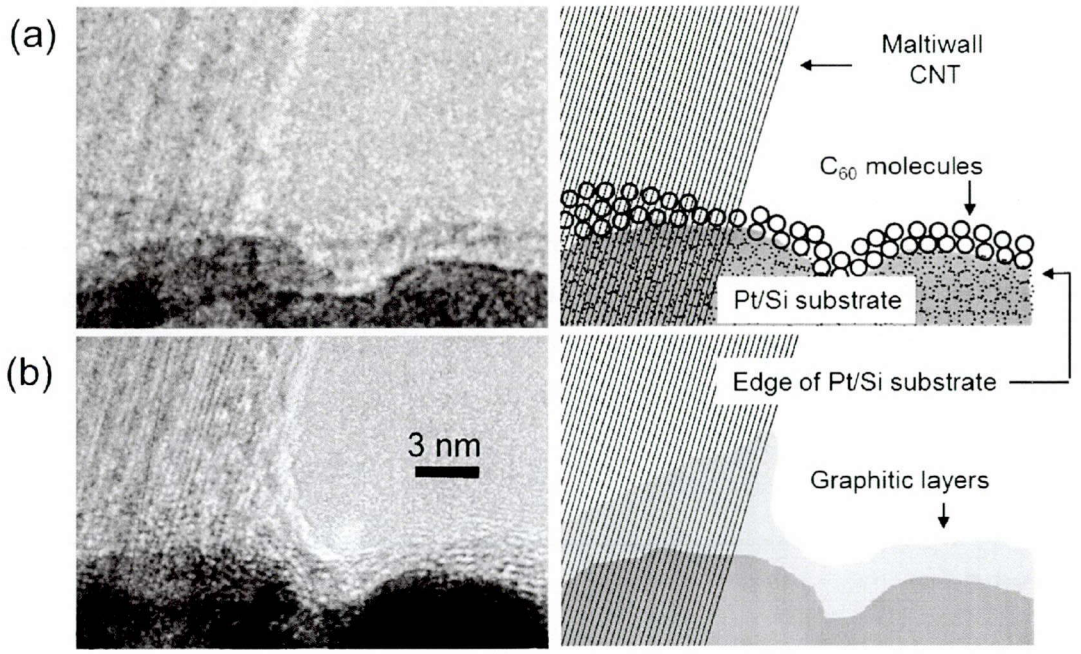

Fig. 6.2 TEM images and schematics of interface between a multiwall CNT and a Pt/Si substrate covered with C_{60} molecules (a) before and (b) after electron beam irradiation with 3×10^8 electrons/nm^2.

6.4 Fabrication of carbon nanotube arms

6.4.1 Fabrication of sharpening tips for force measurement

The force measurement system is embedded in AFM as described in section 3.5.3. In the force measurement, the CNT stiffness is important to avoid undesired CNT bending or vibration. However, the use of thicker CNT probes makes it impossible to measure biological reactions at a single-molecule level. Subsequently, we fabricated conical CNTs with a sharpened end by cutting multiwall CNT by application of excess current.

Figure 6.3(a) presents an initial condition of a multiwall CNT bridged between an AFM tip (left side) and cartridge (right side). The CNT is put along an edge line of the AFM tip. The resultant CNT length protruded from the AFM tip after cutting is controlled by arranging the suspended length between electrodes. Joule heating of a CNT in this condition provides a parabolic temperature distribution in a suspended area [86,88]. Consequently, CNTs are usually cut from the center of a suspended area where the temperature becomes highest. Therefore, the suspended length is arranged to be twice the objective length before applying the current. When the current reached 200 μA

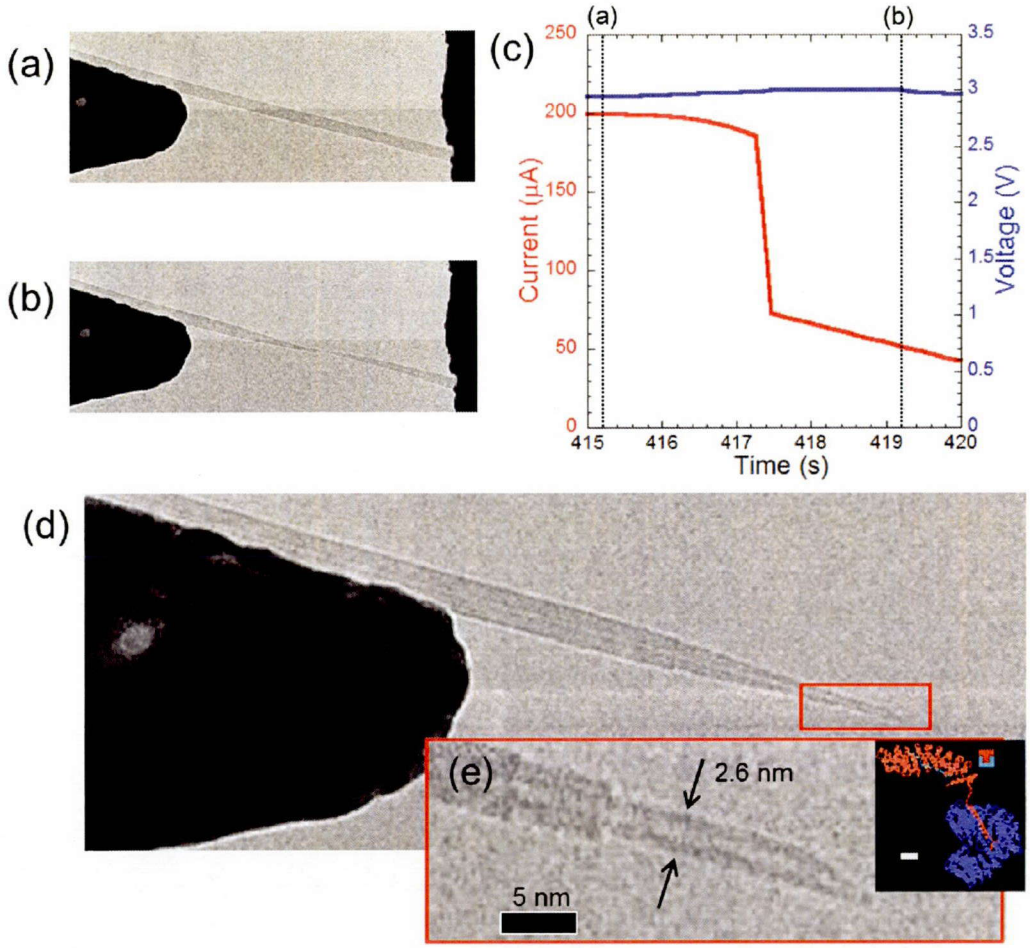

Fig. 6.3 Fabrication process for sharpening tips. TEM images of a multiwall CNT bridged between electrodes (a) before and (b) after structural change induced by the application of the current. (b) Outer layers of the CNT sublimated from the center of the suspended area. (c) Temporal variation of the current corresponding to that of the voltage applied to the CNT. Points on the graph designated as (a) and (b) correspond to TEM images (a) and (b). (d) TEM image of the CNT tip after cutting. (e) Enlarged image of the tip shown as a red square in (d). The inset in (e) is a model of a pair of proteins named importin α and importin β. Their scale is fitted to the TEM image.

outer layers of the middle area. The number of layers decreased stepwise to the center region. Consequently, the center region diameter became 2.6 nm, as depicted in Fig. 6.3(b). During the structural change, although the current shown as a red line in Fig. 6.3(c) decreased from 200 μA to 50 μA, the circumference current density was almost constant: 6.1 μA/nm to 6.4 μA/nm. This result means that the electrical resistance increases as the diameter decreases, whereas the temperature of the CNT is almost constant. That result shows good agreement with results described in a previous report measuring the temperature of a CNT from light emissions during Joule heating [88].

Finally, the right-side CNT was pulled slowly to cut with the current maintaining 50 μA. Consequently, the sharpened tip as depicted in Figs. 6.3(d) and 6.3(e) was obtained. The inset in Fig. 6.3(e) shows models of protein molecules named importin α (red) and importin β (blue). The size of those models is fitted to the scale of TEM image of Fig. 6.3(e). Consequently, the image clarifies that the sharpened tip is suitable for trapping only a single protein molecule.

6.4.2 Formation of a thin carbon nanotube on a multiwall carbon nanotube for mass measurement

CNT arms for mass measurement must meet stricter requirements rather than those used for force measurements. The mass measurement system is based on the CNT-FET device. Figure 3.9(b) shows that the system consists of a CNT arm which is attached at an AFM tip and a CNT transistor. The resonance frequency of the CNT arm is changed when a protein is trapped at the CNT arm tip. The protein mass is calculated by detecting a slight change of the frequency of the CNT arm by the CNT transistor. Therefore, the CNT arm needs a sufficiently stiff body to generate suitable signals in a liquid aside from a thin tip for trapping a single molecule. Moreover, sharpened CNT tips, as described in section 6.4.1 are difficult to adopt in the system not only because their mechanical vibration mode is complex for analyses, but also because of the many ends of layers in its stepwise structure can be a cause of excess trapping of molecules. Therefore, we demonstrated a fabrication process to join a thin and short CNT, which provides a trapping portion for a single molecule on its tip and a multiwall CNT using TEM manipulation.

Figure 6.4 presents sequential TEM images of that process and temporal variation of the current and voltage in the process. First, two CNTs are faced in contact, as depicted in Fig. 6.4(a). The right side CNT is a multiwall CNT with an open end. The left side CNT is a hollow CNT from which inner layers are extracted using the process described in section 5.3. Figure 6.4(i) presents a temporal variation of the current corresponding to that of the voltage applied to the CNT. Points on the graph designated (a)–(h) correspond to TEM images Figs. 6.4(a)–6.4(h). When the current reaches 87 μA, the outer layer of the left side CNT starts to sublimate from the interface between two faced CNTs where the temperature is highest as depicted in Fig. 6.4(b). The reason why only the left side hollow CNT sublimates is discussed later in this section. As sublimation proceeds, the tube configuration of the left side CNT begins to break as depicted in Fig. 6.4(c) and graphitic flakes are formed on the tip of the right side CNT as depicted in Fig. 6.4(d). In this structural change, the current decreases rapidly, as

indicated by points from (c)–(d) in Fig. 6.4(i) because of ruptures of atomic bonds. However, simultaneously, the thermal energy provides covalent bonds between two CNTs at the interface as well as sublimation and improves conductivity at the interface. Then, the region of maximum temperature shifts to the left point indicated by a yellow arrow in Fig. 6.4(e) where the sublimation occurs most frequently. In the structural change from Fig. 6.4(e)–6.4(g), the graphitic flakes start to form a tube configuration with a gradual current decrease as indicated by points from (e)–(g) in Fig. 6.4(i) because dangling bonds at the edge of the graphitic flake produce covalent bonds with neighbors induced by a certain temperature that is slightly lower than the sublimation temperature [106]. Finally, a double-wall CNT is fabricated on the tip of the right-side multiwall CNT, as depicted in Fig. 6.4(h). That thinner part is 9.3 nm long with 2.3 nm diameter.

In this process, the hollow CNT serves an important function to provide a carbon source for fabricating a thin CNT through its breakdown and reconstruction. In our experiments, the interface between the two CNT tips has higher electric resistance than those of the bodies of the CNTs at the initial state. At this time, the current flows across several layers through the interface. Consequently, the interface temperature becomes highest across several layers by Joule heating. However, the thermal capacities are slightly different between the two-faced CNTs corresponding to the difference of number of layers. Consequently, only the left hollow CNT starts to sublimate first. Generally, it has been thought that the number of layers does not strongly affect the thermal capacity because the thermal conductivity between layers in graphite (6 W/mK at room temperature [9]) is much lower than that for planar direction in graphene (3000 W/mK at room temperature [9]). Therefore it is almost negligible. However, in this case, it is possible that the slight difference in the thermal capacity arises from the difference of the number of layer functions, causing a difference in the timing of their sublimation.

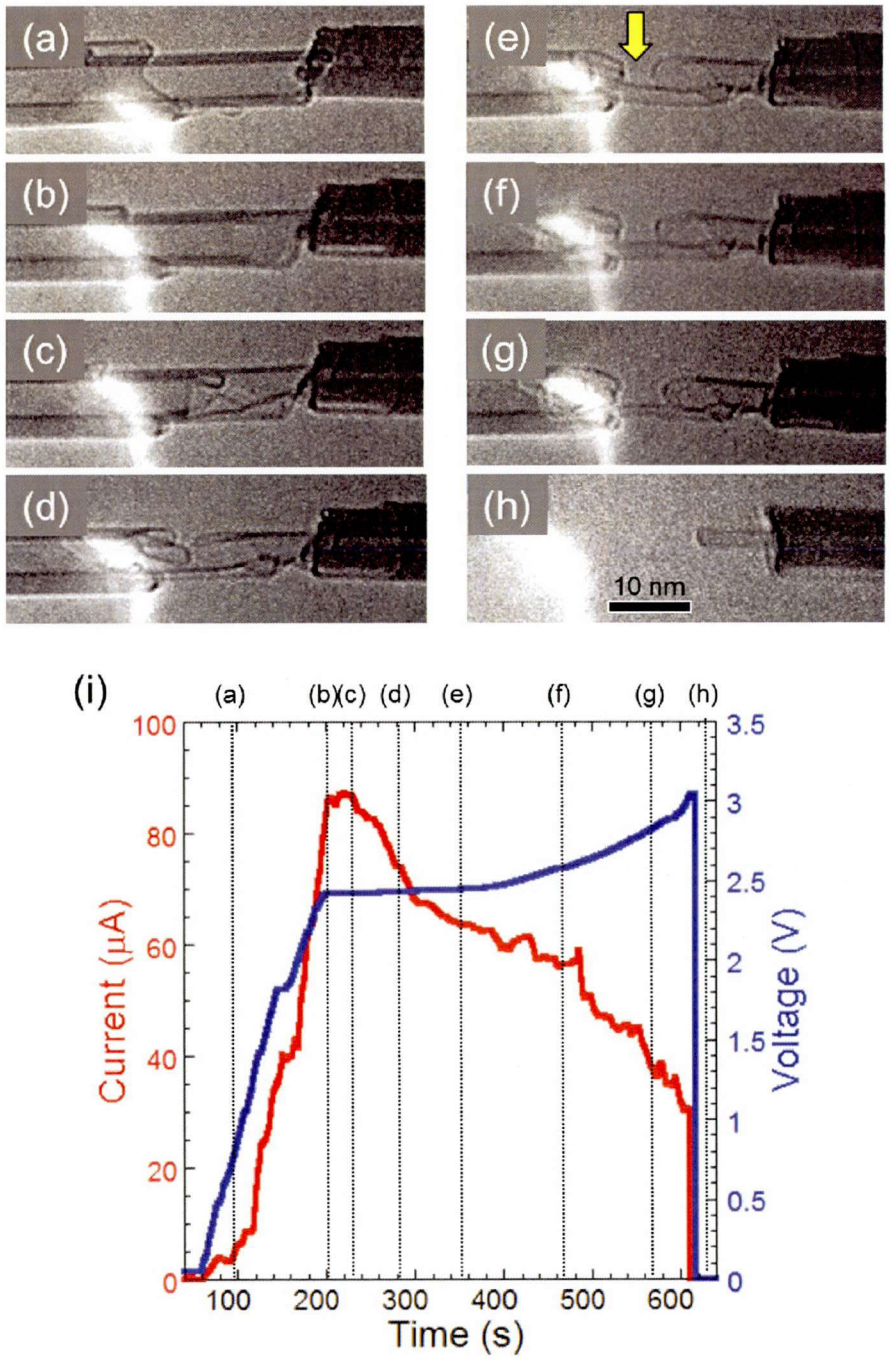

Fig. 6.4 Fabrication process of a thin CNT on the tip of multiwall CNT. (a)–(h) Sequential TEM images for the process. The left CNT is a multiwall CNT from which inner layers were extracted. The right-side CNT is a multiwall CNT with an opened end. (i) Temporal variation of the current corresponding to that of the voltage applied to the CNTs. Points on the graph denoted as (a)–(h) correspond to TEM images (a)–(h).

6.4.3 Opening process

To trap a single protein molecule, the CNT tip should be opened to have carboxyl groups (-COOH) for the latter chemical reaction process. Normally, an open-ended CNT automatically obtains carboxyl groups at the tip in an oxidizing environment with moisture [107]. However, the tips of CNTs after the sharpening process described above tend to close because the closed ends are energetically more stable than the opened ends are. Therefore, we used an electron bombardment process to open the sharpened CNT tip.

First, a constant voltage of 5.45 V was applied between the two-faced sharpened CNTs while maintaining a certain distance between them, as depicted in Fig. 6.5(a). When the distance between the two sharpened tips became less than 10 nm, the cap of the left side CNT disappeared suddenly, as depicted in Fig. 6.5(b). The current flow in this process was less than 100 pA, which resulted from electron emissions corresponding to the voltage and gap distance between the two sharpened CNT tips. At the moment when the left side CNT was opened, the current increased slightly by ca. 1.5 pA, as depicted in Fig. 6.5(c). That current increase represents an increase of the number of emitted electrons by 10^7. Those electrons emitted from the left side CNT tip (anode) go through to the right side CNT (cathode). Generally, a cathode is damaged by electrons emitted in a field emission. However, in this case, the rapid current increase also provides damage to the left CNT, which is an electron emitter. The possible origins of this structural change are tensile stress by static electron force and thermal energy given by the current flow [Emi *et al.*, submitted]. However, the detailed mechanisms for this phenomenon remain unclear and present a challenge for further research.

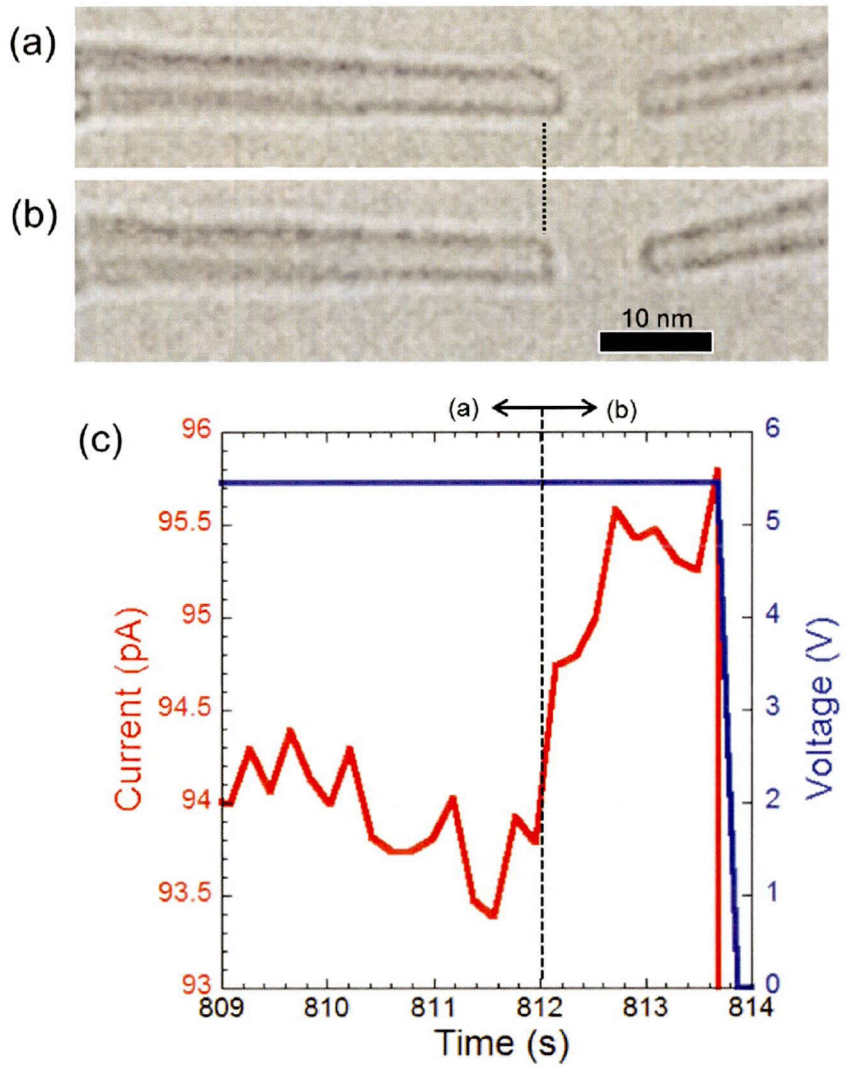

Fig. 6.5 Opening process for CNT tips. (a) TEM images of two sharpened CNT tips faced with a gap distance between two tips maintaining 9 nm. (b) TEM image after removing the left side CNT's cap by an electron bombarded process. (c) Temporal variation of the current corresponding to that of the voltage applied to the CNT. Points on the graph denoted as (a) and (b) correspond to TEM images (a) and (b).

6.5 Force measurements

Next, results of force measurements intended for a single protein molecule using CNT arms, as performed in our project, are described. The force measurement system is embedded in AFM, as described in section 3.5.3. Importin α and importin β [103] were used as a model for examining protein–protein interaction. Importin α binds to importin

β through its importin β binding domain (IBB).

Importin α is bound to the tip of a CNT arm at a specific position [71] using an effective site-specific labeling technique [72] by which an unnatural amino acid, 3-azidotyrosine, is introduced to the targeted site of a protein. Importin β is supported on single-wall CNTs protruding from resin of a so-called CNT sheet. In addition to the CNT arms, the CNT sheet also plays an important role in realizing single-molecule measurement in accuracy. Our group has developed CNT sheets as a substrate to immobilize single importin β molecules with an oriented direction [Nakano *et al.*, submitted].

In force measurements, azido importin α partial recombinants of two types were used: F124Amb and F56Amb. These have different introduction sites of azidotyrosine, to which the CNT arm tip binds. Importin α F124Amb has azidotyrosine residue far from IBB. Thereby, the recombinant bound to the CNT tip can interact specifically with importin β, as depicted in Fig. 6.6(a). In contrast, F56Amb has azidotyrosine near IBB. It is caught by the CNT tip at IBB. Consequently, F56Amb bound to the CNT tip is expected to interact with importin β, but not specifically, as depicted in Fig. 6.6(c). Importin α containing an azidotyrosine residue was attached site-specifically to the CNT probe tip using the Staudinger reaction [108,109]. Therefore, the unbinding force *i.e.*, rupture force was measured from the force curve in both cases.

Figure 6.6(b) portrays a histogram of the rupture force using a combination of importin α F124Amb and importin β molecules. Results show a single peak at 43.0 pN. The rupture force depends on the loading rate $r_f = dF/dt$, where F is the rupture force and where t denotes time [110]. The force was measured at a loading rate of 2000 pN/s. The force value obtained here is well fitted to the loading rate – rupture force curve reported in our previous result [111]. Therefore, the measured force is expected to be a specific force between importin α and importin β.

Figure 6.6(d) portrays a histogram of the rupture force using a combination of importin α F56Amb and importin β molecules. Different from F124Amb, F56Amb has an azidotyrosine residue near its IBB. Therefore, the IBB is blocked when it is attached to the CNT tip. The measured force is 10.9 pN, which is much lower than the case of F124Amb. This result confirms that the force obtained for F124Amb is the specific force between IBB and importin β, and that the force for F56Amb is the non-specific force between importin α and importin β.

Although it has been impossible to observe directly whether a single importin α molecule attaches to the CNT tip, we measured the force resulting from single binding events using a CNT arm fabricated in TEM. Using the CNT sheet also brings important

benefits for the measurement of specific force. In fact, even in a previous work using commercially available CNT probes, a multimolecular force would be detected because the CNT probe tip is insufficiently small and causes binding of several proteins to its tip [112]. In this sense, this work has important value not only as a step for single-molecule measurement in biology but also as a basis for functional nanodevices using CNTs.

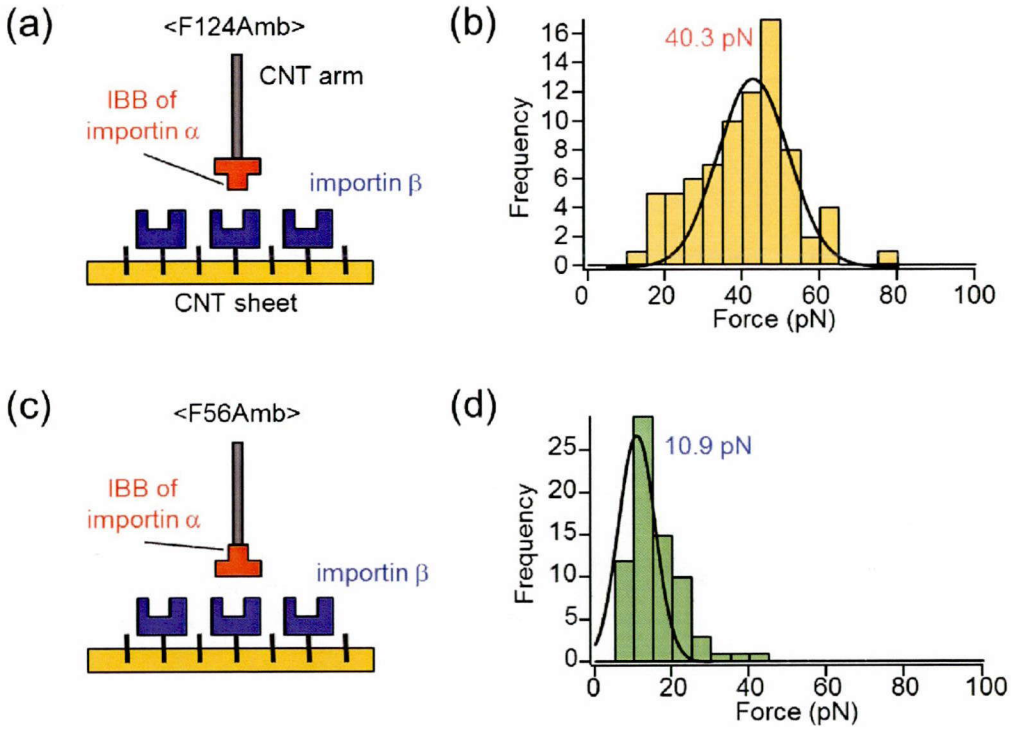

Fig. 6.6 Models of results of force measurements of two types. (a) Schematic images of protein trapping using a CNT arm with importin α F124Amb which has azidotyrosine residue far from IBB and a CNT sheet with importin β. (b) Histogram of rupture force between two proteins in the case of (a). (c) Schematic images of protein trapping using F56Amb which has the azidotyrosine near IBB. (d) Histogram of rupture force between two proteins in the case of (c).

6.6 Mass measurements

The mass measurement system is based on the CNT-FET device. One of our proposed devices is depicted in Fig. 6.7(a). The system consists of an AFM tip equipped a CNT arm and a CNT transistor. The CNT arm is putted on the AFM tip along the normal direction of the AFM tip as depicted in Fig. 6.7(b). For this, the measurements can be repeated merely by changing the AFM tip equipped with a CNT arm. In the

measurement, a function generator gives alternate voltage to the top gate for vibrating the CNT arm. When the CNT vibrates with amplitude f, the source-drain current also alternates corresponding to the alternately changed electrical field between upper CNT arm and bottom CNT in the transistor. Moreover, when a protein is trapped at the tip of the CNT, the resonance frequency of the CNT can be changed by Δf and shifts to the $f' = f + \Delta f$. Using f and f', the mass of protein m is calculated as shown below.

$$m = \frac{m_0}{4}\left\{\left(\frac{f}{f'}\right)^2 - 1\right\} \tag{6.1}$$

In that equation, m_0 denotes the mass of the CNT arm (protruding from the AFM tip).

Our group has detected the resonance frequency of CNT arms in vacuum condition by this system. One result obtained using a CNT of which the mass m_0 is ca. 2.95×10^{-19} g shows that the resonance frequency f is 2083 kHz. Based on this result, we have a forecast that the system can measure the mass $m = 3.54 \times 10^{-23}$ g $= 0.0354$ zg (zepto: 10^{-21}) in a liquid environment by assuming that the shift of resonance frequency Δf is at least 100 Hz. The mass of the importin β used in section 6.5 is ca. 150 zg. Therefore, the system can be a strong tool for measuring the mass of single protein molecules in a liquid environment. However, the measurement in a liquid in a nanoworld has many difficulties. It remains as a great challenge for the development of nanodevices.

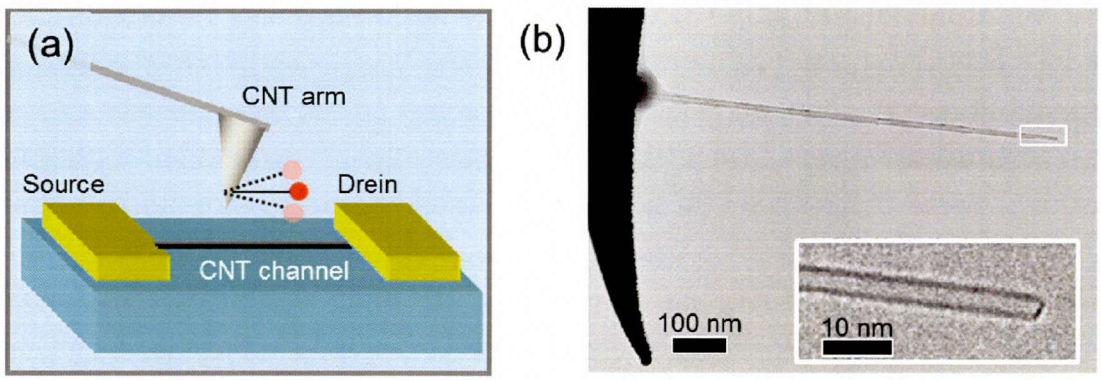

Fig. 6.7 Schematics and TEM images for mass measurement system. (a) Schematics of the mass measurement system consisting of a CNT transistor and a CNT arm. (b) TEM image of the CNT arm used for that system.

6.7 Summary

For the measurements of a single biomolecule, the author has developed CNT arms of two types. As a fundamental technique for CNT arm creation, the attachment process of a CNT to the substrate using C_{60} molecules has been demonstrated. The structural change of C_{60} molecular layer induced by an electron beam at the contact region between the CNT and the substrate functioned effectively to attach the CNT to the substrate.

Sharpened tips for force measurements are produced by Joule heating. The tip protruding length and diameter are well controlled in the process. For mass measurements, the fabrication process to join a thin and short CNT, which becomes a trapping portion for a single molecule on a tip of a multiwall CNT has been demonstrated. In that process, a hollow CNT facing the tip of a dense multiwall CNT is heated by Joule heating and works with a function to provide carbon source for fabricating a thin CNT through its breakdown and reconstruction. The tips of those CNT arms are opened by field emissions.

Force measurements using the CNT arm were conducted using a pair of proteins of importin α and importin β. When importin α was bound to the nanotube tip far from its importin β binding domain, the measured force against importin β was 43 pN. The value was much larger than that obtained when importin α was caught at the binding domain to the nanotube tip. This result underscores the fact that only the specific force can be measured by attaching a protein at an arbitrary site using CNTs. It proves the advance of CNT arms for single-molecule measurements.

The proposed mass measurement system is confirmed to work in a vacuum condition. The result provides a forecast that the system can measure a mass as small as $m=3.54\times10^{-23}$ g =0.0354 zg in a liquid environment, which is much smaller than the mass of proteins, for example the mass of importin β: 150 zg. For realizing this measurement, measurement in a liquid condition remains as a subject for additional study.

Chapter 7 Conclusion

Carbon nanotubes have been anticipated for use as components in newly developed nanodevices because of their unique properties. The objective of this thesis was to describe the design, fabrication, and assessment of nanodevices consisting of CNTs experimentally and to establish a basis for nanocarbon devices. This thesis has been devoted to the study of nanodevices of three types. The first is a high-frequency oscillator using low friction between layers in a CNT (chapter 4). The second is a torsional actuator based on the unique state transition property (chapter 5). The third is a nanosensor for measuring single biomolecules (chapter 6). The main results obtained in this study are presented below.

Chapter 4: Nano-oscillator

1 TEM observations with a heating holder revealed that, at the high temperature of 673 K, the linear motion of the CNT capsules in the hollow space in the outer CNT is more active than at room temperature. Results confirmed that the back-and-forth motion of the CNT capsule is thermally activated. According to the Arrhenius equation, the frequency of back-and-forth movement for the CNT capsules can be 10^4 Hz at room temperature.

2 However, a temperature as high as 1073 K obstructs the movement of the CNT capsules and the activation of the linear motion. The most probable origin of the obstruction is the thermal fluctuation of the sidewall of the outer CNT.

3 Dumbbell-shaped CNTs formed for use in nano-oscillators were fabricated using Joule heating and applying tensile stress in TEM. In the process, the sublimation of atoms from 5–7 defects starts from the center of the bridged CNT with tensile stress as well as migration of 5–7 defects at 1.6 μA/nm of circumferential current density. The sublimation rate is ca. 300 atoms/s, which is a value between those reported previously, providing large diameter changes in a short distance at both sides and a suitable dumbbell shape for the nano-oscillator.

Chapter 5: Nanotorsional actuator

4 TEM manipulation and MD simulations have demonstrated the transition between the flattened and the tubular states in a CNT that can serve as a nanotorsional actuator. The MD simulations clarified that the twist of the flattened CNT results from taking specific graphitic stacking orders for the CNT interior. Results also clarified that the driving force for the transition is the thermal energy. The boundary between the tubular state region and the flattened state region changes its position depending on the temperature.

5 TEM observations of repeated transition behaviors have also revealed the existence of hysteresis in the transition. The hysteresis is explained by the asymmetric potential energy in the state transition: Sufficient energy for the transition from the flattened to the tubular state *i.e.* the circumferential current density takes a higher value than that for the transition from a tubular to flattened state.

6 These results present the possibility of design and control of the output torsional angle and torque of the nanotorsional actuator by selecting the chiralities and lengths of CNTs and controlling the current. The transition speed estimated from MD simulations provides gigahertz-order repeatable clockwise and counterclockwise rotations in the device. The torque is estimated as several nanoNewton nanometers, which is much stronger than that of rotational biomolecular motors. The actuator that we have proposed has broad potential for application to driving of miniaturized devices such as a switch, an oscillator, and a nanosized screwdriver or gear.

Chapter 6: Nanobiosensors

7 As a fundamental technique for the creation of the CNT arms for single protein molecular measurement, the attachment process of a CNT to the substrate using C_{60} molecules was demonstrated. The structural change of C_{60} molecular layer induced by electron beam at the contact region between the CNT and the substrate functioned effectively to attach the CNT to the substrate.

8 Sharpened tips for the force measurement of single-protein molecules are made by Joule heating in TEM. The tip protruding length and diameter are well controlled in the process. For mass measurements, I have demonstrated the fabrication process to join a thin and short CNT, which becomes a trapping portion for a single molecule on a tip of a multiwall CNT. In the process, a hollow CNT facing the tip of a dense multiwall CNT is heated by Joule heating and works with a function to provide a carbon source for fabricating a thin CNT through its breakdown and reconstruction. The tips of those CNT arms are opened by field emissions.

9 Force measurements using the CNT arm were conducted using a pair of proteins of importin α and importin β. When importin α was bound to the nanotube tip far from its importin β binding domain, the measured force against importin β was 43 pN. The value was much larger than that obtained when importin α was caught at the binding domain to the nanotube tip. This result illustrates that only the specific force can be measured by attaching a protein at an arbitrary site using CNTs. It proves the advance of CNT arms for single molecule measurements. Regarding mass measurements, the system consisting of a CNT arm and a CNT transistor is confirmed to work in a vacuum condition. The result provides a forecast that the system can measure a mass as small as m=3.54×10^{-23} g =0.0354 zg in a liquid environment, which is much smaller than the mass of proteins.

Acknowledgements

All work described in this thesis was conducted at Osaka University. I first extend my sincere appreciation to Prof. Yoshikazu Nakayama of Osaka University for his kind and continued guidance and suggestions during the course of work in preparation of this thesis. I am especially grateful also to Prof. Yoji Shibutani and Prof. Yasuhiro Takaya of Osaka University for their review of this thesis work.

Furthermore, I would like to acknowledge Prof. Kaori Hirahara of Osaka University for helpful advice, discussion and suggestions, especially related to work related to electron microscopy, without which I would not have attained my present level of skill in operating transmission electron microscopes.

For his strong support and excellent discussion of molecular dynamics simulations described in chapter 5, I also acknowledge Prof. Yasutaka Yamaguchi of Osaka University. In addition, I wish to thank all members of the "Bunshiken" meeting for their kind invitation and useful advice and suggestions. Especially, I deeply appreciate helpful suggestions and discussions related to computational studies from Prof. Masahiko Shibahara.

My sincere thanks are similarly extended to all past and present colleagues at our laboratory, especially Dr. Eiji Kawabe, Dr. Masahiro Nakano, Dr. Yohei Maeno, Dr. Takeshi Nagasaka, Dr. Ahmadreza Fallahgilvaei, Dr. Hiroyuki Maruyama, Ms. Masami Toyoda, M.Eng. Hiroshi Somada, M.Eng. Satoshi Nunotani, M.Eng. Daisuke Kamesaki, M.Eng. Atsunori Ishikawa, M.Eng. Takanari Matsuda, M.Eng. Kento Nakata, M.Eng. Toshihiro Tsutsui, M.Eng. Keita Inose, M.Eng. Satoshi Tabuchi, M.Eng. Madoka Yamaguchi, M.Eng. Shotaro Itaya, Mr. Takehiko Emi, Mr. Motochika Juso and Mr. Yuki Yonetani for their useful discussions related to this research. I am also grateful to Ms. Kaeko Momose and Ms. Sahoko Kawasaki for their help and patience in carrying out administrative affairs on my behalf.

I am also thankful to Asahi Glass Co. Ltd. (AGC) and Japan Science and Technology Agency (JST) for financial support during the course of my work.

Above all, I am forever and deeply indebted to my family for their earnest and sincere support, without which I would have been unable to complete this thesis.

For all those named above, and for others not named but not forgotten, my gratitude is boundless.

References

[1] A. Cho, D. Normile, Higgs Boson Makes Its Debut After Decades-Long Search, Science. **337** (2012) 142.

[2] R. P. Feynman, There's Plenty of Room at the Bottom: An Invitation to Enter a New World of Physics, Engineering and Science. **23** (1960) 22.

[3] G.A. Ozin, I. Manners, S. Fournier-Bidoz, A. Arsenault, Dream Nanomachines, Advanced Materials. **17** (2005) 3011–3018.

[4] E.L. Wolf, Nanophysics and Nanotechnology –An Introduction to Modern Concepts in Nanoscience, Second, WILEY-VCH, 2011.

[5] J. Cumings, A. Zettl, Low-Friction Nanoscale Linear Bearing Realized from Multiwall Carbon Nanotubes, Science. **289** (2000) 602–604.

[6] S. Akita, Y. Nakayama, Interlayer Sliding Force of Individual Multiwall Carbon Nanotubes, Japanese Journal of Applied Physics. **42** (2003) 4830–4833.

[7] R.C. Merkle, Computational nanotechnology, Nanotechnology. **2** (1991) 134.

[8] H.W. Kroto, J.R. Heath, S.C. O'Brien, R.F. Curl, R.E. Smalley, C60: Buckminsterfullerene, Nature. **318** (1985) 162.

[9] M. S. Dresselhaus, G. Dresselhaus, P.C. Eklund, Science of Fullerenes and Carbon Nanotubes, Academic Press, 1996.

[10] G.A. Hughes, Nanostructure-mediated drug delivery., Nanomedicine : Nanotechnology, Biology, and Medicine. **1** (2005) 22–30.

[11] Frontier nanocarbon HP (http://www.f-carbon.com/special_applist.html), (n.d.).

[12] S. Iijima, Helical microtubules of graphitic carbon, Nature. **354** (1991) 56.

[13] R. Saito, M. Fujita, G. Dresselhaus, M. Dresselhaus, Electronic structure of graphene tubules based on C60., Physical Review. B. **46** (1992) 1804–1811.

[14] R.H. Baughman, A.A. Zakhidov, W.A. de Heer, Carbon nanotubes--the route toward applications., Science. **297** (2002) 787.

[15] S. Berber, Y. Kwon, D. Tomanek, Unusually high thermal conductivity of carbon nanotubes, Physical Review Letters. **84** (2000) 4613.

[16] G. Begtrup, K. Ray, B. Kessler, T. Yuzvinsky, H. Garcia, A. Zettl, Probing Nanoscale Solids at Thermal Extremes, Physical Review Letters. **99** (2007) 155901.

[17] H. Nishijima, S. Kamo, S. Akita, Y. Nakayama, K.I. Hohmura, S.H. Yoshimura, et al., Carbon-nanotube tips for scanning probe microscopy: Preparation by a controlled process and observation of deoxyribonucleic acid, Applied Physics Letters. **74** (1999) 4061.

[18] TORAY HP (http://www.toray.co.jp/news/rd/nr120209.html) in Japanese, (2012) 1–2.

[19] R.E. Haufler, J. Conceicao, L.P.F. Chibante, Y. Chai, N.E. Byrne, S. Flanagan, et al., Efficient Produetion of C60 (Buckminsterfullerene), C60H36, and the Solvated Buckide Ion, The Journal of Physical Chemistry. **94** (1990) 8634–8636.

[20] T.W. Ebbesen, P.M. Ajayan, Large-scale synthesis of carbon nanotubes, Nature. **358** (1992) 220.

[21] D.S. Bethune, C.H. Kiang, M.S. de Vries, G. Gorman, R. Savoy, J. Vazquez, et al., Cobalt-catalysed growth of carbon nanotubes with single-atomic-layer walls, Nature. **363** (1993) 605.

[22] Y. Nakayama, Synthesis, Nanoprocessing, and Yarn Application of Carbon Nanotubes, Japanese Journal of Applied Physics. **47** (2008) 8149–8156.

[23] T. Yamada, T. Namai, K. Hata, D.N. Futaba, K. Mizuno, J. Fan, et al., Size-selective growth of double-walled carbon nanotube forests from engineered iron catalysts., Nature Nanotechnology. **1** (2006) 131–6.

[24] A.M. Thayer, Carbon Nanotubes By The Metric Ton, Chemical and Engineering News. **85** (2007) 29.

[25] R.F. Service, Nanotubes Show Image-Display Talent, Science. **270** (1991) 1119.

[26] N.R. Franklin, H. Dai, An Enhanced CVD Approach to Extensive Nanotube Networks with Directionality, Advanced Materials. **12** (2000) 890–894.

[27] M.S. Dresselhaus, G. Dresselhaus, R. Saito, Physics of carbon nanotubes, Carbon. **33** (1995) 883–891.

[28] J.W.G. Wildoer, L.C. Venema, A.G. Rinzler, R.E. Smalley, C. Dekker, Electronic structure of atomically resolved carbon nanotubes ¨, Nature. **391** (1998) 59.

[29] S.J. Tans, M.H. Devoret, H. Dai, T. Andreas, R.E. Smalley, L.J. Geerligs, et al., Individual single-wall carbon nanotubes as quantum wires, Nature. **286** (1997) 474.

[30] H.W. Postma, T. Teepen, Z. Yao, M. Grifoni, C. Dekker, Carbon nanotube single-electron transistors at room temperature., Science (New York). **293** (2001) 76.

[31] D. Mann, A. Javey, J. Kong, Q. Wang, H. Dai, Ballistic Transport in Metallic Nanotubes with Reliable Pd Ohmic Contacts, Nano Letters. **3** (2003) 1541–1544.

[32] T. Dürkop, S.A. Getty, E. Cobas, M.S. Fuhrer, Extraordinary Mobility in Semiconducting Carbon Nanotubes, Nano Letters. **4** (2004) 35–39.

[33] A. Sears, R.C. Batra, Macroscopic properties of carbon nanotubes from molecular-mechanics simulations, Physical Review B. **69** (2004) 235406.

[34] M.M.J. Treacy, T.W. Ebbesen, J.M. Gibson, Exceptionally high Young's modulus observed for individual carbon nanotubes, Nature. **381** (1996) 678.

[35] P. Poncharal, Z.L. Wang, D. Ugarte, W.A. de Heer, Electrostatic Deflections and Electromechanical Resonances of Carbon Nanotubes, Science. **283** (1999) 1513–1516.

[36] A. Krishnan, E. Dujardin, T. Ebbesen, P. Yianilos, M. Treacy, Young's modulus of single-walled nanotubes, Physical Review B. **58** (1998) 14013–14019.

[37] E.W. Wong, P.E. Sheehan, C.M. Lieber, Nanobeam Mechanics: Elasticity, Strength, and Toughness of Nanorods and Nanotubes, Science. **277** (1997) 1971–1975.

[38] S. Akita, H. Nishijima, Y. Nakayama, F. Tokumasu, K. Takeyasu, Carbon nanotube tips for a scanning probe microscope: their fabrication and properties, Journal of Physics D: Applied Physics. **32** (1999) 1044–1048.

[39] M.-F. Yu, O. Lourie, M.J. Dyer, K. Moloni, T.F. Kelly, R.S. Ruoff, Strength and Breaking Mechanism of Multiwalled Carbon Nanotubes Under Tensile Load, Science. **287** (2000) 637–640.

[40] B.G. Demczyk, Y.M. Wang, J. Cumings, M. Hetman, W. Han, A. Zettl, et al., Direct mechanical measurement of the tensile strength and elastic modulus of multiwalled carbon nanotubes, Materials Science and Engineering: A. **334** (2002) 173–178.

[41] B. Yakobson, C. Brabec, J. Berhnolc, Nanomechanics of carbon tubes: Instabilities beyond linear response., Physical Review Letters. **76** (1996) 2511–2514.

[42] B.I. Yakobson, M.P. Campbell, C.J. Brabec, J. Bernholc, High strain rate fracture and C-chain unraveling in carbon nanotubes, Computational Materials Science. **8** (1997) 341–348.

[43] O. Suekane, A. Nagataki, H. Mori, Y. Nakayama, Static Friction Force of Carbon Nanotube Surfaces, Applied Physics Express. **1** (2008) 064001.

[44] L.X. Benedict, S.G. Louie, M.L. Cohen, Heat Capacity of Carbon Nanotubes, Solid State Communications. **100** (1996) 177–180.

[45] J. Lasjaunias, K. Biljaković, Z. Benes, J. Fischer, P. Monceau, Low-temperature specific heat of single-wall carbon nanotubes, Physical Review B. **65** (2002) 113409.

[46] P. Kim, L. Shi, A. Majumdar, P. McEuen, Thermal Transport Measurements of Individual Multiwalled Nanotubes, Physical Review Letters. **87** (2001) 215502.

[47] D. Yang, Q. Zhang, G. Chen, S. Yoon, J. Ahn, S. Wang, et al., Thermal conductivity of multiwalled carbon nanotubes, Physical Review B. **66** (2002) 165440.

[48] J. Hone, M.C. Llaguno, M.J. Biercuk, A.T. Johnson, B. Batlogg, Z. Benes, et al., Thermal properties of carbon nanotubes and nanotube-based materials, Applied Physics A: Materials Science & Processing. **74** (2002) 339–343.

[49] T. Yamamoto, S. Watanabe, K. Watanabe, Universal Features of Quantized Thermal Conductance of Carbon Nanotubes, Physical Review Letters. **92** (2004) 075502.

[50] K. Hirahara, S. Bandow, H. Kataura, M. Kociak, S. Iijima, Stretching of carbon-carbon bonds in a 0.7nm diameter carbon nanotube studied by electron diffraction, Physical Review B. **70** (2004) 205422.

[51] Y. Nakayama, Plasticity of Carbon Nanotubes: Aiming at Their Use in Nanosized Devices, Japanese Journal of Applied Physics. **46** (2007) 5005–5014.

[52] Y. Nakayama, A. Nagataki, O. Suekane, X. Cai, S. Akita, Current-Induced Plastic Deformation of Double-Walled Carbon Nanotubes, Japanese Journal of Applied Physics. **44** (2005) L720–L722.

[53] K. Hirahara, K. Inose, Y. Nakayama, Determination of the chiralities of isolated carbon nanotubes during superplastic elongation process, Applied Physics Letters. **97** (2010) 051905.

[54] R.D. Vale, R.A. Milligan, The way things move: looking under the hood of molecular motor proteins, Science. **288** (2000) 88.

[55] N. Kodera, D. Yamamoto, R. Ishikawa, T. Ando, Video imaging of walking myosin V by high-speed atomic force microscopy., Nature. **468** (2010) 72–6.

[56] Y. Sambongi, Y. Iko, M. Tanabe, H. Omote, A. Iwamoto-Kihara, I. Ueda, et al., Mechanical Rotation of the c Subunit Oligomer in ATP Synthase (F0F1): Direct Observation, Science. **286** (1999) 1722–1724.

[57] R.K. Soong, G.D. Bachand, H.P. Neves, A.G. Olkhovets, H.G. Craighead, C.D. Montemagno, Powering an inorganic nanodevice with a biomolecular motor, Science. **290** (2000) 1555.

[58] R. Baughman, Conducting polymer artificial muscles, Synthetic Metals. **78** (1996) 339–353.

[59] Y. Osada, H. Okuzaki, H. Hori, A polymer gel with electrically driven motility, Nature. **355** (1992) 242.

[60] R. Pelrine, R. Kornbluh, Q. Pei, J. Joseph, High-speed electrically actuated elastomers with strain greater than 100%, Science. **287** (2000) 836.

[61] A.M. Fennimore, T.D. Yuzvinsky, W.-Q. Han, M.S. Fuhrer, J. Cumings, A. Zettl, Rotational actuators based on carbon nanotubes, Nature. **424** (2003) 408–410.

[62] A. Barreiro, R. Rurali, E.R. Hernández, J. Moser, T. Pichler, L. Forró, et al., Subnanometer motion of cargoes driven by thermal gradients along carbon nanotubes., Science. **320** (2008) 775–778.

[63] K. Jensen, K. Kim, A. Zettl, An atomic-resolution nanomechanical mass sensor., Nature Nanotechnology. **3** (2008) 533–537.

[64] K. Jensen, J. Weldon, H. Garcia, A. Zettl, Nanotube Radio, Nano Letters. **7** (2007) 3508–3511.

[65] R.J. Chen, S. Bangsaruntip, K.A. Drouvalakis, N.W.S. Kam, M. Shim, Y. Li, et al., Noncovalent functionalization of carbon nanotubes for highly specific electronic biosensors., Proceedings of the National Academy of Sciences of the United States of America. **100** (2003) 4984–4989.

[66] K. Besteman, J.-O. Lee, F.G.M. Wiertz, H.A. Heering, C. Dekker, Enzyme-Coated Carbon Nanotubes as Single-Molecule Biosensors, Nano Letters. **3** (2003) 727–730.

[67] H. Somada, K. Hirahara, S. Akita, Y. Nakayama, A molecular linear motor consisting of carbon nanotubes, Nano Letters. **9** (2008) 62–65.

[68] S.B. Legoas, V.R. Coluci, S.F. Braga, P.Z. Coura, S.O. Dantas, D.S. Galvão, Molecular-Dynamics Simulations of Carbon Nanotubes as Gigahertz Oscillators, Physical Review Letters. **90** (2003) 055504.

[69] R. Senga, K. Hirahara, Y. Nakayama, Nanotorsional actuator using transition between flattened and tubular states in carbon nanotubes, Applied Physics Letters. **100** (2012) 083110.

[70] R. Senga, K. Hirahara, Y. Nakayama, Attachment of Carbon Nanotubes to a Substrate by Electron-Beam-Induced Structural Change of Fullerene Molecules, Applied Physics Express. **3** (2010) 025001.

[71] H. Maruyama, S.H. Yoshimura, S. Akita, A. Nagataki, Y. Nakayama, Covalent attachment of protein to the tip of a multiwalled carbon nanotube without sidewall decoration, Journal of Applied Physics. **102** (2007) 094701.

[72] S. Ohno, M. Matsui, T. Yokogawa, M. Nakamura, T. Hosoya, T. Hiramatsu, et al., Site-selective post-translational modification of proteins using an unnatural amino acid, 3-azidotyrosine., Journal of Biochemistry. **141** (2007) 335–343.

[73] Y.-K. Kwon, D. Tománek, S. Iijima, "Bucky Shuttle" Memory Device: Synthetic Approach and Molecular Dynamics Simulations, Physical Review Letters. **82** (1999) 1470–1473.

[74] Y. Ueno, H. Somada, K. Hirahara, Y. Nakayama, S. Akita, Molecular Dynamics Simulations for Molecular Linear Motor Inside Nanotube, Japanese Journal of Applied Physics. **48** (2009) 06FG03.

[75] Y. Maeno, A. Ishikawa, Y. Nakayama, Adhesive Behavior of Single Carbon Nanotubes, Applied Physics Express. **3** (2010) 065102.

[76] R.M. Servuss, W. Helfrich, Mutual adhesion of lecithin membranes at ultralow tensions, Journal De Physique France. **50** (1989) 809–827.

[77] N.G. Chopra, L.X. Benedict, V.H. Crespi, M.L. Cohen, S.G. Louie, A. Zettl, Fully collapsed carbon nanotubes, Nature. **377** (1995) 135–138.

[78] M. Huhtala, A. V. Krasheninnikov, J. Aittoniemi, S.J. Stuart, K. Nordlund, K. Kaski, Improved mechanical load transfer between shells of multiwalled carbon nanotubes, Physical Review B. **70** (2004) 045404.

[79] H.A. Zambrano, J.H. Walther, R.L. Jaffe, Thermally driven molecular linear motors: A molecular dynamics study., The Journal of Chemical Physics. **131** (2009) 241104.

[80] V.R. Coluci, V.S. Timóteo, D.S. Galvão, Thermophoretically driven carbon nanotube oscillators, Applied Physics Letters. **95** (2009) 253103.

[81] R. Rurali, E.R. Hernández, Thermally induced directed motion of fullerene clusters encapsulated in carbon nanotubes, Chemical Physics Letters. **497** (2010) 62–65.

[82] Z. Guo, T. Chang, X. Guo, H. Gao, Mechanics of thermophoretic and thermally induced edge forces in carbon nanotube nanodevices, Journal of the Mechanics and Physics of Solids. **60** (2012) 1676–1687.

[83] K. Ran, J.-M. Zuo, Q. Chen, Z. Shi, Electron beam stimulated molecular motions., ACS Nano. **5** (2011) 3367–3372.

[84] C. Jin, K. Suenaga, S. Iijima, Plumbing carbon nanotubes., Nature Nanotechnology. **3** (2008) 17–21.

[85] T.D. Yuzvinsky, W. Mickelson, S. Aloni, G.E. Begtrup, A. Kis, A. Zettl, Shrinking a carbon nanotube., Nano Letters. **6** (2006) 2718–2722.

[86] H. Maruyama, T. Ishibashi, K. Hirahara, Y. Nakayama, Carbon Nanotube Sharpening Using an Induced Electrical Current, Applied Physics Express. **3** (2010) 025101.

[87] J.Y. Huang, S. Chen, Z.Q. Wang, K. Kempa, Y.M. Wang, S.H. Jo, et al., Superplastic carbon nanotubes., Nature. **439** (2006) 281.

[88] X. Cai, S. Akita, Y. Nakayama, Current induced light emission from a multiwall carbon nanotube, Thin Solid Films. **464-465** (2004) 364–367.

[89] Z. Liu, M. Koshino, K. Suenaga, A. Mrzel, H. Kataura, S. Iijima, Transmission Electron Microscopy Imaging of Individual Functional Groups of Fullerene Derivatives, Physical Review Letters. **96** (2006) 088304.

[90] D.W. Brenner, Emprical potential for hydrocarbons for use in simulating the chemical vapor deposition of diamond films, Physical Review B. **42** (1990) 9458.

[91] J. Tersoff, New Empirical Model for the Structural Properties of Silicon, Physical Review Letters. **56** (1986) 632–635.

[92] Y. Yamaguchi, S. Maruyama, A molecular dynamics simulation of the fullerene formation process, Chemical Physics Letters. **286** (1998) 336–342.

[93] S. Maruyama, Y. Yamaguchi, A molecular dynamics demonstration of annealing to a perfect C 60 structure, Chemical Physics Letters. **286** (1998) 343–349.

[94] Y. Shibuta, S. Maruyama, Molecular dynamics of the generation process of double-walled carbon nanotubes from peapods, Heat Transfer—Asian Research. **35** (2006) 254–264.

[95] H.J.C. Berendsen, J.P.M. Postma, W.F. van Gunsteren, A. DiNola, J.R. Haak, Molecular dynamics with coupling to an external bath, The Journal of Chemical Physics. **81** (1984) 3684.

[96] Y. Miyata, M. Suzuki, M. Fujihara, Y. Asada, R. Kitaura, H. Shinohara, Solution-phase extraction of ultrathin inner shells from double-wall carbon nanotubes., ACS Nano. **4** (2010) 5807–5812.

[97] S. Akita, H. Nishijima, Y. Nakayama, Influence of stiffness of carbon-nanotube probes in atomic force microscopy, Journal of Physics D: Applied Physics. **33** (2000) 2673–2677.

[98] A. Nagataki, T. Kawai, Y. Miyamoto, O. Suekane, Y. Nakayama, Controlling Atomic Joints between Carbon Nanotubes by Electric Current, Physical Review Letters. **102** (2009) 176808.

[99] Y.-M. Lin, P. Avouris, Strong suppression of electrical noise in bilayer graphene nanodevices., Nano Letters. **8** (2008) 2119–2125.

[100] J.-P. Salvetat, J.-M. Bonard, N.H. Thomson, A.J. Kulik, L. Forró, W. Benoit, et al., Mechanical properties of carbon nanotubes, Applied Physics A: Materials Science & Processing. **69** (1999) 255–260.

[101] J. Shiomi, S. Maruyama, Non-Fourier heat conduction in a single-walled carbon nanotube: Classical molecular dynamics simulations, Physical Review B. **73** (2006) 205420.

[102] Z. Xu, M.J. Buehler, Nanoengineering heat transfer performance at carbon nanotube interfaces., ACS Nano. **3** (2009) 2767–2775.

[103] G. Cingolani, C. Petosa, K. Weis, C.W. Müller, Structure of importin-beta bound to the IBB domain of importin-alpha., Nature. **399** (1999) 221–229.

[104] S. Akita, Y. Nakayama, S. Mizooka, Y. Takano, T. Okawa, Y. Miyatake, et al., Nanotweezers consisting of carbon nanotubes operating in an atomic force microscope, Applied Physics Letters. **79** (2001) 1691.

[105] S. Sawaya, S. Akita, Y. Nakayama, In situ mass measurement of electron-beam-induced nanometer-sized W-related deposits using a carbon nanotube cantilever, Applied Physics Letters. **89** (2006) 193115.

[106] Z. Liu, K. Suenaga, P. Harris, S. Iijima, Open and Closed Edges of Graphene Layers, Physical Review Letters. **102** (2009) 015501.

[107] A. Kuznetsova, D.B. Mawhinney, V. Naumenko, J.T. Yates, J. Liu, R.E. Smalley, Enhancement of adsorption inside of single-walled nanotubes : opening the entry ports, Chemical Physics Letters. **321** (2000) 292–296.

[108] E. Saxon, C.R. Bertozzi, Cell Surface Engineering by a Modified Staudinger Reaction, Science. **287** (2000) 2007–2010.

[109] K.L. Kiick, E. Saxon, D.A. Tirrell, C.R. Bertozzi, Incorporation of azides into recombinant proteins for chemoselective modification by the Staudinger ligation., Proceedings of the National Academy of Sciences of the United States of America. **99** (2002) 19–24.

[110] E. Evans, K. Ritchie, Dynamic strength of molecular adhesion bonds., Biophysical Journal. **72** (1997) 1541–55.

[111] M. Yamaguchi, M. Nakano, R. Senga, H. Maruyama, S.H. Yoshimura, Y. Nakayama, Specific interaction studied by single-molecule force measurement using a carbon nanotube probe, Proceedings of the IASTED International Conference on Biomechanics. (2011) 22.

[112] S. Stanislaus, E. Wong, T. Adam, others, Covalently functionalized nanotubes as nanometre-sized probes in chemistry and biology, Nature. **394** (1998) 52–55.

Publication list

1. "Attachment of carbon nanotubes to a substrate by electron-beam-induced structural change of fullerene molecules", Ryosuke Senga, Kaori Hirahara, Yoshikazu Nakayama, Applied Physics Express Vol.3 pp.025001-025003, 2010.1

2. "Nanotorsional actuator using transition between flattened and tubular states in carbon nanotubes", Ryosuke Senga, Kaori Hirahara, Yoshikazu Nakayama, Applied Physics Letters vol.100 pp.083110-083113, 2012.3

3. "Carbon nanotube torsional actuator based on transition between flattened and tubular states", Ryosuke Senga, Kaori Hirahara, Yasutaka Yamaguchi, Yoshikazu Nakayama, Journal of Non-Crystal Solids, vol. 358 pp2541-2544. 2012.9

International conference list

1. "Manipulation of C_{60} molecules by electron beam and its application to attach carbon nanotubes to a substrate", Ryosuke Senga, Kaori Hirahara, Yoshikazu Nakayama, 11th International Conference on the Science and Application of Nanotubes 2010 (Canada), (2010.6) Poster

2. "Transition between flattened states and tubular states in carbon nanotubes", Ryosuke Senga, Kaori Hirahara, Yoshikazu Nakayama, A3 Symposium on Emerging Materials : Nanocarbon and Nanowires for Energy (Korea), (2010.11) Poster

3. "Torsional actuator based on transition between flattened states and tubular states in carbon nanotubes", Ryosuke Senga, Kaori Hirahara, Yasutaka Yamaguchi, Yoshikazu Nakayama, 12th International Conference on the Science and Application of Nanotubes 2011 (NT11) (England), (2011.7) Poster

4. "Carbon nanotube torsional actuator based on transition between flattened and tubular states", Ryosuke Senga, Kaori Hirahara, Yasutaka Yamaguchi, Yoshikazu Nakayama, 24th Internationaol Conference on Amorphous and Nanocrystalline Semiconductors (Japan), (2011.8) Oral

5. "Response of thermally activated torsional motion of carbon nanotube", Ryosuke Senga, Kaori Hirahara, Yoshikazu Nakayama, A3 Symposium on Emerging Materials : Nanometals for energy & environments (China), (2011.10) Poster

6. "Feasibility of high frequency oscillator consisting of carbon nanotubes" Ryosuke Senga, Kaori Hirahara, Yoshikazu Nakayama, 13th International Conference on the Science and Application of Nanotubes 2012 (NT12) (Australia), (2012.6) Oral

Appendix

A1 Temporary subtraction for molecular dynamics simulations

The velocity Verlet method was adopted to integrate the equation of motion as described below.

$$r_i(t+\Delta t) = r_i(t) + \Delta t \cdot v_i(t) + (\Delta t)^2 \frac{F_i(t)}{2m}, \tag{A1.1}$$

$$v_i(t+\Delta t) = v_i(t) + \frac{\Delta t}{2m}\{F_i(t+\Delta t) + F_i(t)\}, \tag{A1.2}$$

In those equations, r, v and F respectively denote the position, velocity, and force for an atom as a function of time t; m denotes the atomic mass. The value of the time step for the calculation was decided based on the following assessment. In general, a one-dimensional equation of the motion is expressed as

$$-\varepsilon \frac{\partial \Phi(r/\sigma)}{\partial r} = m\frac{d^2 r}{d^2 t}, \tag{A1.3}$$

where Φ denotes the potential energy of the system as a function of the position r, and where ε and σ respectively stand for the minimum value of the potential energy and the distance between two atoms when the potential energy becomes the minimum value. This equation can be translated to the equation shown below by introducing non-dimensional parameters $r'=r/\sigma$ (distance) and $t'=t/\tau_I$ (time).

$$-\frac{\partial \Phi(r')}{\partial r'} = \frac{m\sigma^2}{\varepsilon \tau_I^2}\frac{d^2 r'}{d^2 t'} \tag{A1.4}$$

By assuming that the time-derivative terms of both members are 1, the time scale τ_I is given as the following.

$$\frac{m\sigma^2}{\varepsilon \tau_I^2} = 1, \quad \tau_I = \sqrt{m\sigma^2/\varepsilon} \tag{A1.5}$$

At this time, τ_I presents the time scale for $r'=1$. Therefore, τ_I means the order of the time scale for an atom moving by distance σ. Thus, Δt should be chosen not to generate differential errors considering the value of τ_I. Using parameters for this study as shown in section 5.2 ($\varepsilon=D_e$=6.325 eV, $\sigma=R_e$=1.315 Å), τ_I =60 fs is given from eq. (A1.5). From this result and the calculation time, Δt=0.5 fs is adopted for this study.

A2 Temperature control for molecular dynamics simulations

A pair of carbon atoms that are closer than cut-off distance R are considered to share a bond. A group of carbon atoms connected with bonds is defined as a cluster. The total kinetic energy is defined as a cluster. The total kinetic energy of the cluster C_n containing n carbon atoms is separated into translational, rotational, and vibrational energies, respectively denoted as K_T, K_R, and K_V.

$$K_T = \frac{1}{2} nm \left| \bar{v} \right|^2$$

$$K_R = \frac{\left| \sum_{i=1}^{n} m r_i' \times v_i' \right|}{2 \sum_{i=1}^{n} m \left| r_i' \right|^2} \tag{A2.1}$$

$$K_V = \frac{1}{2} \sum_{i=1}^{n} m \left| v_i' \right|^2 - K_R$$

Therein, m donates the mass of carbon atom, and

$$r_i' = r_i - \bar{r}, \quad v_i' = v_i - \bar{v} \tag{A2.2}$$

are positions and velocities relative to those of the center of mass of the cluster

$$\bar{r} = \frac{1}{n} \sum_{i=1}^{n} r_i, \quad \bar{v} = \frac{1}{n} \sum_{i=1}^{n} v_i . \tag{A2.3}$$

The temperatures of respective clusters, T_T, T_R, and T_V, and the total temperatures T^t_T, T^t_R, and T^t_V are expressed as shown below.

$$T_T = \frac{2K_T}{3k_B}, \quad T_T^t = \frac{\sum v_T T_T}{\sum v_T} = \frac{2 \sum K_T}{3NK_B} \tag{A2.4}$$

$$T_R = \frac{2K_R}{k_B v_R}, \quad T_R^t = \frac{\sum v_R T_R}{\sum v_R} = \frac{2 \sum K_R}{k_B \sum v_R} \tag{A2.5}$$

$$T_V = \frac{2K_V}{k_B v_V}, \quad T_V^t = \frac{\sum v_V T_V}{\sum v_V} = \frac{2 \sum K_V}{k_B \sum v_V} \tag{A2.6}$$

In those equations, v and k_B respectively represent the number of degrees of freedom of motion and Boltzmann's constant. To enforce the temperature equilibrium, each

temperature of the system was controlled independently to the control temperature T_c so that the difference between $T_{T,R,V}$ and T_c was reduced by 60% in 0.1 ps.

A3 Trapping a protein at a carbon nanotube tip

Open-ended CNT on the AFM tips as described in section 6.4.3 has carboxyl groups (-COOH) in an oxidizing environment at its tip, as shown in Fig. A3.1(a). These carboxyl groups were activated by 2.5 mg/ml ethylenediamine (EDA) in 50 mM borate buffer, pH 8.2 (Buffer 1) for 15 min at room temperature. Then the CNT tip was decorated with amino groups (-NH_2). These amino groups were subjected to reaction with 11 mg/ml N-hydroxysulfosuccinimide (sulfo-NHS) in Buffers 1 and 4 mg/ml 1-ethyl-3-(3-dimethylaminopropyl)carbodiimide hydrochloride (EDC) in Buffer 1 for 15 min. Subsequently, the CNT was decorated with triarylphosphine derivative by exposure to 0.625 mM N-hydroxysuccinimide- triarylphosphine (NHS-PPh3) in Buffer 1 for 15 min. The triarylphosphine derivative reacts specifically with the azido-group (Staudinger reaction). In this reaction, the decorated CNT tip reacted with 0.0375 μM azido-importin α in Buffer 1 for 1 h was washed with 50 mM phosphate buffer, pH 8.0 (Buffer 2) and was immediately used thereafter in experiments. Consequently, importin α was covalently bonded to the tip of the CNT via the azido group, as presented in Fig. A3.1(b).

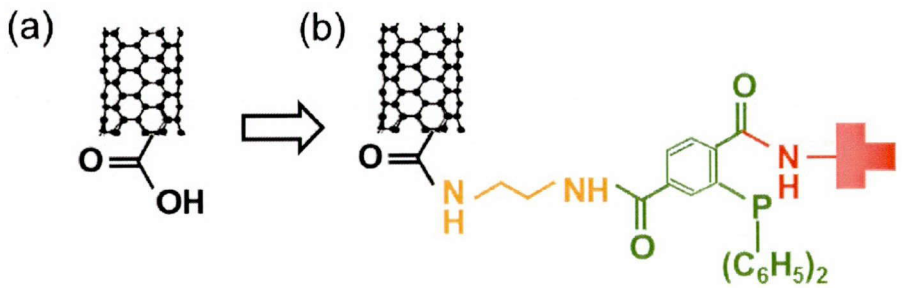

Fig. A3.1 Molecular model of (a) a single-walled CNT tip with one carboxyl group at its tip end and (b) the CNT model after final decoration by site-selective covalent binding with azido-importin α.